



DISSERTATION

3D Printed Polymer-Bonded NdFeB Magnets for a Tailored Magnetic Field

zur Erlangung des akademischen Grades

Doktor der technischen Wissenschaften

eingereicht von

Dipl.-Ing. Christian Huber

Matrikelnummer 0925229

an der

Fakultät für Festkörperphysik der Technischen Universität Wien

Betreuung: Ass.Prof. Dipl.-Ing. Dr.techn. Dieter Süss

Diese Dissertation haben begutachtet:

(Prof. Dr. Oliver Gutfleisch)

(Prof. Dipl.-Ing. Dr.mont.
Jürgen Stampfl)

Wien, 30.11.2017

(Dipl.-Ing. Christian Huber)



TECHNISCHE
UNIVERSITÄT
WIEN
Vienna University of Technology

DISSERTATION

3D Printed Polymer-Bonded NdFeB Magnets for a Tailored Magnetic Field

submitted in partial fulfillment of the requirements for the degree of

Doktor der technischen Wissenschaften

by

Dipl.-Ing. Christian Huber

Registration Number 0925229

to the

Faculty of Solid State Physics at the Vienna University of Technology

Advisor: Ass.Prof. Dipl.-Ing. Dr.techn. Dieter Süss

The dissertation has been reviewed by:

(Prof. Dr. Oliver Gutfleisch)

(Prof. Dipl.-Ing. Dr.mont.
Jürgen Stampfl)

Wien, 30.11.2017

(Dipl.-Ing. Christian Huber)

Erklärung zur Verfassung der Arbeit

Dipl.-Ing. Christian Huber
Maria-Trapp-Platz 2/2/216, 1220 Wien

Hiermit erkläre ich, dass ich diese Arbeit selbständig verfasst habe, dass ich die verwendeten Quellen und Hilfsmittel vollständig angegeben habe und dass ich die Stellen der Arbeit – einschließlich Tabellen, Karten und Abbildungen –, die anderen Werken oder dem Internet im Wortlaut oder dem Sinn nach entnommen sind, auf jeden Fall unter Angabe der Quelle als Entlehnung kenntlich gemacht habe.

(Ort, Datum)

(Dipl.-Ing. Christian Huber)

Danksagung

An dieser Stelle möchte ich vor allem Dieter Suess danken, der es mir ermöglichte diese Dissertation durchzuführen. Seine motivierende, optimistische Art Probleme zu lösen, hatte einen entscheidenden Einfluss auf diese Arbeit. Er hatte jederzeit ein offenes Ohr für Diskussionen und Hilfestellungen.

Abgesehen davon, wäre ein Zustandekommen dieser Dissertation ohne der Hilfestellung der gesamten Arbeitsgruppe kaum möglich gewesen. Spezieller Dank geht an Claas, Florian, Christoph und Roman, die immer eine große Hilfe waren bzw. auch mal für ein Feierabendbier zu haben waren.

Mein Dank gilt auch Oliver Gutfleisch und Jürgen Stampfl für die Begutachtung dieser Arbeit.

An dieser Stelle möchte ich auch Iulian Teliban und Martin Groenefeld und der gesamten Magnetfabrik Bonn GmbH danken. Ohne deren Engagement wäre diese Arbeit nicht möglich gewesen.

Ein großes Dankeschön geht natürlich auch an meine Familie und Freunde, die mich immer unterstützen und an mich glaubten.

Zu guter Letzt möchte ich noch meiner lieben Freundin Heike für die tolle Unterstützung danken.

Kurzfassung

Additive Fertigung ist heute der de-facto Standard in der Industrieproduktion. Der „industriellen Revolution aus dem Drucker“ wird enormes Potenzial bescheinigt. Dabei können Werkstücke ohne der Hilfe von Werkzeugen direkt aus Halbzeugen wie in Pulver oder Stangenform hergestellt werden. Eine große Zahl an unterschiedlichen additive Fertigungsmethoden ist zur Zeit am Markt verfügbar.

Doch bis dato ist keine additive Fertigung von magnetischen Materialien möglich. Obwohl ein großes Marktpotential darin besteht, Permanentmagnete so zu designen, damit sie ein spezielles magnetisches Feld erzeugen.

Ziel dieser Dissertation ist es, polymer gebundene Selten Erden (NdFeB) Materialien mittels eines handelsüblichen 3D-Drucker zu verarbeiten. Ein entschiedener Vorteil unseres Druckers ist die Möglichkeit zwei unterschiedliche Materialien zu mischen. Die Druckereinstellung und das verwendete Matrixmaterial beeinflussen entscheidend die Druckqualität. In dieser Arbeit wird ein kommerziell erhältliches magnetisches isotropes Pulver (MQP-S-11-9 von Magnequench Corporation) in einer PA11/PA12 Matrix verwendet. Das Material wird – für den 3D-Drucker übliche Stangenform – extrudiert. Detaillierte Messungen der magnetischen und mechanischen Eigenschaften werden durchgeführt und bewertet.

Um das magnetische Feld der gedruckten Magneten zu vermessen wird der Drucker zu einem 3D Magnetfeld Messsystem aufgerüstet. Mittels eines speziellen Kalibrier-Algorithmus entfällt das adjustieren des 3D Hall Sensors. Ein weiteres Upgrade ermöglicht das Erzeugen von magnetische Pixeln („maxels“) auf die Oberfläche des gedruckten Objektes.

Um Magnete mit einer speziellen Magnetfeldverteilung erzeugen zu können, wer-

den spezielle Simulationswerkzeuge vorgestellt. Mittels Finite-Elemente-Methoden und eines Inversen Streufeldcodes kann die Dichte des Magnetmaterials berechnet werden. Zusätzlich wird ein Topologieoptimierung vorgestellt mit welcher die Geometrie des Magneten berechnet werden kann. Detaillierte Tests dieser Methoden zeigt eine gute Übereinstimmung mit analytischen Lösungen.

Verschiedenste Anwendungen aus dem Bereich der Messtechnik zeigen die Effektivität des 3D-Druckes von polymer gebunden Magneten. Mittels den Simulationswerkzeugen werden spezielle Magnetgeometrien berechnet, anschließend gedruckt und vermessen. Diese Arbeit beschreibt daher den kompletten Entwicklungsablauf von der Entwicklung der 3D-Drucktechnologie über die speziellen Simulationstools bis zur Anwendung der Magneten.

Abstract

Additive manufacturing has become the de-facto standard in industrial production. The “industrial revolution out of the printer” is seen as having enormous potential. Workpieces can be produced directly from form-neutral products such as powders or filaments without the aid of tools. A large number of different additive manufacturing methods are currently available on the market.

Up to now, no additive manufacturing of magnetic materials has been possible. Although, there is a big market potential for special designed permanent magnets that generate a special magnetic field.

The aim of this dissertation is to process polymer-bounded rare-earth (NdFeB) materials by using a commercial 3D printer. An advantage of our printer is the possibility to mix two different materials. Printer settings and matrix material properties have a decisive influence on the print quality. This work uses a commercially available magnetic isotropic powder (MQP-S-11-9 from Magnequench Corporation) in a PA11/PA12 matrix. The material will be extruded to filaments, which is the common source-material for 3D printers. Detailed measurements of the magnetic and mechanical properties are carried out and evaluated.

In order to measure the magnetic field of the printed magnets, the printer is upgraded to a 3D magnetic field mapping system. A special calibration algorithm elaborate an adjustment of the 3D Hall sensor. By means of a further upgrade, magnetic pixels (“maxels”) can be written on the surface of the printed object.

In order to produce magnets with a special magnetic field distribution, special simulation tools are presented. The density of the magnetic material can be calculated using a finite element method and an inverse stray field code. In addition, a topol-

ogy optimization procedure is presented to calculate the geometry of the magnet for a predefined magnetic field distribution. Detailed tests of these methods show a good agreement with analytical solutions.

Various applications in measurement technology show the effectiveness of 3D printing of polymer bonded magnets. Using the simulation tools, special magnet geometries are calculated, printed and measured. Therefore, this work describes the complete development process from the development of 3D printing technology to special simulation tools and the application of such magnets.

Abbreviations

ABS	acrylonitrile butadiene styrene	FFC	FEniCS form compiler
ADC	analog-to-digital converter	GMR	giant magnetoresistance
AM	additive manufacturing	I ² C	inter-integrated circuit
AVM	adjoint variable method	IM	injection molding
BEM	boundary-element method	JIT	just-in-time
BJ	binder jetting	LOM	laminated object manufacturing
CAD	computer-aided design	MJ	material jetting
CAM	computer-aided manufacturing	NC	numerical control
CT	computer-tomograph	PA	polyamide
DAQ	data acquisition	PC	polycarbonate
DIN	german institute for standardization	PCL	polycaprolactone
DMA	dynamic mechanical analysis	PDE	partial differential equation
DUT	device under test	PET	polyethylene terephthalate
EBM	electron beam melting	PFM	pulsed field magnetometer
FDM	fused deposition modeling	PJ	photopolymer jetting
FEM	finite element method	PLA	polylactide
		PP	polypropylen

PPMS	physical properties measurement system	SNR	signal-to-noise ratio
PPS	polyphenylensulfid	SQID	superconducting quantum interference device
PTFE	polytetrafluoroethylene	STL	standard tessellation language
PVA	polyvinyl acetate	TGA	thermal gravimetric analysis
RE	rare-earth	TPE	thermoplastic elastomer
ROI	region of interest	UFL	unified form language
SEM	scanning electron microscope	USB	universal serial bus
SLA	stereolitography	VSM	vibrating sample magnetometer
SLM	selective laser melting	VTK	visualization toolkit
SLS	selective laser sintering		

Contents

1	Introduction	1
1.1	Motivation	1
1.2	Structure of the Dissertation	2
2	Fundamentals and Related Work	5
2.1	Additive Manufacturing	5
2.1.1	Additive Manufacturing Principles	7
2.1.2	Challenges and Perspectives of AM	10
2.2	Magnetism	13
2.2.1	Magnetic Properties	13
2.2.2	Magnetic Hysteresis	14
2.2.3	Magnetic Anisotropy	16
2.2.4	Magnetic Materials	17
2.3	Polymer Bonded Magnets	19
2.3.1	Overview of Highly Filled Compounds	20
2.3.2	Matrix Materials	21
2.3.3	Compound Properties	21
2.3.4	Packing Density	25
2.3.5	Compound Production	26
2.3.6	Conventional Processing Techniques	27
2.4	Additive Manufacturing of Magnets	29
3	Experimental Setup	31
3.1	3D Printer	31
3.1.1	Main Features of the 3D Printer	31
3.1.2	Slicer	33

3.1.3	Printer Parameters	34
3.2	3D Magnetic Field Scanner	35
3.2.1	Introduction	35
3.2.2	Sensor Characteristics and Data Processing	37
3.2.3	Upgrade 3D Printer	38
3.2.4	Measurement Software	39
3.2.5	Calibration Routine	43
3.2.6	Benchmark Measurement	45
3.3	“Maxel” Printer	46
3.4	Magnetization	50
4	Materials	51
4.1	Introduction	51
4.2	Source Materials	51
4.2.1	Prefabricated Compound	52
4.2.2	NdFeB Powder	52
4.2.3	Feedstock Production	53
4.3	Filament Extrusion	54
4.4	Filament Quality	55
4.5	Material Characterization	57
4.5.1	Thermogravimetry Analysis	57
4.5.2	Volumetric Mass Density of Printed Structures	59
4.5.3	Magnetic Properties	61
4.5.4	Tensile Test	66
4.5.5	Dynamic Mechanical Analysis	69
5	Simulation Framework	71
5.1	Introduction	71
5.2	Stray Field Computation	72
5.2.1	Demagnetization Field	72
5.2.2	Finite-Element Method	74
5.2.3	Implementation in FEniCS	77
5.2.4	Validation and Numerical Experiments	79
5.3	Inverse Stray Field Simulation	84

5.3.1	Adjoint Variable Method	84
5.3.2	Implementation in FEniCS & Dolfin-Adjoint	87
5.3.3	Validation and Numerical Experiments	88
5.4	Topology Optimization	90
5.4.1	Methodology	90
5.4.2	Validation and Numerical Experiments	92
6	Applications	96
6.1	Introduction	96
6.2	Magnetic Speed Wheel Sensing	96
6.2.1	3D Printed Back-Bias Magnet	97
6.2.2	Reconstructed Topology	98
6.3	Magnets with a Variable Magnetic Compound Fraction	99
6.3.1	Reconstruced Magnetization Distribution	99
6.3.2	Tailored Magnetic Stray Field	101
6.4	Linear Position Measurement Setup	104
6.5	Magnetic Scale	108
6.6	Larmor Spin-Rotator	108
6.6.1	Current Setup	110
6.6.2	Optimized Designs	112
6.6.3	Validation	115
7	Conclusion & Outlook	118
7.1	Conclusion	118
7.2	Outlook	120
A	Appendix	121
	Bibliography	123

1 Introduction

1.1 Motivation

Additive manufacturing (AM) or 3D printing processes offer many advantages and additional benefits compared to conventional manufacturing processes. These processes, which first emerged in the mid-1980s, have undergone considerable improvements in quality, precision and material selection in recent years. Since 2006, there has also been an increase in the number of low-cost 3D printers for home use. The accessibility of 3D printers for both industrial and general public use has grown dramatically in the past decade. Worldwide sales in the 3D printing sector that include the devices, materials and services for industrial-scale to consumer-based printers have grown to \$ 6 billion in 2017 [1]. AM creates an object layer-by-layer by adding material instead of subtracting it like a conventional manufacturing process. It has the possibility to create single-unit structures with a huge variety of different materials that have been impossible to build previously.

Permanent magnets and its applications have another, or even a bigger influence on our daily life. They are found in almost every modern product ranging from speakers to electrical motors, medical diagnostic systems to wind turbines. Permanent magnets that can be used in industrial applications were developed in the 20th century. Due to intensive research efforts, the maximum energy density of such magnetis is 60 times higher than 90 years ago. The global market of permanent magnets grow to \$ 15 billion in 2018 [2]. Since the 1970's another form of magnet has become important, the bonded magnet. Bonded magnets opened a new world of application possibilities. Originally developed with elastomers and ferrite powder to make flexible magnetic materials. Nowadays, a large variation of different binders and magnetic powders, ranging from inexpensive ferrites to high-performance anisotropic NdFeB materials are available.

Different manufacturing methods like injection molding, calendaring or compressing exist to form these kind of magnets. Magnets with a complex geometry and even with a defined magnetization distribution can be produced easily. Bonded magnets claim around 10 % of the global permanent magnets market sales.

All manufacturing methods for bonded magnets have the same weak point, they are not suitable for single-unit production. This leads to the first motivation of this dissertation, use the possibilities of additive manufacturing methods, to create polymer-bonded permanent magnets with a specific complex geometry. In times of tight budgets, low-cost but effective methods are the first choice. Therefore, the well-established, low-cost 3D printers for home use are the preferred method. Suitable compounds of thermoplastics and magnetic powders should be found and investigated. To measure the field of the printed magnets, a 3D field scanner would be necessary. The XYZ-table and controller of the 3D printer can be used to upgrade the printer to a full 3D magnetic field scanner.

The opportunity to create magnetic structures of arbitrary shapes opens up a new world of magnetic system designs. This leads to the second motivation of this thesis; a simulation framework to solve the inverse stray field problem of permanent magnetic systems is desired. With such a simulation tool, the topology and/or the magnetization distribution of a permanent magnetic system that generate a predefined field in a defined volume outside the magnet can be calculated. The idea is to find a suitable magnetic design for a specific problem and print it with our 3D printer setup directly. Afterwards, the 3D printed and magnetized samples can be characterized by the field scanner.

1.2 Structure of the Dissertation

This thesis is divided into two main parts. The first part describes the experimental work of additive manufacturing of polymer-bonded magnets by the aim of a commercial fused deposition modeling 3D printer. Suitable compounds of thermoplastic binders and isotropic NdFeB magnetic are investigated and characterized. To measure the external magnetic field density of the printed magnets, the 3D printer is upgraded to full-automated 3D magnetic field scanner. To avoid an exact positioning of the sensor, a calibration routine based on detailed field measurements is presented. In the

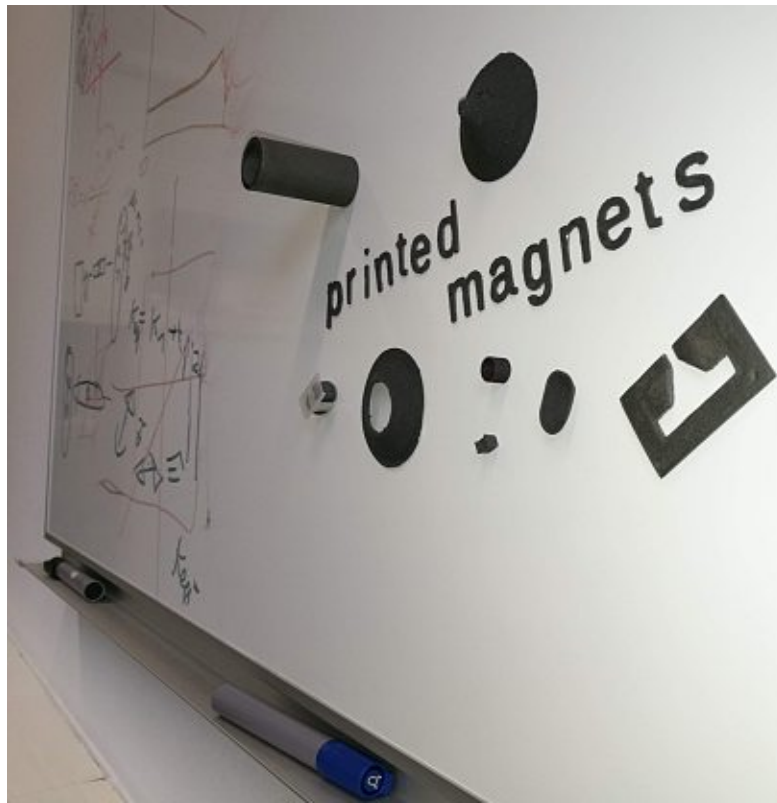


Figure 1.1: 3D printed magnets on a whiteboard.

second part, we introduce a finite element method (FEM) simulation framework to calculate the topology and magnetization distribution, of a magnetic system respectively in order to create a tailored magnetic field. Several problems in the fields of magnetic sensing devices, position measurements, and neutron interferometry experiments are explored. With our simulation tools, optimized magnetic designs are found and physically fabricated with the 3D printer setup.

In every particular,

- **Chapter 2** gives a short introduction into the currently most relevant additive manufacturing (AM) methods, and the challenges and perspectives of AM. Then, some of the basics in magnetism are discussed in general and for polymer-bonded magnets in detail. The current status of AM technologies of magnetic materials with its advantages and disadvantages are reviewed.

- **Chapter 3** describes the 3D printer parameters in general, and the specific features of our setup, as well as the optimized parameters for each material are given. The 3D printer upgrade to a full 3D magnetic field scanner is described. A specific calibration procedure to avoid a complex mounting setup is introduced. To magnetize various regions of a 3D printed structure in different regions, a upgrade to a magnetic pixel (“maxel”) printer is described.
- **Chapter 4** presents the different compound materials for the printing process. At the beginning, prefabricated compounds are described. Mixtures of plastics and magnetic powders are introduced, and the filament production are described in detail. Detailed tests on their physical, magnetic, and mechanic behaviors are performed and discussed.
- **Chapter 5** introduces a simulation framework to compute the demagnetization field of permanent and soft magnetic materials. Even more, an implementation to solve the inverse stray field problem as well as a topology optimization code is presented. All simulation techniques are implemented with a pure finite element method, based on FEniCS and Dolfin-Adjoint. Several numerical experiments and comparisons with well-known techniques show the effectiveness of the implemented methods.
- **Chapter 6** combines all the previous introduced methods, knowledges and uses it for specific defined applications. The 3D printing process is benchmarked with magnetic speed wheel sensing applications. By the aim of the mixing extruder and the inverse stray field simulation framework, several examples are given for sensing applications. With the “maxel” printer, a magnetic scale for position detection is described. The last application deals with a neutron spin manipulation device. Detailed simulations and measurements shows the effectiveness of the 3D printing technique.
- **Chapter 7** summarizes the dissertation and its conclusions, as well as potential future works in the field of AM of magnetic materials.

Fundamentals and Related Work

2

2.1 Additive Manufacturing

Additive manufacturing (AM), rapid prototyping, or colloquially called 3D printing became known in the 1980s with the enormous growth in computer aided design and manufacturing (CAD/CAM) technologies [3]. A technology that quickly and easy converts CAD data into a workpiece or prototype without expensive manufacturing techniques or molds was desired. The international standardization organization ASTM defines AM as the “*process of joining materials to make objects from three-dimensional (3D) model data, usually layer upon layer, as opposed to subtractive manufacturing methodologies*” [4]. AM is a rapid and price-conscious manufacturing process for production of models, prototypes, patterns, and tools, as well as functional parts with special properties for direct industrial applications. It is called as a generative manufacturing process, which means that the manufacturing is carried out directly based on computer models. The basic idea of AM is always that a CAD object is converted to a triangular mesh form; typical encoded as a standard tessellation language (STL) or similar file. Then, the STL file is sliced into small layers. These layers are converted into a tool path for the AM-machine by the means of a slicing program [5, 6]. The object is fabricated in a layer-by-layer manner of a formless (liquids, powders, etc.) or form-neutral (tape, wire, etc.) construction material by means of thermal or chemical processes. The individual layers are joint together and form bit by bit the finished object. Many different kinds of materials can be processed. Some common used materials are thermo plastics like polylactic acid (PLA), acrylonitrile butadiene styrene (ABS), polyamide (PA12; also called as Nylon 12), and polycarbonate (PC), photo-curable resin, wax, metal/ceramic/polymer powders, adhesive coated sheets, compounds of plastic and metals, as well as new advanced materials. The tool-chain of the AM process is shown in figure 2.1.

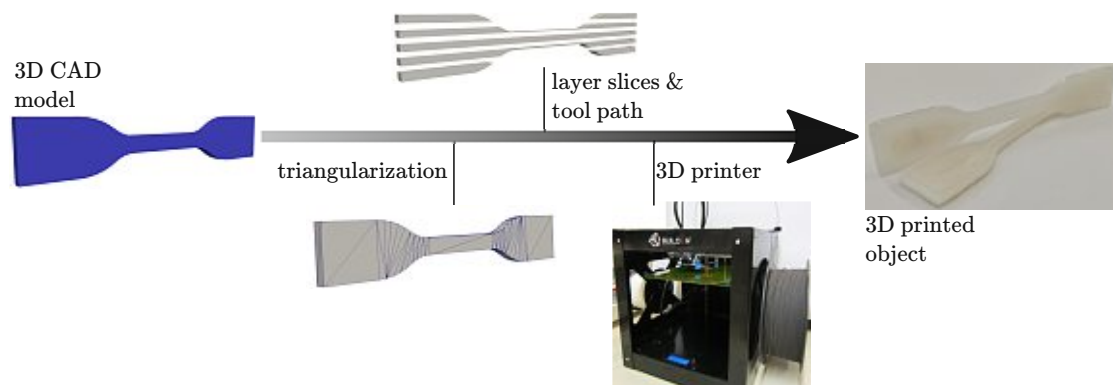


Figure 2.1: Tool-chain of the additive manufacturing process.

Over the last 30+ years AM processes have been investigated and developed [7]. Some of them, among others, stereolithography (SLA) [8], photopolymer jetting (PJ) [9], binder jetting (BJ) [10], fused deposition modeling (FDM) [11], selective laser sintering (SLS) [12], selective laser melting (SLM) [13], electron beam melting (EBM) [14], material jetting (MJ) [15], and laminated object manufacturing (LOM) [16]. In this three decades, the industry and the research community applied these AM processes in the automotive [17], aerospace [18], biomedical [19,20], and many other fields. Figure 2.2 shows a classification of these AM methods on their basic principle.

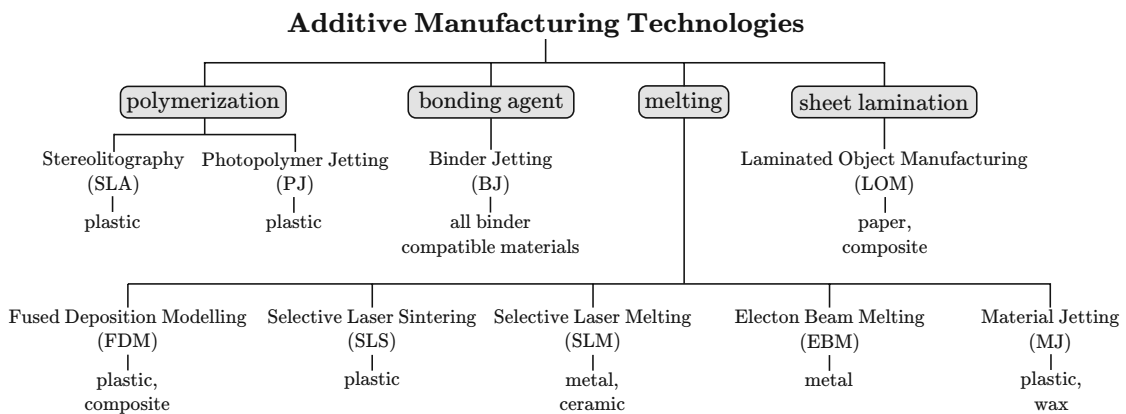


Figure 2.2: The most important additive manufacturing technologies classified on their basic principle.

2.1.1 Additive Manufacturing Principles

As pictured in figure 2.2, additive manufacturing can roughly classify into four basic principles. This section gives a brief overview of these techniques.

Polymerization

Additive manufacturing by means of polymerization uses photopolymers for the manufacturing process. The construction material is liquid in its initial state, when it is irradiated with ultraviolet (UV) light, the phase of the material changes from liquid to solid. A typical photo-curable resin as printing material is the acrylic or epoxy resin. Polymerization is the chain reaction that links molecules to macromolecules (polymers). This process produces a cured, interlinked plastic from a liquid mixture of monomers [21]. All photopolymerisation processes work basically with the same technique, but differs in the procedure.

Stereolithography (SLA) was the first commercially available AM technology. The layers of the sliced CAD model is scanned by the UV light to cure the resin selectively for each cross-section. The procedure is carried out in a bath filled with the basic monomers of the photosensitive plastic. After each finished layer, the workpiece is lowered by one layer thickness. Then, the resin sweeps across the cross-section of the partly finished object, and coating it with a new layer of fresh resin. This layer is scanned and cured-on the previous hardened layer. Figure 2.3(a) shows the principle of SLA.

Photopolymer jetting (PJ) uses a movable ink-jet printer head that generates jets of the UV curable liquid resin. The printer head builds each single layer, followed by a UV lamp curing of the deposit resin. When one layer is finished, the builder platform is lowered by one layer and the next layer is build upon the previous layer. A sketch of this technology is pictured in figure 2.3(b).

Bonding Agent

Binder jetting (BJ) is an AM process that builds the part in a bed of the construction powder. A movable ink-jet printer head sprays a liquid binder at selected points to form the workpiece layer-by-layer. An advantage of this method is that many different materials as well as composites of powder materials can be used. Due to the binder, the produced parts made by BJ are limited in their maximum volumetric mass density and

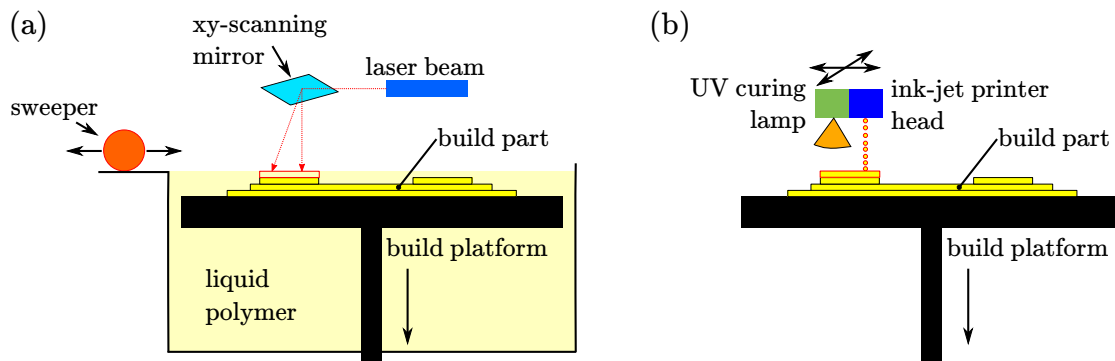


Figure 2.3: AM processes that use polymerization to form an object. (a) Stereolithography (SLA). (b) Photopolymer jetting (PJ).

their mechanical resilience. Post-processing techniques like sintering or infiltration can be applied to increase the density and the mechanical properties of the structures [22]. Figure 2.4 shows the principle of BJ.

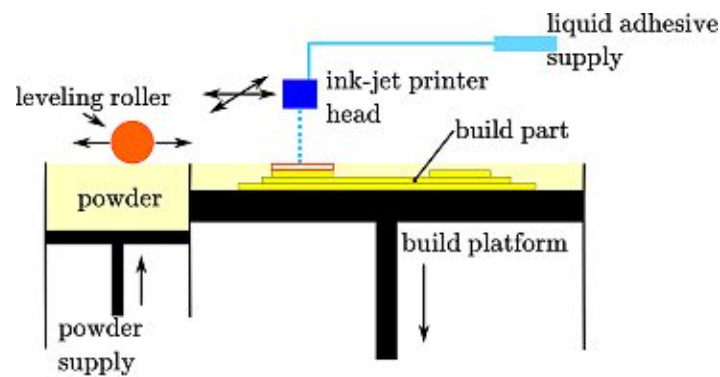


Figure 2.4: Binder jetting (BJ) uses a binder agent to join the powder together.

Melting

Five processes involve the melting and subsequent solidification of the construction material. The first one is the fused deposition modeling (FDM) technique, it is the most popular low-cost, end-user 3D printing process. Stratasys Inc. (USA) developed it in the 1980s. Nowadays, many different types and manufacturer exist. The open-source *replicating rapid prototyper* (RepRap) project developed a low-cost 3D printer, that can print most of its own components by themselves [23]. This triggered a boom of new possibilities in the field of AM. This system uses meltable thermoplastic (PLA, ABS,

etc.) or a compound material (e.g. PA12+metal powder) as construction material. By the aid of a movable extruder with a heated nozzle on its end, the wire-shaped plastic is heated up slightly above its softening point. Molten thermoplastic is pressed out of the printer head nozzle and builds up the object layer-by-layer on the already solidified material on the building platform. Advances have been made by using multi-nozzle or mixing-extruder systems, where each nozzle extrude a different material or mixing different materials together in order to print objects with special properties [24,25]. Figure 2.5 shows a sketch of the FDM principle.

The next three processes are selective laser sintering (SLS), selective laser melting (SLM), and electron beam melting (EBM). All of them working on the same principle. The object is build out of the construction powder layer-by-layer by a localized heat source. After each finished layer, the workpiece is lowered by one layer thickness. Then, a new layer of powder is spread on the top of the object and selectively sintering or melting the powder by scanning the cross-section. SLS and SLM use a focused laser source, EBM uses an electron beam as a heat source. The difference of these techniques is their maximum energy of the heat source. SLS uses a carbon dioxide (CO₂) laser, and SLM a high-power laser beam usually an ytterbium fiber (Yb:YAG) laser with hundreds of watts [26]. The electron beam of EBM has the highest energy density of these methods. SLS selectively fuses and sinters polymer particles or coated metal/ceramic powders. A post processing is necessary to remove the coating. SLM completely melts the metal/ceramic powder by the aid of the high-power laser source. The manufactured object is completely dense. EBM has the same area of application, but due to the higher energy density of the electron beam, it has higher building rates. A sketch of these methods is shown in figure 2.5(b).

The last method is Material Jetting (MJ), it is similar to photopolymer jetting, but instead of a curable liquid resin, the construction material is heated up above its melting point and jetted onto the build surface or platform, where it cools and solidifies. Wax or plastic with a low viscosity are processable. The technique is sketched in figure 2.5(c).

Sheet Lamination

The last manufacturing process that will be discussed in this work is the laminated object manufacturing (LOM) process. The construction material for this process is sup-

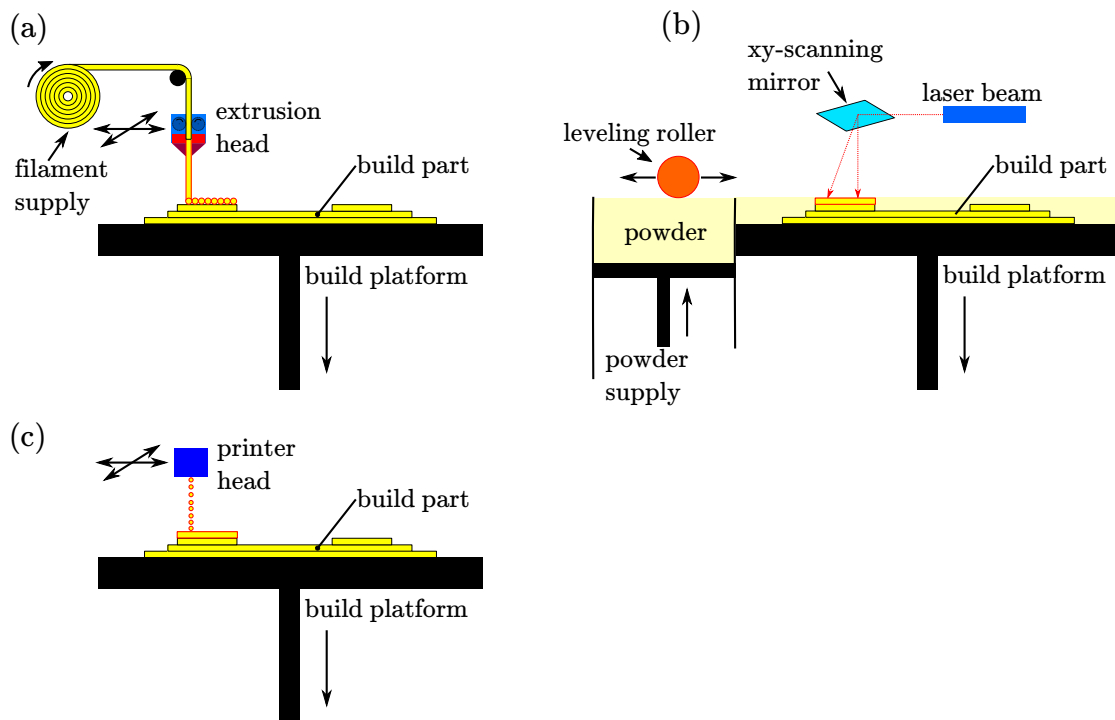


Figure 2.5: The workpiece is created by melting the construction material together. (a) Fused deposition modeling (FDM). (b) Selective laser sintering (SLS), selective laser melting (SLM), electron beam melting (EBM) (instead of a laser source and a xy -scanning mirror, an electron beam source and lenses are used.) (c) Material jetting (MJ).

plied in sheet or foil form. The material can be layers of adhesive-coated paper, plastic, ceramic, or metal. The cross-section of each layer of the workpiece is cut out of the foil and attached on the previous layer. A laser cuts out the contour of the movable foil, and a hot roller bonds the the layer coating together subsequently. With this method, a high process speed is achievable because the laser has to scan only the contour of the layer. Figure 2.6 shows the working principle of the method.

2.1.2 Challenges and Perspectives of AM

Initially created as a method for rapid prototyping, AM has grown into a true manufacturing process. AM giving scientists, engineers and companies the ability to both prototype and manufacture end-use products and it offers significant advantages over traditional manufacturing processes. These advantages include enabling mass customization, increasing design freedom, allowing the reduction of assemblies, and can serve as

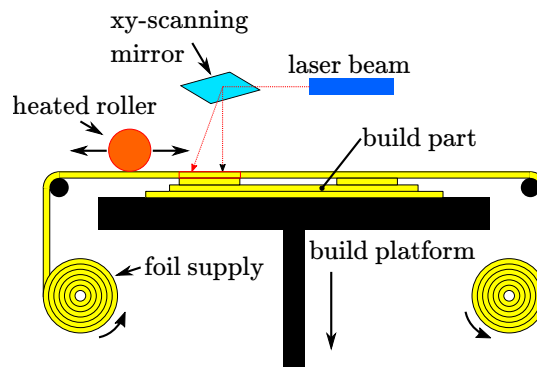


Figure 2.6: Laminated object manufacturing (LOM) uses a cut-out of the cross-section in the sheet of the building material to form the end product.

a cost-effective low volume production process. At the same time, there were people citing disadvantages of AM as well.

The fact that products or objects are produced one at a time in AM gives us the benefit of maximum customization potential. However, the same fact also gives us one of the most potent disadvantage of AM processes i.e. the absence of economies of scale. Economies of scale can be defined as mass production improves the profit margin of manufacturers. Figure 2.7 compares a hypothetical break-even analysis of conventional and AM processes.

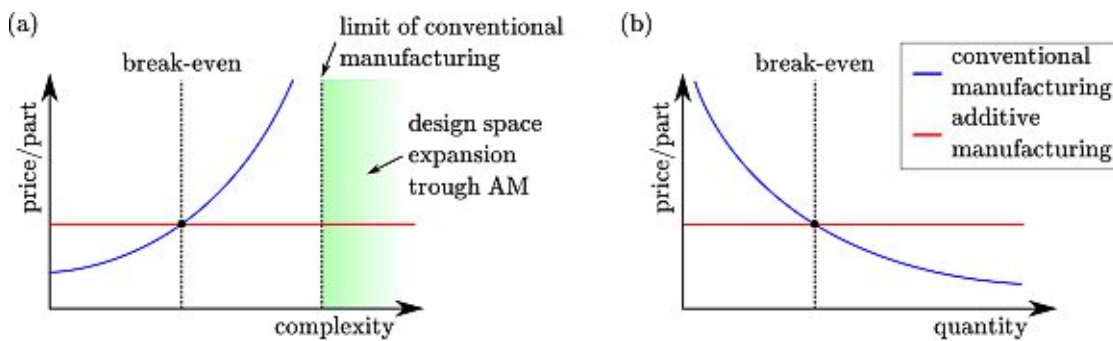


Figure 2.7: Hypothetical break-even analysis comparing conventional and AM processes. (a) Up until a break-even point, it is more economical to use a conventional manufacturing method instead of AM of the part. At some point, the complexity reaches a level where parts can be only manufactured by AM processes. (b) For mass-production, conventional manufacturing methods are more economical.

Poor surface roughness is one of the main limitations of AM processes. Surface condition is an important design criteria in applications involving friction, lubrication, and

wear [27]. Surface finish is mainly influenced by tessellation of the original CAD model and slicing during the manufacturing process [28]. Slicing generates the contour in the xy -plane. The z -direction results from single layers being stacked up on top of each other. This means, the tolerances of AM parts are small in xy -direction, but leads to a stair-stepping effect in the z -direction. By reducing the layer thickness, the surface roughness is better but this increases the build time significantly. Post processing of the surface can improve the surface condition, but this also increases the building time, as well as this changes the geometrical definition of the model. Errors due to tessellation and slicing of an example is pictured in figure 2.8.

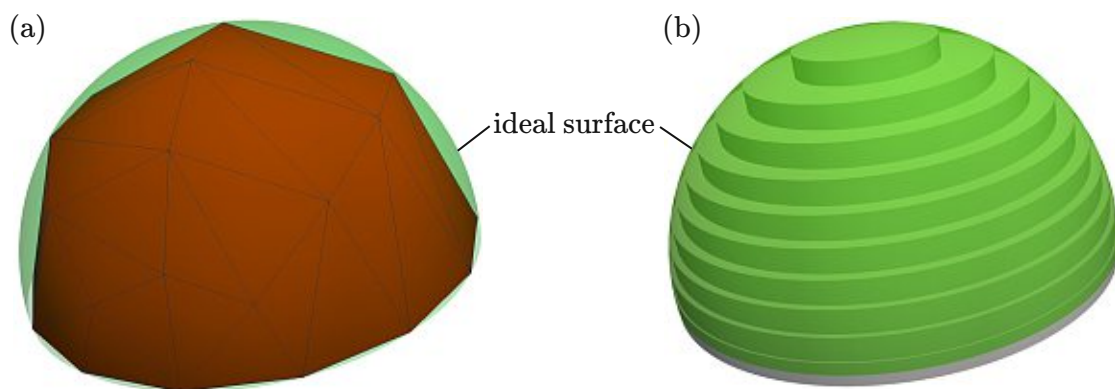


Figure 2.8: Errors due to tessellation and slicing of the original CAD file. (a) Chordal error as the result of tessellation of the surface of a CAD model. (b) Staircase effect in AM parts.

It is not easy to select the most suitable manufacturing method for a specific design. In general, it can be summarized that for small quantities, high complex workpieces, parts that need to be customized, and fully assembled components, AM is the best choice. Nevertheless, if material properties and surface finish are of critical importance and the quantities are low, mechanical machining may be a better option. For high quantities and simple plastic parts, injection molding or forming is the best manufacturing process [29]. Table 2.1 lists the advantages and disadvantages of some important additive and conventional manufacturing methods.

The accessibility of 3D printers for both industrial and general public-use has grown dramatically in the past decade. The major challenges at the moment and the future is to increase the accuracy, surface condition, and the number of processable materials, as well as to decrease the costs and the execution time of the process. New composite

Table 2.1: Comparison chart of different additive and conventional manufacturing technologies. Additive manufacturing: SLA: stereolithography, PJ: photopolymer jetting, BJ: binder jetting, FDM: fused deposition modeling, SLS: selective laser sintering, SLM: selective laser melting, EBM: electron beam melting, MJ: material jetting, LOM: laminated object manufacturing. Conventional manufacturing: CNC: computerized numerical control machine, IM: injection molding, F: forming, J: joining. (Table adapted from [30–33])

	additive manufacturing									conventional manufacturing			
	SLA	PJ	BJ	FDM	SLS	SLM	EBM	MJ	LOM	CNC	IM	F	J
cost- low volume	✓	✓	✓	✓	✓	✓	–	✓	✓	–	×	×	×
cost- high volume	×	×	×	×	×	×	×	×	×	×	✓	✓	–
lead time	✓	✓	✓	✓	✓	✓	✓	✓	✓	✓	×	×	×
material selection	–	–	✓	–	–	–	–	×	×	✓	–	✓	✓
surface finish	–	–	×	×	–	–	–	×	–	✓	✓	✓	✓
tolerance	✓	✓	×	×	–	✓	✓	×	–	✓	✓	✓	✓
integrated assembly	✓	✓	✓	✓	✓	✓	✓	✓	–	×	×	×	×
complexity	✓	✓	✓	✓	✓	✓	✓	✓	✓	–	–	×	×
customizability	✓	✓	✓	✓	✓	✓	✓	–	–	✓	×	×	×

✓ is good, – is fair, × is poor

materials may offer greater opportunities to extend the present limitations of materials in AM.

2.2 Magnetism

In order to understand the experimental investigations and the calculation methods of this work, it seems necessary to examine some of the basics of magnetism more in detail. These basics will be limited to topic-specific areas, and do not claim to provide a complete description of all magnetic effects.

2.2.1 Magnetic Properties

A material introduced into a magnetic field, leads to an interaction between the field and the atomic properties of the material. This result in a deviation of the magnetic field inside the material compared with the external magnetic field. Atomic, magnetic spin and orbital moments are generated by the rotation of the electrons in the material around the atomic nucleus. These spin- and orbital moments of an atom represent the smallest magnetic elementary entity (magnetic dipole), it is described by its dipole moment. The material-specific electron structure means that each material has fundamentally different magnetic properties. Five types of magnetism can occur in solid

states (diamagnetism, paramagnetism, ferromagnetism, antiferromagnetism, and ferrimagnetism) [34].

Ferromagnetic materials are of particular technical importance. The magnetic moment of individual particles are not independent of each other, but they are spontaneously parallel aligned. The coupling of the magnetic moments inside the material is not a long range effect, it is limited to small areas (magnetic domains) [35]. The magnetic domains are aligned to form a minimum energy state. This means that the entire body appears as non-magnetic. The domains can be aligned by an external magnetic field. This orientation of permanent magnets is fixed even after the external field has been removed, so that a permanent magnetization of the material is obtained. If the material is heated up above its ferromagnetic Curie temperature, the magnetic properties of the material changes from a ferromagnetic to a paramagnetic behavior.

If a magnetic material is inside a magnetic field strength \mathbf{H} , the atomic dipole moments \mathbf{m} are aligned parallel to \mathbf{H} . This leads to a magnetization of the material. The magnitude and direction of the magnetization \mathbf{M} results in

$$\mathbf{M} = \frac{d\mathbf{m}}{dV} \quad (2.1)$$

with the volume V of the material. The magnetization \mathbf{M} has the unit (A/m).

The magnetization describes the relationship between the magnetic flux density \mathbf{B} and the magnetic field strength \mathbf{H} inside the material

$$\mathbf{B} = \mu_0 (\mathbf{H} + \mathbf{M}) = \mu_0 \mu_r \mathbf{H} = \mu \mathbf{H} \quad (2.2)$$

where μ_0 is the vacuum permeability ($\mu_0 = 4\pi \times 10^{-7}$ Vs/(Am)), μ_r is the relative permeability, and $\mu = \mu_0 \mu_r$ is the permeability (for ferromagnetic materials: $\mu \gg 1$). In general, μ varies with the magnetic field ($\mu(H)$). For technical calculations and applications, the German Institute for Standardization (DIN 1324-II) gives eleven different definitions of $\mu(H)$. The magnetic flux density $\mu_0 \mathbf{M}$ is also known as magnetic polarization \mathbf{J} with the unit (T).

2.2.2 Magnetic Hysteresis

If an initially ferromagnetic but non-magnetic body is magnetized by an increasing applied magnetic field H , an increasing flux density B can be observed in the material.

The correlation between the two quantities is non-linear and it saturates B_s when the field strength H is sufficiently high (initial magnetization curve). If the field strength decrease again, the magnetization will no longer run back on the initial curve. Instead, it decreases less and at $H = 0$ A/m, a magnetization or remanent field B_r remains - it has become a permanent magnet, due to its ferromagnetic behavior under the influence of H . In order to generate a non-magnetic state in the material ($B = 0$ T) after magnetization, a magnetic counter-field, the so-called coercive field strength H_c must be applied. It is a material-specific value and it is a criterion of the robustness of the magnetic flux density against external magnetic fields. A further reduction of H leads to a negative saturation of the material. The coercive field strength H_c is smaller as the intrinsic coercive field strength H_{cJ} . This is the magnetic field strength that is required to reset the polarization J or magnetization M to zero, and it is a criterion of the inherent stability of the magnetic properties of a material. Figure 2.9(a) shows a typical hysteresis curve for a permanent magnetic material.

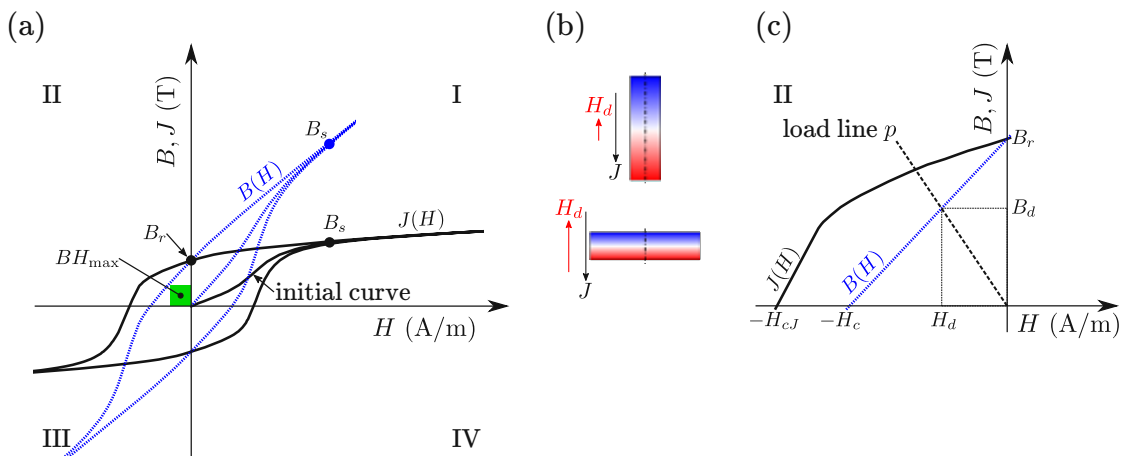


Figure 2.9: (a) Hysteresis curve for a typical hard magnetic material. B_r is the remanence at $H = 0$, H_{cJ} is the intrinsic coercivity (i.e. the reverse field that reduces the polarization $J(H)$ to zero), H_c is the coercivity (i.e. the reverse field required to reduce the magnetic flux density $B(H)$ to zero), B_s is the saturation magnetization, $(BH)_{\max}$ is the maximum energy product. (b) Shape of a magnet and its demagnetization field for a low and high D/h ratio. (c) II. Quadrant of the hysteresis loop with a load line p .

To compare different magnetic materials, the energy density w is a crucial factor. If the permeability μ is constant in the II quadrant, the energy density $w = \int H dB$ is proportional to the product of the magnetic flux density B and the magnetic field H on the $B - H$ curve (figure 2.9(a)). Then, the maximum energy product $(BH)_{\max}$ is with

$$H = B/\mu$$

$$(BH)_{\max} = \frac{1}{2\mu} B_r^2 \quad (2.3)$$

with the unit kJ/m^3 .

2.2.3 Magnetic Anisotropy

Magnetic anisotropy describes that magnetic materials may have a preferred direction for magnetization. Here, two sources of magnetic anisotropy are important and will be discussed. For permanent magnetic system, the magnetic flux density also depends on the geometry of the system (also called as shape anisotropy). It is important to consider the shape anisotropy for microscopic grains (i.e. magnetic powders), as well as for macroscopic magnetic structures. The magnetization of the material itself generates a magnetic field in the opposite direction of the magnetization direction, this is the demagnetization field H_d . The magnitude of this demagnetization field H_d is proportional to the polarization J and is expressed as

$$H_d = -N \frac{J}{\mu_0} \quad (2.4)$$

with the demagnetization factor N ($0 \leq N \leq 1$). N is determined by the shape of the magnetic body (the sum of N along the major axis is: $\sum_{i=1}^3 N_i = 1$). N decreases with the relative height h of the magnet in relation to its diameter D . Figure 2.9(b) shows a sketch of a magnet with a high D/h (magnetized along easy axis) ratio and its low demagnetization field H_d , and a magnet with a low D/h (hard axis) and a high H_d , respectively.

Practically, analysis of the magnetic behaviors of magnetic structures use the $B-H$ hysteresis curve. Therefore, instead of this demagnetizing factor N , the permeance coefficient p defined as

$$p = -\frac{B_d}{\mu_0 H_d} \quad (2.5)$$

is used. In figure 2.9(c) the II. quadrant of the hysteresis curve with a load line p is shown. The intersection between p and $B-H$ curve is defined as the operating point of a magnet. The permeance coefficient p is determined by the shape of the magnetic body, just like the demagnetizing factor N . The relationship between p and N is

$$p = \frac{1 - N}{N} \quad (2.6)$$

The second source for anisotropy is the magnetocrystalline anisotropy. It is an intrinsic property of a ferromagnet single crystal, independent of grain size and shape.

In simple terms, it is not possible to magnetize a single crystal along the hard axis. In other words, the magnetization along the hard axis is reversible, therefore theoretically no hysteresis appears. These directions are usually related to the principal axis of its crystal lattice. Practically, the shape and the magnetocrystalline anisotropy occur together. The total magnetic easy axis does not necessarily has to correlate with the easy axis of the geometric shape [36]. If we consider an alignment of magnetic particles, e.g. in a plastic binder, this refers to the orientation of the particles easy axis along the external magnetic field inside the binder.

If the magnetic easy axis of the particles in a magnet are stochastic distributed, the magnetic properties do not depend on the direction of the magnetization field. The material is magnetically isotropic. To estimate the magnetic performance ($(BH)_{\max}$), the Stoner-Wohlfarth model can be used to describe magnetic anisotropic and isotropic materials [37]. The model describes the anisotropy energy and Zeeman energy of a ferromagnetic single domain particle with uniaxial anisotropy in an external magnetic field. For a single Stoner–Wohlfarth particle, where the easy axis is orientated parallel to the external field, the remanence is equal to the saturation magnetization $B_r = B_s$. If the field is orientated along the hard axis, the remanence is zero ($B_r = 0$). For an isotropic material, the particles are randomly oriented. This leads statistically to remanence of $B_r = B_s/2$. Therefore, theoretically B_r and $(BH)_{\max}$ of an isotropic orientated material, respectively, is only 1/2 of the remanence of an anisotropic orientated material.

2.2.4 Magnetic Materials

Magnetic materials are divided into soft and hard magnetic materials regarding to their coercivity strength H_{cJ} . Soft magnetic materials have a H_{cJ} between 10^{-1} and 10^3 A/m or 10^{-7} and 10^{-3} T, respectively. Typical soft magnetic materials are nickel-iron materials ($H_{cJ} \approx 1$ A/m, $B_s \approx 0.8 - 1.2$ T), ferrites ($H_{cJ} \approx 10^3$ A/m, $B_s \approx 0.5$ T), the same H_{cJ} but with a much higher B_s have iron-silicon, pure iron and iron-cobalt materials with a B_s up to 2.5 T [38]. Due to the low H_{cJ} and the high B_s , these materials have a high permeability μ which in turn leads to a low $(BH)_{\max}$ (equation 2.3).

Hard or permanent magnetic materials have a coercivity strength H_{cJ} greater than 10^4 A/m or 10^{-2} T. If a permanent magnetic material is saturated inside a external field, the remanence flux density remains after turning-off the external field. The magnetic properties of the most relevant permanent magnetic materials are shown in figure 2.10.

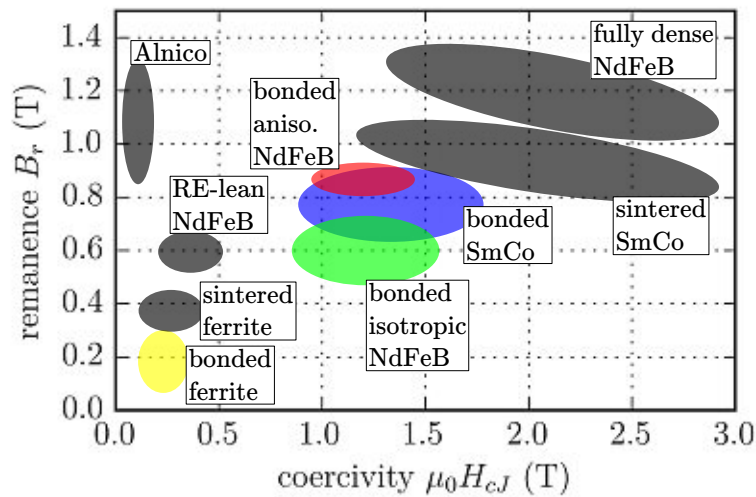


Figure 2.10: Magnetic properties of common permanent magnetic materials. Bonded magnets are colored. (Adapted from [39])

Alnico was invented and commercialized in the early 1940's. It is an alloy made of aluminum (Al), nickel (Ni) and cobalt (Co), it has a high maximum working temperature of around 500 °C. Due to the low H_{cJ} and its high price compared to other materials, applications of Alnico materials are restricted nowadays. Alnico magnets are produced by casting of the liquid alloy or by pressing and sintering metal powders [40].

Ferrite magnets were first commercialized in 1952. Ferrite with a high electrical resistance and chemical resistivity are interesting. Ferrites with a hexagonal crystal structure like barium ($\text{BaO} \cdot 6\text{Fe}_2\text{O}_3$) or strontium ferrite ($\text{SrO} \cdot 6\text{Fe}_2\text{O}_3$) are the first choice. Ferrites are cheap compared with rare-earth (RE) materials. They are made by mixing of the barium or strontium carbonate with Fe_2O_3 at a temperature of about 1200 °C. This material is then ball milled to reduce the particle size, pressed in a die, and sintered at about 1200 °C to make the final magnet [36,41].

Samarium–cobalt was introduced in 1961, it is RE material. Technical relevant are the alloys SmCo_5 and $\text{Sm}_2\text{Co}_{17}$. An advantage of these alloys is the high maximum working temperature of around $300\text{ }^\circ\text{C}$ by a sufficient high H_{cJ} . The SmCo magnetic powder is produced by melting and casting of the alloy, milling to produce a powder with particle size near $10\text{ }\mu\text{m}$. In order to maximize B_r , the magnetocrystalline anisotropic SmCo powder is aligned in a magnetic field so that the easy axis of all the particles are parallel, and then compressed in a die. The compressed powder is sintered above $1000\text{ }^\circ\text{C}$ [42].

The most recently developed magnetic material is neodymium–iron-boron ($\text{Nd}_2\text{Fe}_{14}\text{B}$), it was first available in 1984. It has compared to SmCo materials a lower volumetric mass density and the highest available H_{cJ} and therefore, they have the highest $(BH)_{\text{max}}$ of all currently known materials. Disadvantages of this material are the high price and the low working temperature compared to other materials [43]. NdFeB magnets can be divided into micro and nanocrystalline structures [44]. Microcrystalline NdFeB magnets are produced by casting of the material and milling to a powder of around $5\text{ }\mu\text{m}$. Nanocrystalline NdFeB mostly produced by a melt spinning process. This produces ribbons of flakes with a size of about $200\text{ }\mu\text{m}$ [45]. Inert gas atomization processes produce spherical powder with a particle size of around $45\text{ }\mu\text{m}$. [46]. Each flake or sphere contains many randomly orientated grains with an uniaxial magnetocrystalline anisotropy. This leads to isotropic magnetic properties of the bulk material. For a higher maximum energy product, anisotropic NdFeB is desirable. By means of a hot press (die-upsetting) procedure, an anisotropic structure can be generated [47].

2.3 Polymer Bonded Magnets

On the one hand, sintered magnets have the highest maximum energy product $(BH)_{\text{max}}$; on the other hand, the geometric freedom in shaping of magnetic structures by pressing and sintering is restricted. For this reason, for many applications it is useful to grind a permanent magnet material into powder and embed the particles in a matrix of a plastic or rubber. Completely new geometry shaping capabilities occur with such bounded magnets. By the aid of a proper matrix material, specific mechanical behaviors can be achieved, like flexible bonded magnets with a rubber matrix. Even complex magnetization distributions are possible. Applying an external magnetic field while the the matrix

material is melted, leads to a physical rotation of the particle. This rotation leads to an alignment between the magnetic easy axis of the particles and the external field [36,39]. Another advantage of injection molded polymer-bonded magnets is the possibility to mold the magnet to an object with special mechanical properties such as a shaft or a hub. A crucial disadvantage of bonded magnets is their reduced $(BH)_{\max}$ compared to sintered magnets. However, due to the procedural advantages of plastic technologies, bonded magnets have a wide area of applications in many different industrial fields, it ranges from sensors to various electric drive technologies [48–50].

2.3.1 Overview of Highly Filled Compounds

Compounds of permanent magnetic and plastic materials are just a special application of highly filled compounds. The intentions of applications are fundamentally different. Some examples are:

- Adding additives such as, anti-oxidants to avoid a degeneration of the polymer, or UV-stabilizers to absorbing the UV radiation preferentially, and dissipating the energy as low-level heat [21].
- Mechanical improvement of the component by adding a strengthening component such as glass fibre [51].
- Filling of the matrix material with electrical conductive (i.e. carbon black, aluminum flakes) material to produce electric shielding elements [52].
- The usage of soft magnetic fillers with polymer materials for low frequency and inductive device applications [53,54].

All applications of filled compounds unite the fact that parts of the compound should be produced by forming (i.e. injection molding), but the fillers considerably change the rheological and material properties of the component in contrast to the pure matrix material. In most applications, a maximum filler content is desired, but it is limited by the loss of flowability of the melted compound.

2.3.2 Matrix Materials

For technical applications, the matrix materials for polymer-bonded magnets are mostly thermoplastics, thermosetting polymers, and elastomers (rubber) [39]. Thermoplastic matrix plastics must have a comparatively low processing viscosity and high strength, as well as the matrix should also provide a high elasticity. Polyamide has a good combination of these properties, and is therefore suitable for the processing of highly filled plastics. Especially polyamides such as PA6, PA11, and PA12 are commercially relevant. For applications with an increased operating temperature, polyphenylsulfid (PPS) and polyphthalamide (PA6T) are established [55,56].

Compared to thermoplastic matrix systems, thermosetting polymers compounds have the advantage that their low viscosity allows higher filler contents of up to 85 vol.% and thus higher magnetic properties can be achieved. The magnets also have the material advantages of thermosetting polymers, such as high chemical resistance and increased operating temperatures. On the other hand, due to the required hardening process, the manufacturing process is more complicated [57].

An advantage of elastomer-bonded magnets is their viscoelastic behavior. This can be used to make elastic magnets; a first application for such a magnet was a refrigerator door gasket seal. With an elastomer matrix, magnetorheological materials can be produced. This class of materials can vary their rheological properties by application of an external magnetic field. These kind of materials can be used for vibration isolation applications since their stiffness changes within a magnetic field [58,59].

2.3.3 Compound Properties

The fraction of the filling material has a crucial influence on the characteristic properties of the compound material. In figure 2.11 the qualitative influence of the filling fraction is shown.

Some of the most important physical properties will be described in the next subsections.

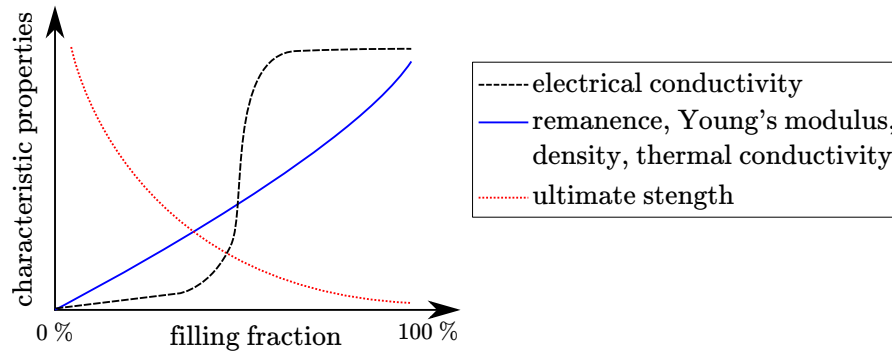


Figure 2.11: Qualitative influence of the filling fraction on the characteristic properties of filled thermoplastics. (Adapted from [60])

Volume Fraction vs. Mass Fraction

Practically, the filling fractions of a compound are listed in mass fractions (wt.%), but to compare the special properties of a compound, the volume fractions (vol.%) of the filler constituents are necessary. The volume fraction ϕ_i of a constituent with the volume V_i is [61]:

$$\phi_i = \frac{V_i}{V} \quad (2.7)$$

with the volume of all constituents of the mixture $V = \sum_{i=1}^N V_i$ prior to mixing. The sum of all volume fractions of a mixture is equal to 1

$$\sum_{i=1}^N \phi_i = 1 \Rightarrow \phi_N = 1 - \sum_{i=1}^{N-1} \phi_i. \quad (2.8)$$

For a binary system with a filler and a matrix material, the relation between filler volume fraction ϕ_f and filler mass fraction w_f is

$$\phi_f = \frac{w_f / \rho_f}{(1 - w_f) / \rho_m + w_f / \rho_f} \quad (2.9)$$

with the densities of the filler material ρ_f and matrix material ρ_m , respectively.

Due to the different densities of the fillers, the same filler volume fraction leads to significantly different filler weight fractions and vice versa. Figure 2.12 shows the relation between volume and mass fraction of a PA12+Sr Ferrite and PA12+NdFeB compound, respectively. The densities are: $\rho_{\text{PA12}} = 1.01 \text{ g/cm}^3$, $\rho_{\text{NdFeB}} = 7.43 \text{ g/cm}^3$, $\rho_{\text{Sr}} = 5.08 \text{ g/cm}^3$. A typical volume fraction of magnetic materials for injection molded (IM) parts is between 50 – 70 vol.%

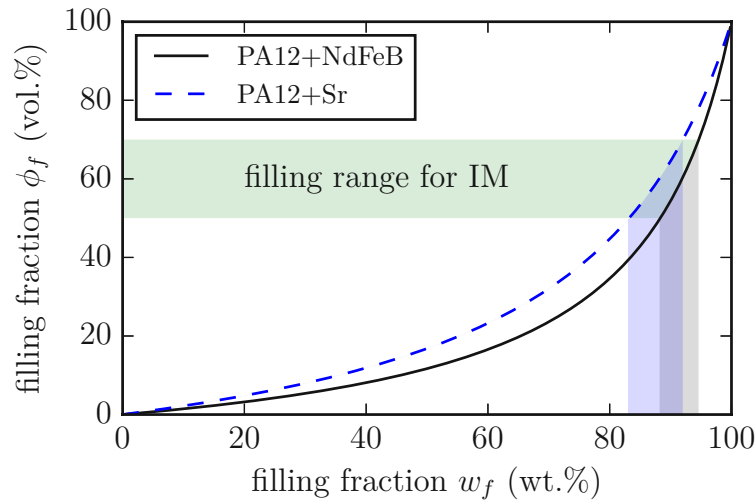


Figure 2.12: Comparison between the filling volume and mass fraction of PA12+Sr-Ferrite and NdFeB compounds, respectively. The filling fraction for typical injection molding (IM) compounds is highlighted.

Rheology

Rheology describes the flowability and flow behavior of matter, primarily of liquids or soft states. The essential variable within the rheology is the viscosity, which defines the required pressure to press a medium through a nozzle, or it defines the maximum flow path length for a given flow cross-section during injection molding. For bonded anisotropic magnetic material, the viscosity is a significant parameter for the alignment behavior of the magnetic particles and thus the resulting magnetic properties. The viscosity can be formulated for different forms of mechanical stresses. For plastic compounds, the shear stress model describes the viscosity reasonable. For low shear rates, the viscosity is almost independent of a change in shear rate, depending on the plastic. This range is also known as zero viscosity. Highly filled compounds usually form no zero viscosity range. As the shear rate increases continuously, this behavior changes and the dependence on shear rate increases significantly. A theoretical description of highly filled compound is complex, or can only approximated by a simplified model.

In the literature, an increase in viscosity due to solid fillers is described [62]. An explanation for a viscosity increase is the model of the inner shear rate. The model is based on a flow channel, which is reduced by the filler particles, whereby the solid

fillers and the polymer are homogeneous distributed over the height of the flow channel. This results in a higher internal shear rate of the polymer at constant external shear rate. Therefore, a higher shear stress is generated at a constant viscosity of the matrix plastic [63].

Mechanical Properties

The mechanical properties are influenced by the filling fraction and particle geometry. To achieve a high Young's modulus, the filler content should be as large as possible and the particle size of the filler should be as small as possible. Additionally, suitable additives can influence the Young's modulus in a good way.

The temperature of the object plays a crucial role. For a given filler fraction, the tensile strength decreases with increasing temperature. Bonded magnets made of melt spun flakes powder have a higher tensile strength compared with bonded magnets made of powder with a spherical morphology [64].

Electrical & Thermal Conductivity

If an electrical conductive filler is added to a plastic matrix, the material becomes conductive as soon as the percolation threshold is exceeded. At the percolation threshold, the particles touch each other and conductive paths are formed. It is shown that when using larger particles, the resistance decreases faster with the same filler content and the same filler [65].

Like electrical resistance, thermal resistance decreases with increasing filler content when suitable fillers such as ceramic powder or carbon fibers are used. The thermal conductivity of the compound can be adjust, as well as the electrical conductivity, by modifying the filler material, filler fraction, and particle size. Plastics with thermally conductive fillers heat up or cool faster with increasing filler content. Compared to electrical conductive compounds, no contact between the particles are necessary [66]. Thermal conductivity is important for additive manufacturing systems that work based on melting of the building material.

Magnetic Properties

To describe the magnetic properties of polymer-bonded magnets, it is important to distinguish between bonded soft and hard magnets. For bonded soft magnets, the relation between coercivity and filler fraction ϕ_f can be described by the equation from Néel [53]

$$H_c(\phi_f) = H_c(0)(1 - \phi_f) \quad (2.10)$$

with the coercivity $H_c(0)$ at a magnetic particle content against zero and the coercivity $H_c(\phi_f)$ for a filler fraction ϕ_f . This relation leads for $\phi_f = 1$ to a coercivity of $H_c(1) = 0$ A/m. H_c for soft magnets is small but not zero. Nevertheless, the relation describes the coercivity of bonded soft magnets very well [67].

The relative permeability μ_c of soft magnetic compounds can be described by the equation from Bruggeman [68]

$$\mu_c(\phi_f) = \frac{\mu_m}{(1 - \phi_f)^3} \quad (2.11)$$

this model assumes that the permeability of the filler material $\mu \rightarrow \infty$ as a basis, as well as that the particles are far away from each other and intersection can be neglected. Therefore, this model is only applicable for low filler fractions ($\phi_f < 0.85$). The permeability of the polymer matrix material is $\mu_m \approx 1$.

The polarization J and remanence B_r , respectively can easily be described by a linear relation

$$J(\phi_f) = J(\phi_f = 1)\phi_f \quad (2.12)$$

The relation for the polarization and remanence is also valid for bonded hard magnetic materials. Compared to bonded soft magnets, the coercivity for bonded NdFeB hard magnets is independent of ϕ_f . The nano-sized NdFeB grains, produced by melt spinning or inert gas atomization are responsible for the coercivity of the compound and there are not changed, or their modification is negligible [69]. This behavior is proofed in section 4.5.3.

2.3.4 Packing Density

To archive a high remanence B_r and $(BH)_{\max}$, respectively, a high filler fraction is desirable. Therefore, the packing density of the filler particles is a crucial parameter. For

a mixture of spherical particles with a unimodal particle size distribution, the highest achievable packing density for a face-centered cubic (fcc) alignment is $\phi_f = 0.74$. For a fcc lattice a cavity, or called octahedral site between the particles accrues. In this octahedral site, a particle with the maximum radius $r = R(\sqrt{2}-1) \approx 0.414R$ can be embedded. For this bimodal particle size distribution in a fcc arrangement, the maximum packing density increase to $\phi_f = 0.81$. Figure 2.13(a) shows a cross section of fcc lattice with a particle in the octahedral site. A fcc lattice arrangement of the particles inside the matrix is almost unlikely. In reality, the particles are statistically distributed. For a bimodal mixture of spherical particles, a maximum density of 86 % can be achieved for a particle size ratio of $R/r = \infty$ and an amount of 70 % large particles [70,71]. Figure 2.13(b) shows the basic behavior of a bimodal mixture of spherical particles. Consider, this relation is only valid for spherical particles. For flakes from a melt spinning process the maximum packing density decrease significant. Figure 2.13(c) shows the qualitative influence of the particles sphericity on the packing density.

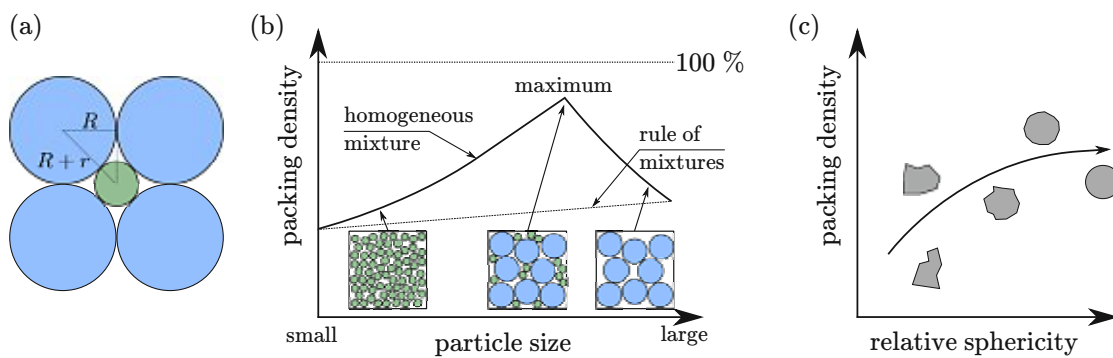


Figure 2.13: Influence of the size distribution and filler morphology on the maximum packing density. (a) Cross section of a face-centered cubic (fcc) lattice with the maximum filled octahedral site. (b) Packing density variation for a bimodal mixture. The homogeneous mixture and the rule of mixtures line gives the theoretical upper- and lower-bound for the packing density. (c) Influence of the relative sphericity of particles of equal size on the maximum packing density. (Adapted from [66,71])

2.3.5 Compound Production

The manufacturing of highly filled polymer-bonded magnets, is carried out by two plastic processing steps. It starts with the mixing of a filler into a plastic matrix material. The second step is the subsequent shaping of the object from the melt. Special mixing equipment is necessary for a homogeneous incorporation of the filler into the matrix.

The compounding process needs to be fast enough to avoid oxidation processes of the magnetic material. Practically, in industrial processes a co-rotating twin-screw extruder is used to mix highly filled compounds [72].

A compound extruder plastifies, mixes, compress, and conveys the plastic through a special screw geometry running in a cylinder. A schematic picture of a twin-screw extruder is shown in figure 2.14. The extruding process can produce endless profiles like filaments for FDM 3D printer, or granules by chopping the compound after the die of the extruder. These granules can be further processed by conventional processing techniques.

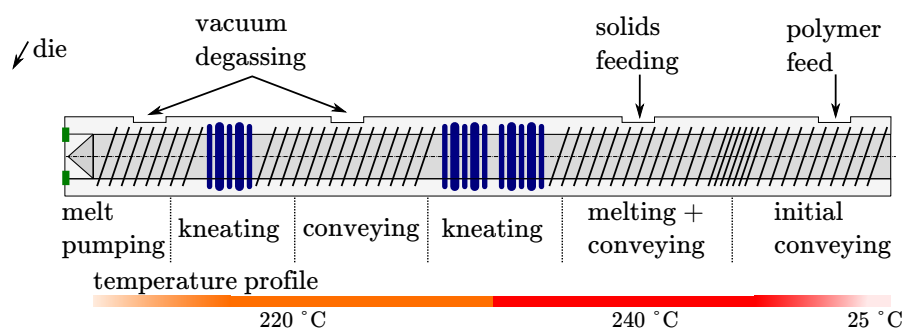


Figure 2.14: Schematic sketch of a twin-screw extruder for compound manufacturing.

2.3.6 Conventional Processing Techniques

The shaping of polymer-bonded permanent magnets is carried out by using conventional, continuous and cyclical plastic processing methods. Continuous processes are extrusion and calendering, cyclical processes are injection molding and compression. Figure 2.15 shows these four manufacturing processes with their used magnetic and binder material. The end product is rigid for compressing and injection molding, and flexible for calendering. Depended on the matrix material, extrusion can produce rigid or flexible parts. Special changes on the forming tool and process control are necessary for processing compounds with magnetically anisotropic fillers. An external magnetic alignment field in the forming tool is required to align the easy axis of the particles along the field. Therefore, a major advantage of isotropic magnetic powders is their simplified fabrication. Since there is no residual magnetization that attract ferromagnetic particles to the magnets, enhanced cleanliness during subsequent handling and assembly operations is obtained. Nevertheless, this leads to a lower $(BH)_{\max}$ compared

to anisotropic materials as discussed above. Due to the high viscosity of the compound, it is difficult to realize long melt flow paths and the forming of complex geometries (compared to additive manufacturing methods) [39,55]. The shaping processes that are important in practice, are briefly explained below.

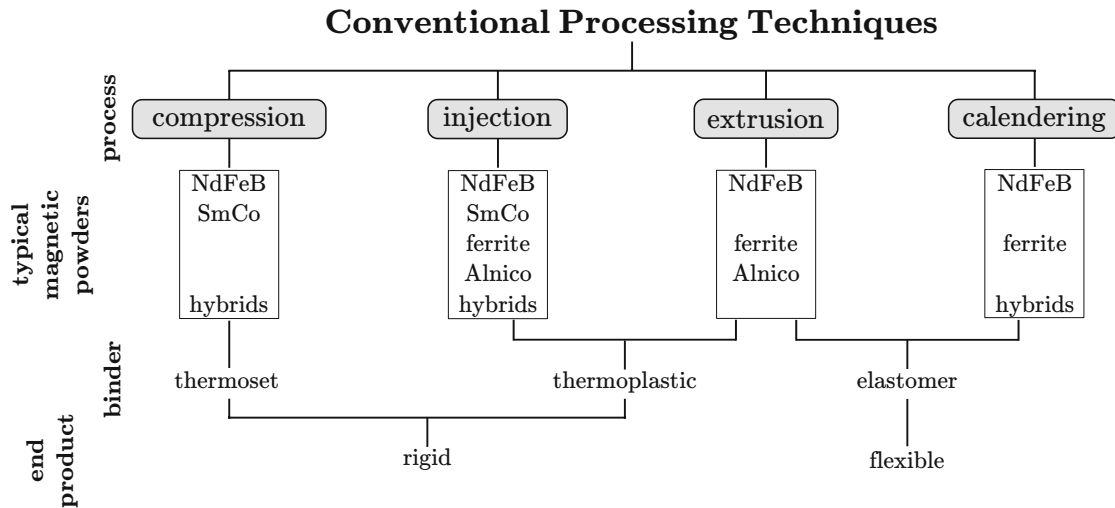


Figure 2.15: Conventional manufacturing methods and their used magnetic and matrix materials. (Adapted from [39])

Compression bounded magnets usually use as matrix material a thermoset epoxy. The compound flows into a press cavity and compact it under high pressure. Afterwards, the compacted magnet is cured at temperatures of around 160 °C. An advantage is the possibility of a high filler fraction of about 80 %. Compression offers a near-net-shape fabrication. This makes a post-processing step generally unnecessary.

Injection molding (IM) is the most important mass manufacturing process. The heated compound is pressed under high pressure into cavities where it cools down. After the object is hardened, the mold cavity is opened and the object will be ejected. IM is a highly efficient process, it allows the production of bounded magnets with a filler fraction of up to 70 %. The formed objects have precise dimensions and the usage of anisotropic powder is state-of-the-art.

Extrusion uses the same technique as for the compound production process. It squeezes the melted compound through a die (orifice) where it cools down. Rigid or flexible compounds with a magnetic loading of about 75 % are possible. Due to the high

abrasive magnetic particles, one challenge for manufactures is to develop tools that are resistant to wear.

Calendering forms the hot plastified compound between rollers to a continuous strip with a typical thickness between 0.25 and 6 mm. Due to the usage of elastomer binders, highly flexible magnets with a filling fraction of around 70 % can be fabricated.

2.4 Additive Manufacturing of Magnets

This section give a short overview of the current status of other research projects in the field of additive manufacturing of soft and hard magnetic materials. The first project is a derivate of the photopolymer jetting. Instead of an ink-jet printer head that generate jets of the UV curable liquid resin, a paste of low-viscosity curable polymer with magnetic powder is used to create the layers of an object [73]. Additionally, a paste of electrically conductive silver can generate conductive paths such as windings for a transformer. A commercial FDM 3D printer is modified to deposit the paste onto the printer table. After the structure is printed, it is cured at 250 °C for a hour without any external pressure to form a layer of the magnetic component. The electrical resistivity of the printed winding is about three times higher than that of bulk silver. The main disadvantage of this method is the high curing temperature and curing time to print one layer. On the other side, full-integrated electrical components like a transformer core can be print in one step.

Soft magnetic materials can be in-situ synthesized by selective laser melting (SLM). Typically, permalloys like FeNi₃ or Ni-Fe-V and Ni-Fe-Mo, respectively are used [74] [75]. A big advantage of this method is to manufacture dense soft magnetic objects with an arbitrary shape. While the saturation magnetization of these alloys is comparable to conventionally processed versions of similar composition, the coercivities were higher for the laser-processed alloys, presumably due to microstructural defects. The magnetic properties can be modified by the processing laser parameters, that can be used to produce tailored soft magnets for various applications like transformers, electric motors, inductive, and other electromagnetic devices.

Compared to dense magnets produced by SLM, FDM of compounds with soft magnetic particles are investigated [76]. Samples of commercially available extruded com-

posite filament from Proto-Pasta (Magnetic Iron PLA) are printed. This filament consists of 40 wt.% Fe particles embedded in a polylactic acid (PLA) polymer matrix. As discussed in section 2.3.3, the magnetic properties of soft magnetic compounds are mainly influenced by their filler fraction. Filling fraction of more than 65 vol.% would be necessary to fabricate functional soft magnetic parts.

The next project uses SLM and commercial spherical NdFeB powder (MQP-S supplied by Magnequench Corporation) to create permanent magnetic structures [77]. The produced structures have a density that is 92 % of the ideal one. Therefore, it outperforms polymer-bonded magnets regarding of the maximum energy product and the temperature stability. The difficulties of this procedure is to find the optimal process parameters. Due to the complex phase diagram of NdFeB, the liquefaction and the subsequent cooling down of the melt influences the size and the composition of the grains [78].

Another suitable technology for the additive manufacturing of magnets is binder jetting (BJ) [79]. A resin-coated isotropic NdFeB magnetic powder (referred to as MQP from Magnequench Corporation) is used for this study. After printing, the structures are cured in an oven by a temperature of 150 °C for 4 – 6 h. Disadvantages of this method is the porous and rough surface, as well as only densities up to 46 % compared to a full-dense part can be archived. This leads to minor magnetic performance compared to magnets manufactured by other AM techniques. One possibility to enhance the coercivity of the BJ printed magnets is by alloy infiltration [80]. Low-melting point eutectic alloys (i.e. NdCuCo, PrCuCo) can be used to infiltrate a structure and double the coercivity.

To 3D print polymer-bonded magnets by the aim of a FDM process with a big size, the big area additive manufacturing (BAAM) technology can process NdFeB powder (MQP-B+ supplied by Magnequench Corporation) with a filling fraction of 65 vol.% [81]. The build volume of the system is $3.56 \times 1.65 \times 0.86 \text{ m}^3$ (L×W×H), this is greater as for the most other systems. Due to the big size of the BAAM system, a single screw extruder is directly mounted on the printer head. Therefore, no prefabricated filaments are necessary. However, this leads to a limitation of miniaturization of feasible structures.

Experimental Setup

3

Portions of this chapter were previously published in [82] and have been reproduced with permissions of the coauthors and in accordance with the publisher's policy. Content which was not generated by the author of this thesis is explicitly denoted, copyright is held by American Institute of Physics.

3.1 3D Printer

This section describes the 3D printer for the manufacturing of the polymer-bonded magnets. As described below, a commercial 3D printer is used without any modifications. To get well printing results, it is important to optimize the printing parameters. A general overview of these printer parameters is given.

3.1.1 Main Features of the 3D Printer

For the printing process, the conventional end-user 3D printer Builder from Code P is chosen. This printer works by use of the FDM principle. It has a maximum building size of $220 \times 210 \times 164 \text{ mm}^3$ (L×W×H). Structures with a layer height resolution between 0.05 and 0.3 mm can be printed. The stepper motors have a resolution in x and y -axis of 0.1 mm. The printing speed ranges from 10 to 80 mm/s, and the traveling speed ranges from 10 to 200 mm/s. To print the highly filled compound the nozzle has a diameter of 0.4 mm, and by the means of a dual feed extruder, two different filaments can be mixed in a contentions ratio, or defined regions of the printing object can be printed with different materials. If two different filaments are mixed together, only filaments made of the same plastic can be processed. This means for a compound, that the matrix material must be the same. Otherwise, the two different materials cannot bind together. The filaments must have a diameter of $1.75 \pm 0.2 \text{ mm}$, to avoid sticking of the filament

in the printer head. The maximum nozzle temperature is 260 °C. For a better adhesion of the printing object, the printer bed can be heated up to 80 °C. Figure 3.1(a) shows a picture of the printer, (b) shows a sketch of the mixing extruder.

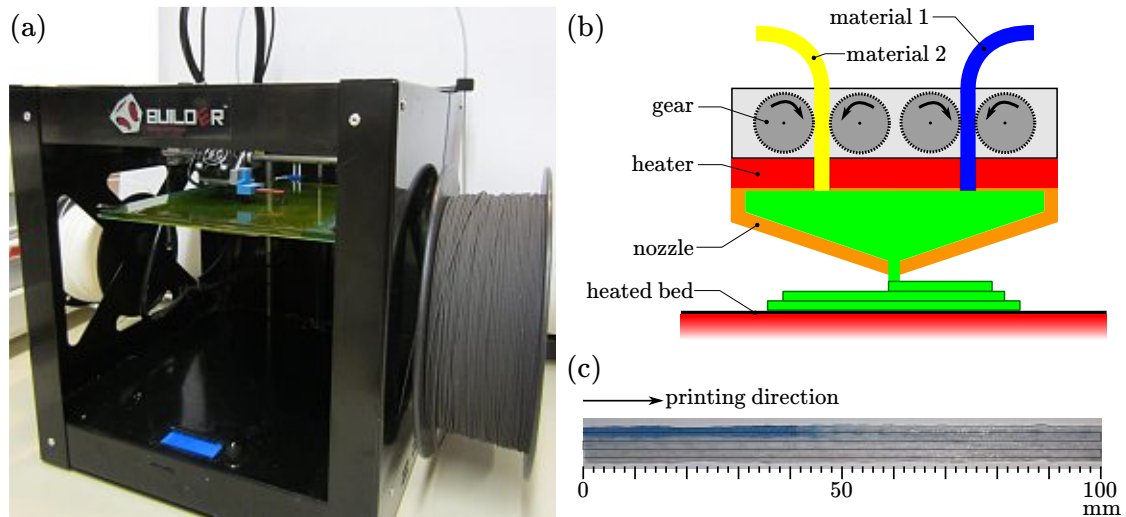


Figure 3.1: 3D printer Builder from Code P with its mixing extruder. (a) Picture of the 3D printer. (b) Sketch of the mixing extruder. (c) Picture of the printed test pattern to estimate the minimum switching volume.

The Builder 3D printer is a variant of the open source RepRap 3D printer [23]. This means that the syntax to control the printer movements are well documented, what is a big benefit for our usage. The commands for the printer are send via a serial interface. The syntax of the code is based on the G-code (also known as RS-274), what is the common name for the most widely used numerical control (NC) programming language. All RepRap printers follow the NIST RS274NGC G-code standard [83]. An example of such a G-code syntax to control the 3D printer functions is listed in listing 3.1.

Listing 3.1: Example of the G-code syntax for a RepRap 3D printer.

```
G90                ; use absolute coordinates
M104 S260          ; set extruder temperature to 260 °C
G28                ; home all axes
G1 Z5 F5000        ; lift nozzle to 5 mm, feedrate 5000 mm/minute
M109 S260          ; wait for temperature to be reached
G0 F1500           ; Set the feedrate to 1500 mm/minute
G1 X10 Y20 Z30 E10 ; move to 10/20/30 mm (X/Y/Z) while extruding 10 mm of material
M104 S0            ; turn off temperature
M84                ; disable motors
```

An important attribute of the mixing extruder is how fast the extruder can switch between two different materials. To estimate the minimum switching volume, a meander like test pattern is programmed with G-code commands and printed with the parameters as listed in table 3.1. The test starts by extruding material 1 (PLA, blue) until only blue material comes out of the nozzle. Then, the extruder is switched to extruder 2 (PLA, white) and the printer starts to print the test pattern. After a characteristic printing distance, the color changes. This length determines, with the nozzle diameter and layer thickness, the minimum switching volume. Figure 3.1(c) shows a picture of the printed test structure. After a length of around 45 mm the color changes from blue to white, but spoors of blue color are visible until 100 mm. However, this is only a rough estimation of the switching volume, a printing length of 50 mm, a layer height of 0.25 mm and a track width of 1 mm are assumed. This leads to a minimum switching volume of 12.5 mm^3 . This means that during the printing process only structures with this minimum switching volume can be printed with the desired material or mixing ratio. To reduce this volume, a wipe and prime tower can be printed [84]. Before the material or mixing ratio is changed, a tower nearby the object is printed to fill the nozzle with the new composition.

Theoretically, it would be possible to print any objects by directly writing the G-codes for the extruder movements in a file, but this would be a really inefficient way to print complex structures. A more comfortable way to transform a CAD file, mostly a STL file into G-code is a slicer program.

3.1.2 Slicer

As mentioned in section 2.1, to 3D print an object, the STL file must be sliced into layers. Two different slicing techniques are relevant, the direct and the adaptive slicing. The direct method slices the object into layers with the same thickness. This leads to the staircase effect, and therefore, to a rough surfaces and incorrect dimensions (figure 2.8). To minimize this effect, the adaptive slicing algorithm was developed. Each layer has a individual thickness h between a minimum and maximum ($h_{\min} \leq h \leq h_{\max}$). The thickness of each sliced layer is mainly determined by the curvature of the surface [85].

After slicing of the object, the tool path for the extruder movements must be defined. Several types of tool path strategies and algorithms such as zigzag, contour, spiral and

partition patterns have been developed with different considerations of the build time, cost, surface quality, strength and stiffness of AM objects [86]. Figure 3.2 shows the steps from a STL file to G-code for the 3D printer.

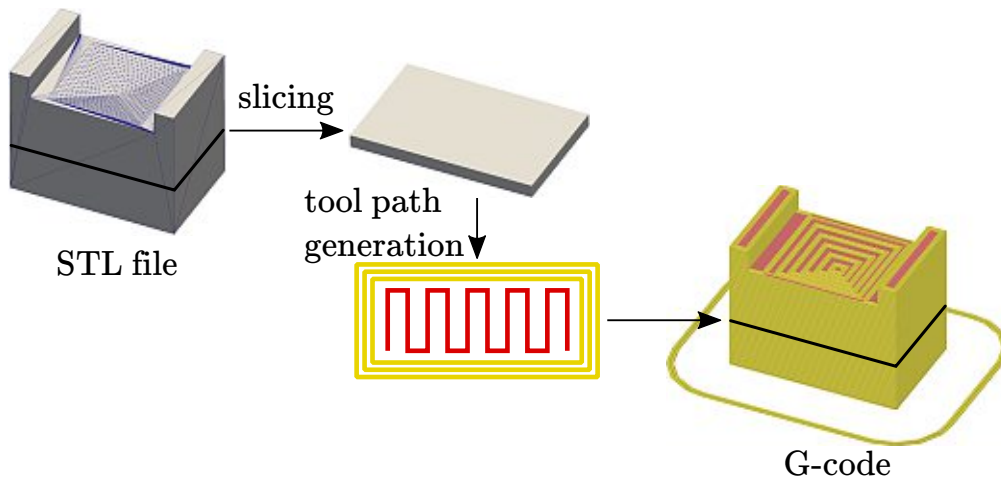


Figure 3.2: Tool-chain for slicing of a STL file. The object is sliced into layers with a specific height. For each layer, the tool path of the extruder is calculated (perimeters: yellow, infill: red). The tool paths of all layers are converted into G-code.

Nowadays, many different slicing and tool path generation programs exist. One of the most effective and efficient programs is the open source Slic3r (v.1.3.0) software. It generates the G-code directly from a STL file, as well as manual printer control functions exist. Many different variables can be modified to optimize the printing result for a given material.

3.1.3 Printer Parameters

To get quality prints, many different slicer settings are available for optimization, as well as the mechanical processes needs to be calibrated. The following list gives a brief overview of the most important FDM 3D printer settings. Attention should be paid that the material selection influences the settings and thus the printing result.

Printing bed preparation: the printing bed can be heated to increase the adhesion between the bed surface and the print. Bed leveling is necessary to calibrate the gap between the nozzle and the bed across the entire bed surface. Depending of the printing material, a coating of the bed surface enhances the adhesion.

Temperature: If the extrusion temperature is too low, the layers have difficulties to stick together. Too high temperatures lead to undesirable artifacts. The optimal temperature is highly depended of the material.

Speed: the print speed defines the overall printing time. A short printing time is desired, but if the speed is too high, it might be the case that the extruder will lay down next layer although the previous layer had not managed to cool down. This will cause unnecessary bends, cavities and other defects of the detail. Too high printing speed can also result in messy and inaccurate look of the print.

Layer thickness: prints with thinner layers create more detailed prints but the printing time increase significantly. A special problem of highly filled compound filaments is that the layer height must be greater than the particles size of the infill.

Infill: infill refers to the density of the space inside the outer shell of an object. For the most 3D printing applications, it is advantage to set the infill as low as possible. It reduces the printing time and the mass of the print. In our case, the fill density correlate with the magnetic properties of a print. Therefore, the infill should be as a high as possible.

All settings depend on the used 3D printer, material selection, and the structure of the print. This means that all settings must be adjusted individually on the specific requirements. The optimal printing setting for our setup and our filaments (the materials are described in chapter 4) are listed in table 3.1.

3.2 3D Magnetic Field Scanner

3.2.1 Introduction

To characterize the quality of the magnetic field of the printed magnets, a magnetic field mapping system is required. This is a crucial part of this thesis, because without the knowledge of the field distribution, no statement about the effectives of the 3D printing process of polymer-bonded magnets can be given. For a full characterization of a magnet, all three components of the magnetic flux density $\mathbf{B}(\mathbf{r})$ at the position $\mathbf{r} \in \mathbb{R}^3$ must be measured. Commercial available 3D field mappers with a 3-axis Hall probe and a probe positioning accuracy of 0.1 mm cost around \$ 20,000 (M3D-2A-PORT from

Table 3.1: Best empirically found printer parameters for the different used materials.

parameter	material		
	PLA	PA12	PCL
extruder temp. (°C)	220	260	100
layer height (mm)	0.1	0.1 – 0.15	0.15
printer speed (mm/s)	25	20	23
fill density (%)	30 – 80	30 – 100	20 – 100
fill pattern	rectilinear	rectilinear	rectilinear
bed adhesion	Kapton + PLA juice	tape	tape
bed temp. (°C)	60	60	–

	material		
	Neofer® 25/60p	PA12+NdFeB	PCL+NdFeB
	255	260	100
	0.1	0.15	0.2
	20	20	23
	100	100	100
	rectilinear, contour	rectilinear, contour	rectilinear, contour
	solvent free	layer of Polyvinyl	tape
	Pritt glue stick	acetate (PVA)	
	40	60	–

Senis), and the price goes to \$ 80,000 for a high end system with a magnetic field resolution of $< 10 \mu\text{T}$ and a probe positioning accuracy of $2 \mu\text{m}$ (MMS-1A-RS from Sensis). These kind of commercial systems are not affordable for this project. This comes to the idea to use the 3D axis capability of our 3D printer to measure the field distribution. A 3D magnetic field probe which measures all field components \mathbf{B} simultaneously is attached on the printer extruder. A script that uses G-code commands to move the extruder in a specific measurement volume, area or line controls the printer. An advanced measurement software is developed that reads the STL file of an object and calculates the minimum distance between object and sensor. This is useful to measure the field distribution of complicated structures. An accurate calibration of the sensor is a crucial step to get reasonable measurement results. To skip this elaborate adjustment of the sensor, a method is developed that easily calculates the calibration parameters from the deviation between measurement and simulation results.

3.2.2 Sensor Characteristics and Data Processing

There is a huge variety of magnetic sensors for a wide range of applications [87]. The majority of these applications use the magnetic field to detect other informations such as position, angle, speed, and informations with a reading head for hard disks. In our case, a sensor is required that provides the components of the magnetic flux density vector. The sensing principle is not important, but the following requirements must be fulfilled: (i) measurement range from 10 μT to at least 100 mT, (ii) the sensor has a linear output without hysteresis effects, (iii) adequate detectivity. This requirements leads to Hall effect sensors.

A Hall effect sensor is a transducer that changes the output voltage as a function of an external magnetic field. These kind of sensors use the Hall effect, it describes a voltage difference across an electrical conductor if a current is applied along it and a magnetic field acts perpendicular on the conductor [88]. To measure all three components of the magnetic field density $\mathbf{B}(\mathbf{r})$ of one point \mathbf{r} at the same time, a 3D sensor is necessary. Such a 3D Hall sensor consists of a centered Hall sensor to measure the perpendicular field, and at least four vertical Hall plates to measure the in-plane field components. The average of each in-plane component is calculated, this is a good approximation of the corresponding component in the center [89].

Investigations of commercial available Hall sensors lead to the suitable 3D Hall transducer 3A-03L02F-A.2T2K5J from Sensis, but a price of more than \$ 6,000 for the equipment explodes the budget of this project. Nevertheless, the new available 3D Hall sensor TLV493D-A1B6 from Infineon fits perfectly for our purpose. It has a price of under \$ 2, a usable magnetic linear range of all three axis of ± 130 mT, and a digital output via 2-wire standard inter-integrated circuit (I²C) interface. A Genuino 101 microcontroller is programmed to read out the components of \mathbf{B} via I²C with a frequency of 3.3 kHz and sends it to a personal computer (PC) by the serial interface. The bottleneck of the data transmission between Hall transducer and the PC is the Genuino microcontroller. It restricts the sampling frequency to 0.5 kHz. By the aim of a specific data acquisition (DAQ) hardware, the sampling frequency could be increased significantly, but for measurements of static magnetic fields, the sampling frequency is only important to reduce the measurement time.

The analog-to-digital converter (ADC) of the TLV493D transducer has a resolution

of 12 bits, and a maximum field range of ± 200 mT. This leads to a field resolution of $400/2^{12} = 97 \mu\text{T}$. In practice, the useful resolution of a converter is limited by the best signal-to-noise ratio (SNR) that can be achieved for a digitized signal. The SNR is defined as

$$SNR = \frac{P_{\text{signal}}}{P_{\text{noise}}} \quad (3.1)$$

with the power of the signal P_{signal} and the noise power P_{noise} , respectively. The noise power is the measured total noise in a given bandwidth of the Hall transducer when the signal is not present. Several types of noise such as thermal noise, shot noise, $1/f$ noise superimpose each other. The power of thermal noise and shot noise is constant over the frequency, $1/f$ noise is mainly significant at lower frequencies. The minimum signal that can be detected of a measurement system has a $SNR = 1$. If white noise is the main noise part (independent of frequency) the SNR can be enhanced by averaging of the measurement data. Figure 3.3(a) shows a noisy static signal $s(f_{\text{signal}} = 0 \text{ Hz})$ with different averages n . The new averaged signal \bar{s} has a better SNR but a lower sampling rate $\bar{f} = f/n$.

In order to compare various sensor systems to measure the magnetic flux density B , the detectivity D ($SNR = 1$) is introduced. It sets the sensitivity of the transduced voltage signal dV/dB into the relation of the noise power P_{noise} and the sampling frequency f [90]. For static field measurements ($f_{\text{signal}} = 0 \text{ Hz}$) and a linear transfer function of the sensor, the lowest detectable field is:

$$\delta B = D \sqrt{\frac{f}{n}} = D \sqrt{\bar{f}}. \quad (3.2)$$

The lowest detectable field is equal to the standard deviation δB of the averaged signal with the sampling rate $\bar{f} = f/n$. Figure 3.3(b) shows δB of the Infineon 3D Hall transducer as a function of n , as well as a fit of equation 3.2 to verify the $\delta B \sim 1/\sqrt{n}$ correlation of the transducer. Table 3.2 lists the calculated detectivity D_i for all three Hall transducers of our setup.

3.2.3 Upgrade 3D Printer

A traditional calibration of the sensor position, angles of the 3D Hall sensor would lead to a complex mounting and adjusting system. In this work, a different approach is

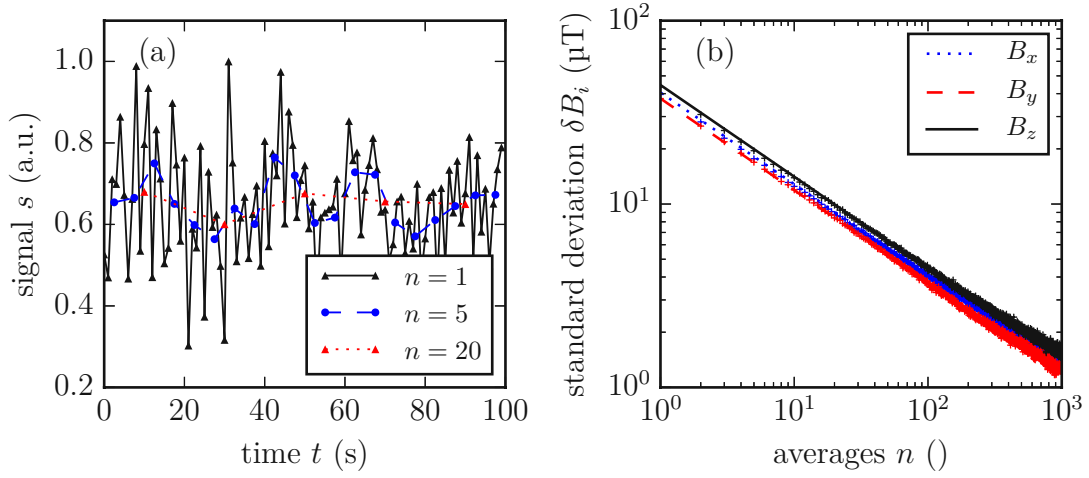


Figure 3.3: Noise signal and the detectivity measurement. (a) Noise signal with different averages n . (b) Measurement of the standard deviation δB of the used 3D Hall transducer and a fit of the relation $\delta B \sim 1/\sqrt{n}$.

Table 3.2: Detectivity measurement for the 3D Hall transducer scanner for static magnetic fields for all three direction in space.

direction	detectivity $D_i(f_{\text{signal}} = 0 \text{ Hz})$ ($\mu\text{T}/\sqrt{\text{Hz}}$)
x	2.65
y	2.43
z	2.10

taken. As described in section 3.2.5, a calibration routine based on stray field simulations is used to find the calibration parameters. This allows us to use a simple self 3D printed mounting jig as mounting system. Different sensor positions can be realized by several mounting jigs. In figure 3.4 three different jigs are pictured. This system allows the operator an easy and fast change between the different jigs, as well as a comfortable handling of sensor.

3.2.4 Measurement Software

Usually, the magnetic field distribution around, or near to the surface of a magnetic object is demanded. To avoid damages and crashes between object and sensor, an intelligent measurement software is required. Some measurement frameworks use a optical distance measurement system to detect the shape of the device under test (DUT) [91]. As this would lead to a complex setup, another path is taken. To 3D print a structure,

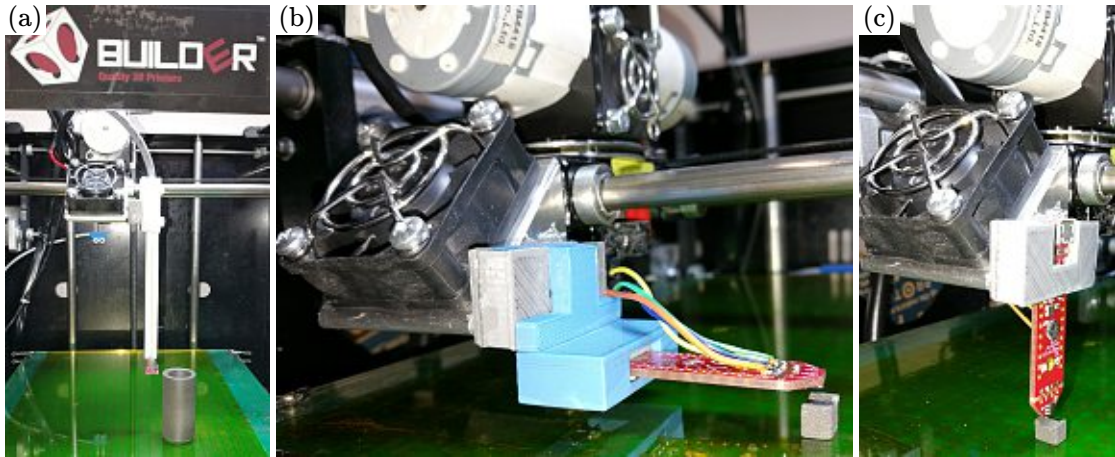


Figure 3.4: Different sensor mounting capabilities on the printer extruder. (a) Long thin rod with the sensor on the bottom. (b) Horizontal mounting. (c) Vertical mounting.

a STL file of the object is necessary to generate the G-code. This file can be used as input to define the measuring space in \mathbb{R}^3 . The STL format describes the surface of 3D bodies by means of triangular facets (tessellation). Each triangle facet is characterized by the three corner points (p_1, p_2, p_3) and the corresponding surface normal n of the triangle. The triangles use a three-dimensional Cartesian coordinate system. A grid of measurement points $P'_{ij}(x, y)$ with a specific resolution dr is span over the xy -plane. An algorithm that finds all points inside a given triangle is necessary. A simple method uses Barycentric coordinates of the triangles [92].

At the beginning, the triangle $T \in \mathbb{R}^3$ is projected on the xy -plane ($T' \in \mathbb{R}^2$). Figure 3.5(a) shows a sketch of the method. The triangle T' is defined by the three vertices p'_1, p'_2 and p'_3 . Each point P' located inside this triangle can be written as a unique convex combination of the three vertices (figure 3.5(b)).

$$P' = \lambda_1 p'_1 + \lambda_2 p'_2 + \lambda_3 p'_3 \quad (3.3)$$

The triple λ is then called barycentric coordinates of the triangle, with the condition $\sum_{i=1}^3 \lambda_i = 1$. To solve the conversion from Cartesian to barycentric coordinates, it can be rewritten as matrix form so that

$$R\lambda = P' \quad (3.4)$$

with $R = (p'_1 | p'_2 | p'_3)$ and $\lambda = (\lambda_1, \lambda_2, \lambda_3)^T$. Then, the condition $\sum_{i=1}^3 \lambda_i = 1$ and the

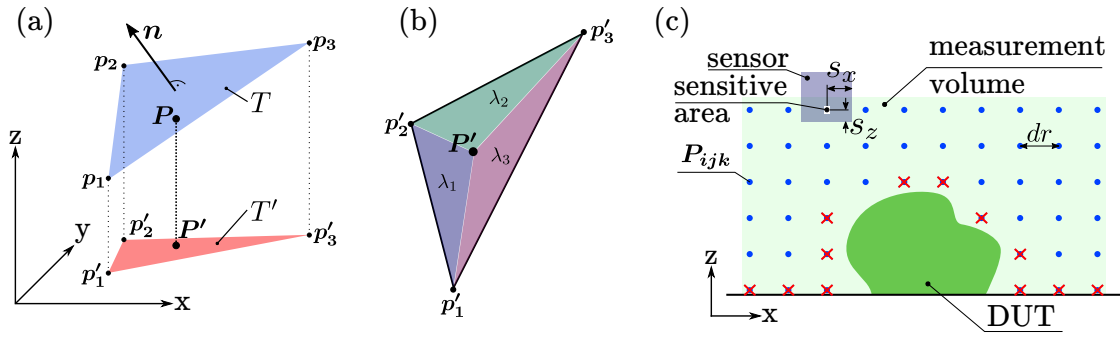


Figure 3.5: Principle of the software to define the measuring grid. (a) Projection of the triangle $T \in \mathbb{R}^3$ to $T' \in \mathbb{R}^2$ to test if the point P' is inside T' . Find the distance between P' and P by the usage of the Hesse normal form. (b) Barycentric coordinates $(\lambda_1, \lambda_2, \lambda_3)$ of a triangle. It can be seen as the area of the sub-triangles $p'_1 p'_2 P'$ (for λ_1), $p'_2 p'_3 P'$ (for λ_2), and $p'_1 p'_3 P'$ (for λ_3). (c) Extension of the measuring grid to \mathbb{R}^3 . Due to the sensor size, some points must be withdrawn to avoid crashes between sensor and the device under test (DUT) or building platform.

barycentric coordinates can be solved as the solution of the linear system

$$\begin{pmatrix} p_{x'_1} & p_{x'_2} & p_{x'_3} \\ p_{y'_1} & p_{y'_2} & p_{y'_3} \\ 1 & 1 & 1 \end{pmatrix} \lambda = \begin{pmatrix} P'_x \\ P'_y \\ 1 \end{pmatrix} \quad (3.5)$$

P' lies in T' or on the edge or corner of the triangle if the linear system is solvable and if $0 \leq \lambda_i \leq 1 \forall i$ in $1, 2, 3$.

After all points P'_{ij} that lie inside a given triangle are found. The z -component of each point must be calculated. The Hessian normal form

$$\mathbf{n} \cdot (\mathbf{P} - \mathbf{p}_i) = 0, \quad (3.6)$$

with the normal vector \mathbf{n} and a vertex \mathbf{p}_i , can be used to find the point $\mathbf{P}(x, y, z)$ on the plane T . This calculation provides the height information of the DUT for all points of the measuring grid.

To measure the magnetic flux density \mathbf{B} in a specific volume around the magnet, the measuring grid with the points $\mathbf{P}_{ij}(x, y, z) \in \mathbb{R}^3$ and a resolution dr must be extended in all three directions in space. To avoid crashes between sensor and object or building platform, the size of the sensor must be considered. The sensitive area of the sensor is inside the casing of the sensor. In our case, the sensitive area for the x and y -direction is in the middle of the sensor with a size of $s_x = 10$ mm and $s_y = 2$ mm. This finite sensor

size makes it necessary to withdraw some points of the measuring grid to avoid crashes. Figure 3.5(c) shows the principle of the expansion of the grid with the measuring points $P_{ijk}(x, y, z) \in \mathbb{R}^3$, and the withdrawn points due to the sensor size. An example of a DUT with a complex shape is shown in figure 3.6(a). Not only the resolution dr between

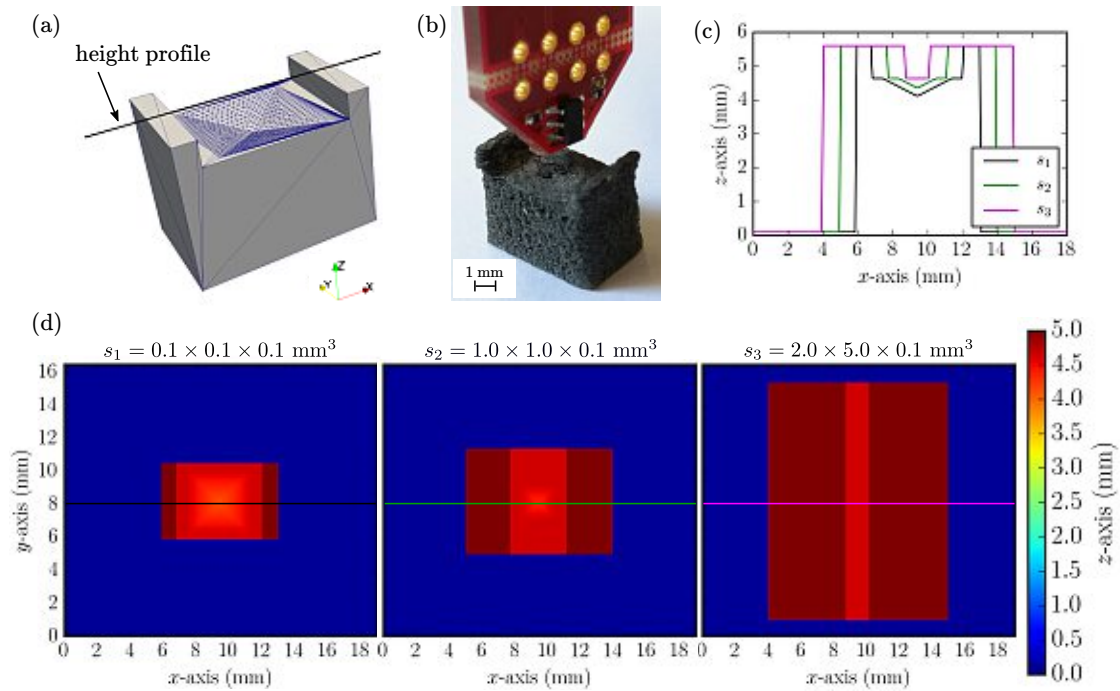


Figure 3.6: Height profile of a complex structure for the 3D magnetic field mapping system. (a) STL file of the object. A line scan along the x -axis ($y = 0$) is marked. (b) Picture of the finite sensor size above the printed magnet. (c) Line scans along the x -axis ($y = 0$) with different sensor sizes ($s_1 = 0.1 \times 0.1 \times 0.1 \text{ mm}^3$, $s_2 = 1 \times 1 \times 0.1 \text{ mm}^3$, $s_3 = 2 \times 5 \times 0.1 \text{ mm}^3$) and a resolution of 0.1 mm. (d) Height profiles in the xy -plane around the object with different sensor sizes and a resolution $dr = 0.1 \text{ mm}$.

the measurement points affects the quality of the measurement. The sensor size s has a big influence on the field measurement of small structures. Figure 3.6(b) shows the sensor above a DUT. The influence of the sensor size s is illustrated in figure 3.6(c-d). If the sensor size s is too large, a scan inside the cavity is no longer possible.

The algorithm to find the points $P_{ijk}(x, y, z) \in \mathbb{R}^3$ with a resolution dr inside the measuring volume is implemented in Python 2.7. The software creates the G-code for the extruder movement (G1 command) and sends it via the serial interface (USB) to the 3D printer. At each measurement point, n measurements are taken and the average

and standard deviation is calculated. The results are exported into a data file for a further post-processing step. ParaView can quickly build visualizations to analyze the data using qualitative and quantitative techniques. To interpolate the field between the points $P_{ijk}(x, y, z)$, the Delaunay triangulation algorithm of ParaView is used [93].

3.2.5 Calibration Routine

An advanced adjustment and alignment of the sensor is important for the accuracy of the stray field measurement. The idea is to avoid an exact positioning and alignment of the sensor, because this would lead to a complex sensor mounting system. A calibration method relying on detailed stray field simulations is proposed.

The calculated magnetic flux density B of a predefined object (e.g. cylinder magnet) is used to calibrate the sensor. The main idea of the calibration is to use an inhomogeneous reference field, which relates to the geometry of the calibration sample and its stray field. The field mapping system scans the magnetic field in a defined volume outside the calibration magnet. With the numerical solution B_s and the measured field B_{exp} , an optimization problem can be formulated, where the squared error between the calculated and measured values is minimized, in order to determine the calibration parameters. A reference field of a calibration magnet can be simulated with the finite element (FEM) stray field simulation framework as described in section 5.2.

Figure 3.7(a) shows a sketch of a calibration setup. The calibration jig has a cavity on a defined position for a rough calibration of the sensor offset. The step on the corner guarantees an exact positioning of the DUT. A picture of the setup with the 3D Hall transducer in the horizontal mounting jig and the calibration magnet is pictured in figure 3.7(b). The cylindrical calibration magnet has a diameter of 10 mm and a height of 5 mm. It has the grade N35, this number represents the $(BH)_{\text{max}}$ in Mega-Gauss Oersteds (MGOe) where 1 MGOe (cgs units) equals 7.96 kJ/m^3 (SI units). This leads to a remanence for a N35 magnet of $B_r = 1.21 \text{ T}$.

The simulated field B_{sim} in relation to the calibration parameters $s, \gamma, \beta, \alpha, \Delta r$ is defined as

$$B_{\text{sim}} = s \mathbf{R}_{ZYX}(\gamma, \beta, \alpha) B_s(\mathbf{r} - \Delta \mathbf{r}) \quad (3.7)$$

where s is the sensitivity of the 3D Hall sensor, \mathbf{R}_{ZYX} is the rotation matrix with the

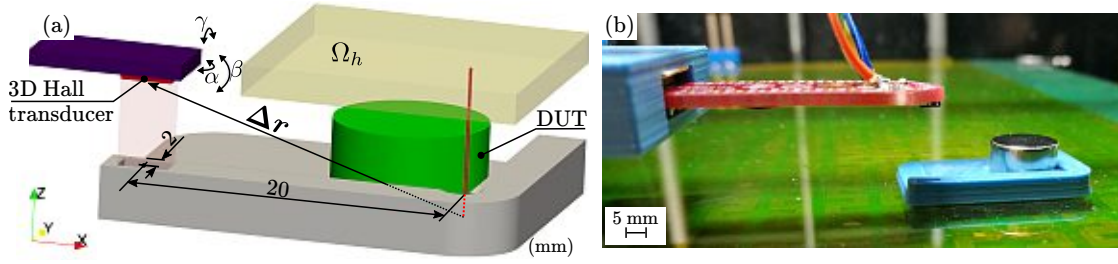


Figure 3.7: Sketch and picture of the calibration procedure. (a) Sketch of the calibration jig with a device under test (DUT) and the 3D Hall transducer. The measurement volume Ω_h above the cylinder magnet is $20 \times 20 \times 2 \text{ mm}^3$ ($L \times W \times H$). For a rough calibration of $\Delta \mathbf{r}$, a small cavity is in the jig. (b) Picture of the 3D Hall transducer with the horizontal mounting jig and the calibration setup.

Euler angles (γ, β, α) (equation A.1) to compensate the tilting of the sensor, and $\Delta \mathbf{r}$ is the sensor offset.

Solving the following minimization problem results in the unknown parameters of the calibration

$$\min_{s, \gamma, \beta, \alpha, \Delta \mathbf{r}} \|\mathbf{B}_{\text{exp}} - \mathbf{B}_{\text{sim}}\|^2. \quad (3.8)$$

Powell's conjugate direction method is used to find a local minimum of the function [94]. For this algorithm, the function need not be differentiable, and no derivatives are taken. The calibration algorithm is implemented in Python 2.7 and Scipy 0.18. For a fast computation of the minimization problem, the fields \mathbf{B}_{sim} and \mathbf{B}_{exp} are converted into a visualization toolkit (VTK) file. VTK is an open-source software system for 3D computer graphics, image processing and visualization. It has a Python interface and it allows advanced modeling techniques such as interpolation of vector fields in the space (\mathbb{R}^3). This package allows a fast calculation of the field $\mathbf{B}_s(\mathbf{r} - \Delta \mathbf{r})$ for a sensor offset. Table 3.3 lists typical calibration parameters of our setup.

Table 3.3: Typical calibration parameters for the 3D field mapping setup.

Parameter	Value
\mathbf{s} ()	0.97/0.95/0.76
γ, β, α (°)	1.9/0.9/2.3
$\Delta \mathbf{r}$ (mm)	0.427/0.010/ - 0.108

Figure 3.8(a) indicates a significant difference between simulation and measurement of a cylinder magnet ($d = 15 \text{ mm}$, $l = 8 \text{ mm}$). After applying the calibration procedure

(figure 3.8(b)), the measurement fits very well with the simulation after the calibration method. The Infineon TLV493D-A1B6 3D Hall sensor has a X/Y to Z sensitivity deviation of approximately 20 %.

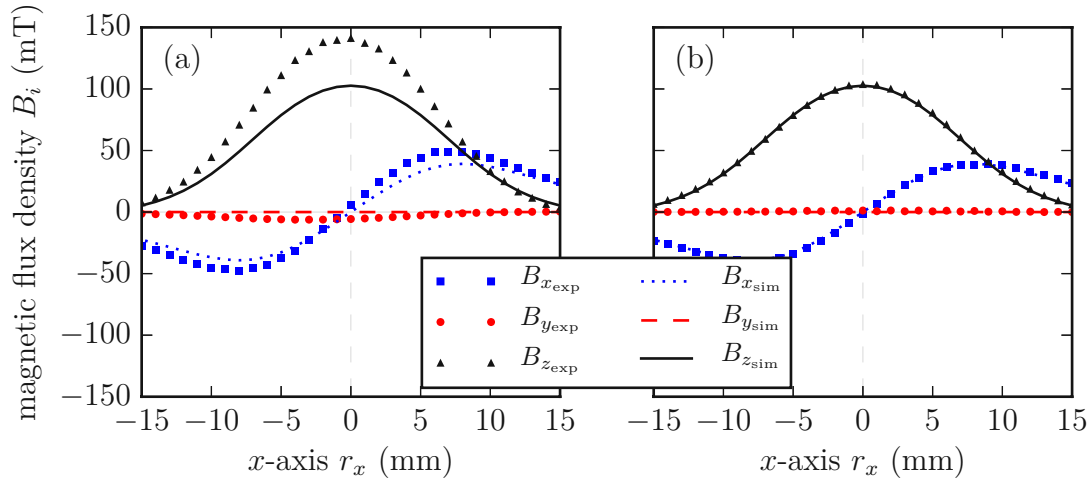


Figure 3.8: Magnetic flux measurement before and after calibration. (a) Line scan ($y = 0$, $z = 16$ mm) of \mathbf{B}_{exp} above the cylinder magnet ($d = 15$, $l = 8$ mm) without calibration, and the simulation \mathbf{B}_{sim} at the same line. (b) Measurement data in comparison with the simulation after calibration.

3.2.6 Benchmark Measurement

To benchmark the 3D magnetic field mapping system, a cylindrical magnet with unknown magnetization is measured at the magnetic testing laboratory at Infineon Technologies Austria AG and with our system. The setup at Infineon consist of a XYZ-table with a resolution of $0.1 \mu\text{m}$ and an absolute accuracy of $\pm 2 \mu\text{m}$. . An optical probe measures the size and the positioning of the DUT. The 3D magnetic field transducer is a 3D Hall probe (T-H3A, Sensis GmbH) with a accuracy of 0.1 % [91].

The cylindrical magnet has a diameter of 3 mm and it is 3 mm height. No informations about the material or magnetization distribution are provided. After the calibration routine as described above, a area scan 1 mm above the magnet with a resolution of 0.1 mm is performed (figure 3.9).

Infineon measured the field distribution of the same magnet and distance with a resolution of 0.5 mm. Figure 3.10(a) shows a line scan along the x -axis, 1 mm above the

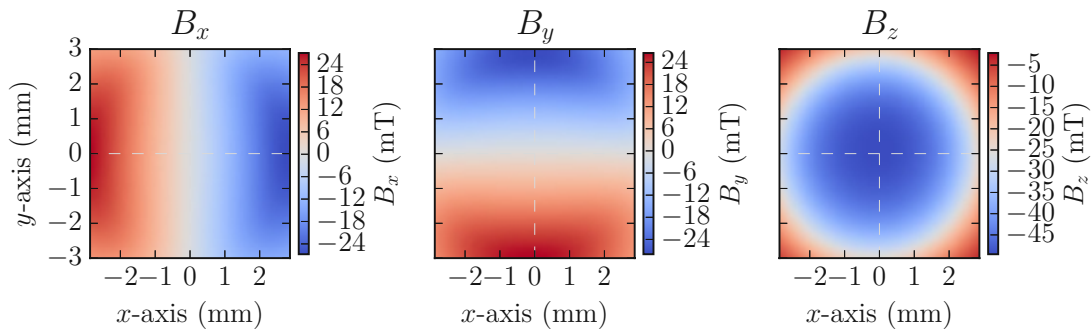


Figure 3.9: Area scan of the magnetic flux density B , 1 mm above the cylinder magnet.

magnet for both field measuring setups. As seen in figure 3.10(b) and figure 3.11, the absolute error ΔB between these two setups is lower than 1 mT. This benchmark test proves the effectiveness of the presented affordable field measurement setup.

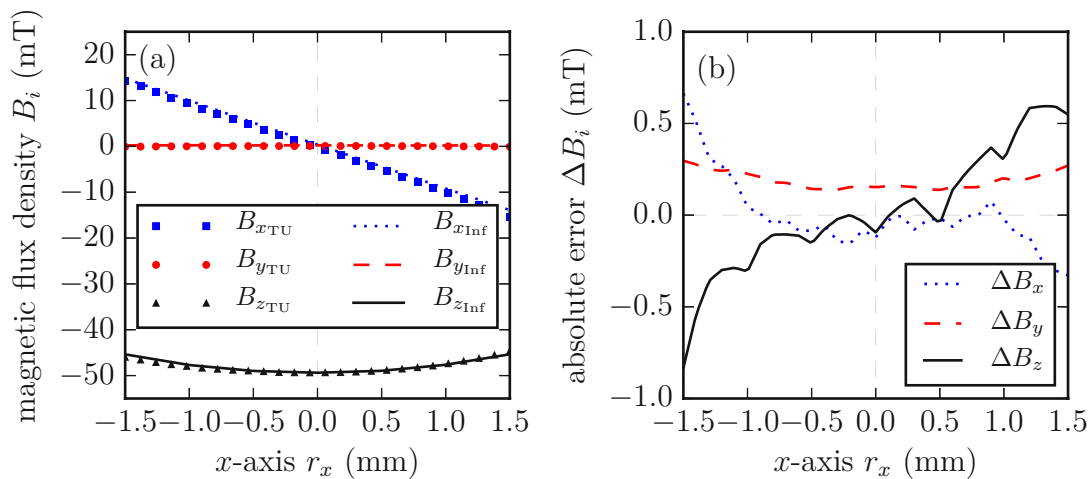


Figure 3.10: Comparison between the Infineon and the 3D printer field mapping system. (a) Line scan of B , along r_x , 1 mm above the cylinder magnet. (b) Absolute error ΔB between both systems.

3.3 “Maxel” Printer

An advantage of isotropic materials is the possibility to magnetize various regions of a magnetic structure into different directions, even if the magnet is already solid. This characteristic of the bonded magnetic materials can be used to upgrade the 3D printer to

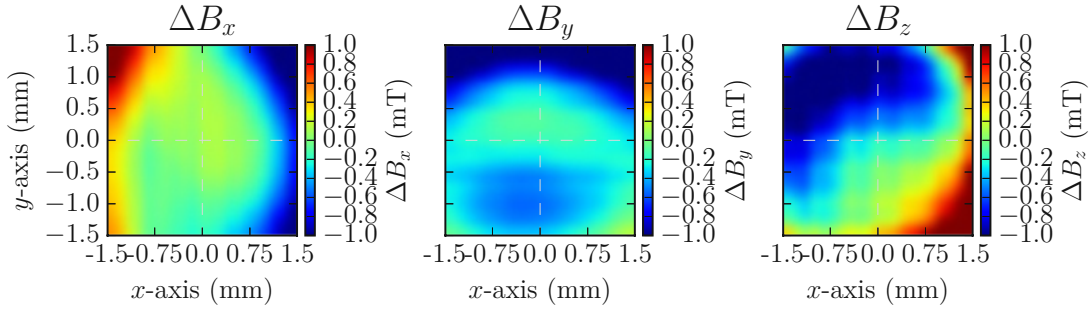


Figure 3.11: Area scan of the absolute error ΔB between the Infineon and the 3D printer field mapping system, 1 mm above the cylinder magnet.

a magnetic pixel (“maxel”) printer. A commercial available system exists that magnetize different regions of a magnet either along z or $-z$ -direction [95]. Undoubtedly, this system can only “print” such “maxels” on a already defined structure. This section describes the possibility and a procedure to print “maxels” not merely on the surface of a magnet, but rather on each layer of the 3D printed magnetic structure.

The commercial system uses a pulse coil to generate a magnetic field near to the saturation magnetization of a “maxel”. A pulse coil is a strong electromagnet that is powered by a brief pulse of electric current through its windings rather than a continuous current, producing a brief but strong pulse of magnetic field. Advantages of such a pulse coil compared to a coil with a continuous current through its windings are: (i) highest achievable magnetic fields, (ii) no or less cooling is required. On the other side are the disadvantages such as: (i) capacitor bank is required to generate a high current pulse, (ii) due to eddy currents and the inductance, only air coils with low windings are relevant. The Biot–Savart law gives a quick estimation of the required current I through the wire of a circular loop (figure 3.12(a)) [34]

$$\mathbf{B}(\mathbf{r}') = \frac{\mu_0}{4\pi} \int_C \frac{I d\mathbf{s} \times \mathbf{r}'}{|\mathbf{r}'|^3} \quad (3.9)$$

\mathbf{r}' is the distance between a point p at which the field is being computed and the wire element s . Carrying out the integration along the closed path C in cylinder coordinates, the z -component (center line) of the magnetic flux density is

$$B_z(z) = \frac{\mu_0 I r^2}{2(r^2 + z^2)^{3/2}} \quad (3.10)$$

with the radius r of the circular loop. A radius of $r = 0.25$ mm seems to be a good

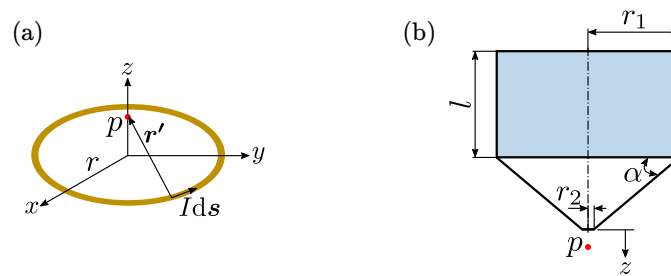


Figure 3.12: Concepts to realize a “maxel” printer. (a) Magnetic field due to a circular loop carrying a steady current. (b) Permanent cylinder magnet with a soft or permanent magnetic conical frustum.

compromise between size of the coil and spatial resolution of a “maxel”. The saturation magnetization of bonded magnet is around $B_s = 1$ T (section 4.5.3). This assumptions lead to a minimum current to reach B_s in the middle of the coil ($z = 0$ mm) of $I \approx 400$ A.

Due to the relative low saturation magnetization of bonded magnets, and the fact that a “maxel” printer with a pulse field coil would lead to a relative complex electronic setup, another technique should be discussed. Anisotropic sintered NdFeB magnets generate the strongest permanent magnetic fields. A conical structure can be used to concentrate the flux on the apex of the cone. Theoretically, the field diverges at the apex of a conical magnet [96]. In section 5.4, a calculation of the optimal cone angle of a such a magnet is presented. The fact that only conical frustums are practicably realizable, simulations based on the Comsol Multiphysics 5.2 FEM software of a structure as pictured in figure 3.12(b) are carried out.

The circumstance that NdFeB magnets are coated to prevent oxidations processes, it is difficult to shape a cone on a lathe. Therefore, another idea uses a NdFeB cylinder magnet with a soft magnetic conical frustum as a flux concentrator. For this reason, the ARMCO Pure Iron material with a minimum Fe content of 99.85 % and a saturation magnetization $B_s = 2.15$ T is used. A similar simulation as for the NdFeB frustum is carried out. Due to the nonlinear hysteresis behavior of the soft magnetic material, the Comsol simulation must solves the nonlinear Maxwell equations.

The Comsol simulations for the NdFeB and the Fe conical frustum are performed in 2D axisymmetric space. The upper cylinder magnet has a radius $r_1 = 5$ mm and a length of $l = 5$ mm, the conical frustum has a top radii of $r_2 = 0.25$ mm and a height of $h = \tan(\alpha)(r_2 - r_1)$. A parameter sweep of the angle α is performed to find the optimal

angle were the magnetic flux density B_z at $z = 0.1$ mm has a maximum (figure 3.13(a)). The optimal angle for the NdFeB and the Fe frustum is $\alpha_{\text{NdFeB}} = 35^\circ$ and $\alpha_{\text{Fe}} = 48^\circ$, respectively. Figure 3.13 shows the simulated B_z along the z -axis for the optimized cone angles α_{NdFeB} and α_{Fe} and the current loop with $I = 400$ A.

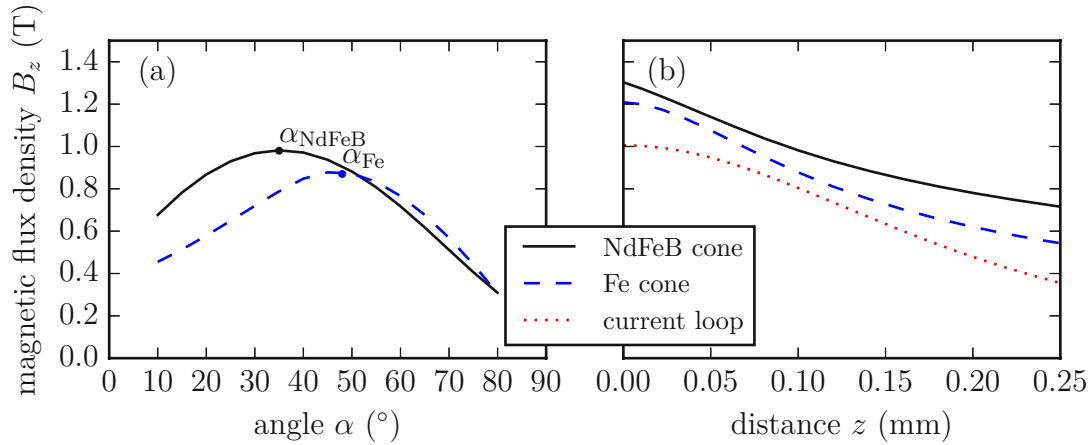


Figure 3.13: Simulations results for the “maxel” printer. (a) Parameter sweep to find the optimal cone angle α that maximize the magnetic flux density $B_z(z = 0.1$ mm). (b) Simulation of B_z along the z -axis for the optimized cone angles and the current loop with $I = 400$ A.

It is obvious that a pulse coil has the most advantages regarding flexibility, but the electronic setup would lead to a considerable additional effort and expense. The solutions with a permanent magnet and hard or soft magnetic conical frustum have similar field densities. Therefore, the “maxel” printer is realized with cylindrical permanent magnets (Grade N35, $B_r = 1.21$ T) and ARMCO Pure Iron frustums. Two of such contrary magnetized structures are fixed in a 3D printed jig. Figure-3.14(a) shows a picture of the 3D printer with the attached “maxel” printer. These two different orientated magnets have a gap of 50 mm to avoid mutual influences. To print a “maxel”, the cone moves to the desired position and touch the 3D printed object. The “maxel” printer has a spatial resolution of a “maxel” (a region where all particles aligned in the same direction) of around 0.5 mm. To print a pattern of different orientated “maxels”, a vector graphic software such as Inkscape can be used to draw the pattern. A Python script imports the graphic and convert it into G1 move commands for the 3D printer. Figure 3.14(b) shows a magnetic field scan (1.5 mm above surface) of the z -component of the magnetic flux above a 3D printed flat structure with different orientated “maxels”

on the surface. The “maxel” pattern shows the letters “TU”.

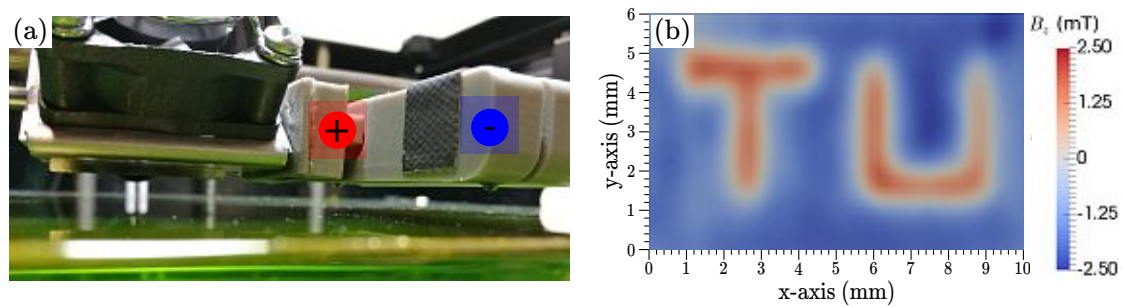


Figure 3.14: Upgrade of the 3D printer to a “maxel” printer. (a) 3D printed jig to hold the magnets (magnetized along z or $-z$ -direction) with the soft magnetic conical frustum. (b) Magnetic flux density B_z area scan (1.5 mm above surface) of a 3D printed magnet with an annotation of the surface.

It should be mentioned that each “maxel” is not full saturated during the “maxel” printing process. This results in a lower measurable magnetic field of the printed structure. However, this “maxel” printer shows a acceptable performance, as well this stage of expansion is just a pilot study to investigate the possibilities of such a “maxel” printer. It is conceivable that the 3D printer is upgraded to a full 3D pulse coil “maxel” printer in a further upgrade.

3.4 Magnetization

The 3D printed magnetically isotropic structures are magnetized inside an electromagnet. It is a self-built water-cooled electromagnet, and it is powered by a low-voltage power supply (Siemens NTN 35000-200). Maximum output current is 150 A with an operating voltage of 200 V. This setup has a maximum magnetic flux density inside the electromagnet of 1.9 T in permanent operation mode. The gap between the pole shoes is 50 mm.

4 Materials

Portions of this chapter were previously published in [82, 97, 98] and have been reproduced with permissions of the coauthors and in accordance with the publisher's policy. Content which was not generated by the author of this thesis is explicitly denoted, copyright is held by American Institute of Physics and Nature Publishing Group.

4.1 Introduction

The source material for FDM 3D printers is a thermoplastic feedstock in wire form. There are many different types of such filaments with different properties available, requiring appropriate printer parameters like temperature or printing speed. Commercial filaments are obtainable in the dimensions of 1.75 and 3 mm.

This chapter deals with the production of the polymer-bonded filaments for the 3D printing process. Several compounds are fabricated and extruded into suitable filaments. The advantages and disadvantages of the different filament diameters for highly filled compound materials are discussed. Several tests are performed to deduct the mechanical and magnetic properties of the compounds.

4.2 Source Materials

Up until now, no commercial filaments made of magnetic compound are available. This means that the filaments for this project must be produced by ourselves. It exists several magnetic compound formulations for the the manufacturing of polymer-bonded magnets by IM. Such feedstock materials can be used to extrude filaments by an extruder. On the other hand, by the aim a twin-screw mixing extruder as described in

section 2.3.6, the pure matrix plastic can be mixed with magnetic particles and extrude it into filaments at the same time.

4.2.1 Prefabricated Compound

Our partner Magnetfabrik Bonn GmbH, manufactures polymer-bonded permanent magnets in different forms and compositions. The Magnetfabrik has several different isotropic NdFeB compounds in their portfolio. Most of the compounds consist of a PA11 matrix; only one compound uses a PA12 as matrix material. For this project, two different isotropic compounds from the Magnetfabrik are chosen and extruded into filaments. Table 4.1 shows the characteristic properties of these compounds.

Table 4.1: Characteristic properties of the used isotropic compounds from the Magnetfabrik Bonn GmbH.

name	code after DIN 60404-8-1	$(BH)_{\max}$ (KJ/m ³)	B_r (mT)	H_c (A/m)	H_{cJ} (A/m)	ρ (g/cm ³)	composition
Neofer [®] 25/60p	REFeB 27/60p	27	400	260	630	4.35	NdFeB + PA11
Neofer [®] 65/70p	REFeB 64/60p	64	630	400	600	5.75	NdFeB + PA12

4.2.2 NdFeB Powder

The magnetic isotropic powder MQP-S-11-9 from Magnequench Corporation is used as magnetic filler for all filaments. This grade has a spherical morphology and it is suitable for the manufacture of bonded magnets, particularly by injection molding, extrusion and calendaring. It is based on a patented NdPrFeCoTiZrB alloy [99]. The NdFeB grains have a uniaxial magnetocrystalline anisotropy, and the orientation of the grains is random leading to isotropic magnetic properties of the bulk magnet. The powder is produced by employing an atomization process followed head treatment. The powder characteristics are summarized in table 4.2.

Table 4.2: Properties of the used isotropic powder from Magnequench Corporation.

name	$(BH)_{\max}$ (KJ/m ³)	B_r (mT)	H_c (A/m)	H_{cJ} (A/m)	ρ (g/cm ³)
MQP-S-11-9	85	750	440	700	7.43

The powder has a maximum operation temperature of 140 – 180 °C, and a maximum process temperature of 350 °C. The Currie temperature of the powder is 320 °C.

The compounds consist of different filler fractions of the isotropic NdFeB particles. With the densities of the powder ($\rho_{\text{NdFeB}} = 7.43 \text{ g/cm}^3$), the matrix materials ($\rho_{\text{PA11}} = 1.04 \text{ g/cm}^3$, $\rho_{\text{PA11}} = 1.01 \text{ g/cm}^3$), and the compounds (table 4.1), the filler fractions of the compounds ϕ_f can be calculated to 52 vol.% for Neofer[®] 25/60p and 74 vol.% for Neofer[®] 65/70p.

The morphology of the NdFeB particles is identified by scanning electron microscope (SEM) (FEI Quanta, 200 FEG) images. The samples are Au-coated with a sputter coater (Quorum, Q150T S). As pictured in figure 4.1, the mean diameter of these spherical powder particles is approximately $45 \mu\text{m}$ with a standard deviation of $20 \mu\text{m}$. Both the spherical powder and bimodal particle size distribution of this powder offers many advantages for injection molding and the production of advanced applications. The bimodal size distribution feature enables high filler fractions in bonded magnets [46].

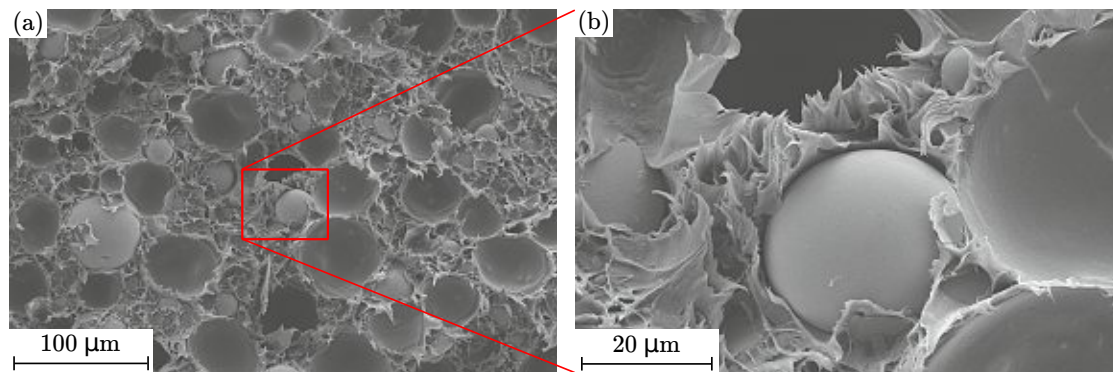


Figure 4.1: Scanning electron microscopic (SEM) image of Neofer[®] 25/60p. (a) Magnification of 1000x. (b) Detail of the image (magnification 5000x).

To expand the range of processable magnetic filaments and for a deeper understanding of the production process of polymer-bonded magnets, self-mixed compounds would be a benefit for this work. For this reason, and for the extrusion of the Neofer[®] compound granules into filaments, a cooperation agreement with the Department of Polymer Engineering and Science at the Montanuniversität Leoben is entered.

4.2.3 Feedstock Production

As described in section 2.11, the ultimate strength of highly filled compounds decrease with increasing filler fraction. This leads to brittle filaments for large filling fractions.

This section describes the compounding process to produce feedstocks out of the matrix materials and the magnetic filler with enhanced mechanical properties. The first feedstock is a compound of PA12 (Polyking, 221-TR) and the magnetically isotropic powder MQP-S-11-9 from Magnequench with a filler fraction of 45 vol.% as described above. It has a lower filler fraction as Neofer[®] 65/70p, but the same PA12 matrix. This leads to better mechanical properties, as well as the possibility to use the mixing extruder capability of the 3D printer to mix the compound filament with a pure PA12 filament in any ratio.

The second compound is a more sophisticated formulation from the Department of Polymer Engineering and Science of the Montanuniversität Leoben. The matrix consists of 30 vol.% thermoplastic elastomer (TPE) and 15 vol.% Polypropylen (PP), the filler is the same MQP-S-11-9 powder with a filler fraction of 55 vol.%. TPEs are plastics that behave similarly to conventional elastomers at room temperature, but can be formed by heat input and thus exhibit thermoplastic behavior [21]. This compound mixture is more ductile as compounds with comparable filler fractions. All materials are dried at 80 °C for 8 hours to guarantee a moisture-free material.

These feedstocks are compounded in a co-rotating twin-screw extruder (figure 2.14), specially designed for compounding of highly-filled polymers with metal or ceramics (Leistritz Extrusionstechnik GmbH, ZSE 18 HPe-48D). The heating zones of the twin-screw are temperate. The feed section is the coolest with 80 °C, and the temperature increases up to the shaping die, which has a temperature of 260 °C. Screw rotation is set at 900 rpm. To avoid oxidation processes of the magnetic material, the extruder has a vacuum degassing system. The extruded compound is pulled away from the die with a conveyor belt (Reduction Engineering Scheer) and later granulated in a cutting mill. All four feedstock compounds are further processed into filament by the aim of another extruding process.

4.3 Filament Extrusion

The prefabricated Neofer[®] compound materials, as well as the produced feedstocks have a granules form with a size of around 5 mm. To prepare the filaments with a diameter of 1.75 mm a single screw extruder (Dr. Collin GmbH, FT-E20T-MP-IS) is used. The extruder barrel has five heating zones and they are set at 180/200/205/205/210 °C.

The die is also heated to a temperature of 220 °C. The rotational speed of the screw is set at 90 rpm. At the outlet of the die, a polytetrafluoroethylene (PTFE) conveyor belt (Geppert-Band GmbH) is placed to pull the filament as it is extruded. After the filament pass the conveyor belt, it is guided to a spooling device with the help of a haul-off unit. Finally, the filament is wound into spools using a spooling device made by the Montanuniversität Leoben. The diameter and ovality of the produced filament are controlled by a diameter-measuring system (Sikora Laser, Series 2000). A schematic sketch of the filament extrusion line is shown in figure 4.2.

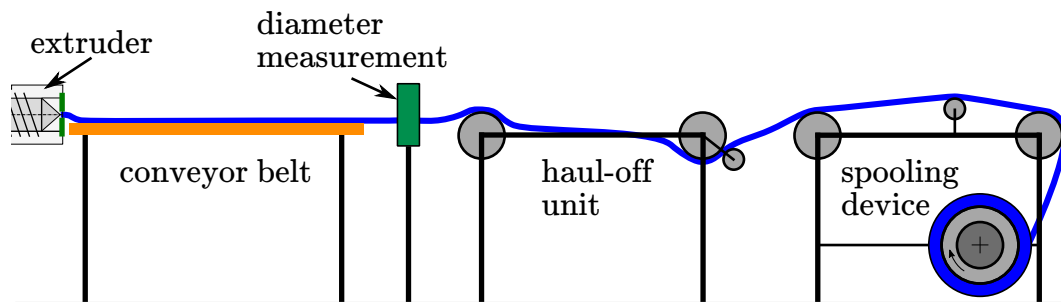


Figure 4.2: Sketch of the filament extrusion line.

According to the measured diameter of the filament, the haul-off and the spooling speeds are manually regulated to obtain a filament with an appropriate diameter of 1.75 ± 0.2 mm. Due to the high filling fraction of the Neofer[®] 65/70p compound and the accompanying brittle structure of the filaments, it is unfortunately impossible to spool this filaments. However, all other filaments are coiled on spools as pictured in figure 4.3.

4.4 Filament Quality

3D printing filament is the construction material used by a 3D printer and its importance cannot be underestimated when aiming for top-quality results. A 3D printer with an advanced extruder can produce high-quality prints with many different materials. Nevertheless, the finest calibration and most carefully printable designing leads to printing failures if the filament has a poor quality. Among others, there are three main quality criteria for the filament quality. The first one is that the filament is free from air-pockets and it has a low moisture content. These errors of the filament can cause

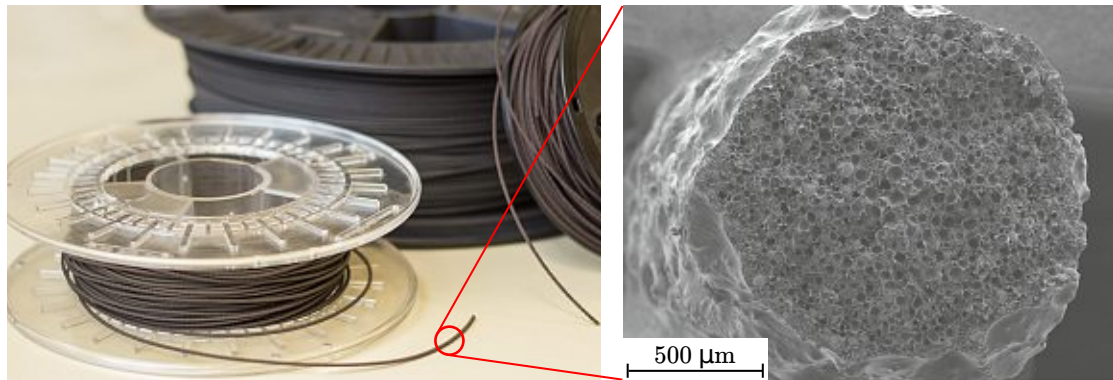


Figure 4.3: Picture of the extruded and spooled filaments, as well as a SEM image of the Neofer[®] 25/60p filament.

to blowouts as the filament is heated, or gaps in the printed model. A solution for this problem is to dry the source materials before the filament extrusion process, as well as uses a degassing system to remove the air pockets in the filament. A special problem of highly filled compound filaments are the fact that the filler particles can result in a intermittent blocking and unblocking of the nozzle. Therefore, a rule of thumb is that the nozzle diameter should be around 8x larger as the particle size to avoid clogging of the nozzle. In our case, a minimum nozzle diameter of 0.4 mm works well.

The other two important quality criteria are the tolerances of the diameter and the roundness of the extruded filament. The used filaments should be both consistently round and consistent in its diameter along the length of the spool. The cross-sectional area of the filament and therefore, the diameter of the filament determines the amount of extruded material through the nozzle. The flow-rate of the extruded material (mm/s) and feed-rate, what is the extruder movements relative to the printer bed (mm/s), connect the filament diameter D with the extrusion width W and the layer height t . For small errors ϵ_D of the filament, a linear approximation of the width error ϵ_W can be considered. This leads to a minimum extrusion width error of $\epsilon_W = 2\epsilon_D$. The same tolerance on a filament with smaller diameter leads to greater difference in the extrusion width area. Identical tolerances for both 3 mm and 1.75 mm filament will result in nearly two times the error for 1.75 mm. Figure 4.4 shows a sketch of the filament and the extrusion width error. The error of the filament leads to voids inside the 3D printed object. Which in turns leads to reduced magnetic performance of the printed magnet.

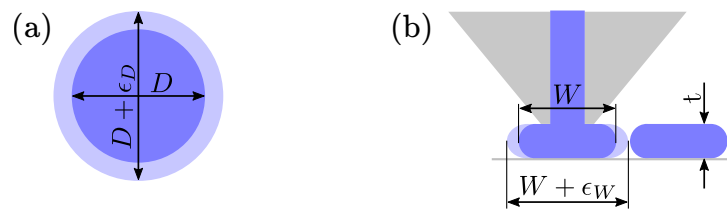


Figure 4.4: Printing errors caused by the filament quality. (a) Change of the filament diameter. (b) Change of the extrusion width due to the tolerances of the filament diameter.

On the one side it would be easier to extrude 3 mm filaments with better tolerances, but there are several disadvantages of the 3 mm filaments: (i) 3 mm filaments, especially highly filled ones, are more rigid, this makes it impossible to coil it on a spool, (ii) more pressure is necessary to press it through the nozzle, (iii) higher printing temperature is required, and (iv) larger extruder heads are necessary.

4.5 Material Characterization

This section describes the material properties of the extruded compounds. Only Neofer[®] 25/60p and the PA12+MQP-S compound are relevant for the 3D printing process. Due to the high filler fraction of Neofer[®] 65/70p, the filament breaks and chokes the rotating parts inside the extruder. The TPE+PP+MQP-S compound is too flexible for our 3D printer. The high flexibility is a result of the high amount of TPE inside the compound. However, two different compounds are processable and works well with the Builder 3D printer.

4.5.1 Thermogravimetry Analysis

To conduct the thermal degradation temperature and the filler fraction of the used compounds, thermal gravimetric analysis (TGA) of the materials are performed. The model TGA 2050 from TA-Instruments has a resolution of $0.2 \mu\text{g}$ and a temperature range of $25 - 1000 \text{ }^\circ\text{C}$. In our case, a heating rate of 10 K/min and a nitrogen atmosphere to avoid oxidation of the particles are used. Figure 4.5(a) shows the TGA analysis of the investigated compounds. The corresponding temperature of the peak in the first derivative of weight loss with temperature ($d\Delta w/dT$), is defined as the degradation temperature T_d . It indicates the corresponding temperature to the highest weight loss rate (figure 4.5(b)).

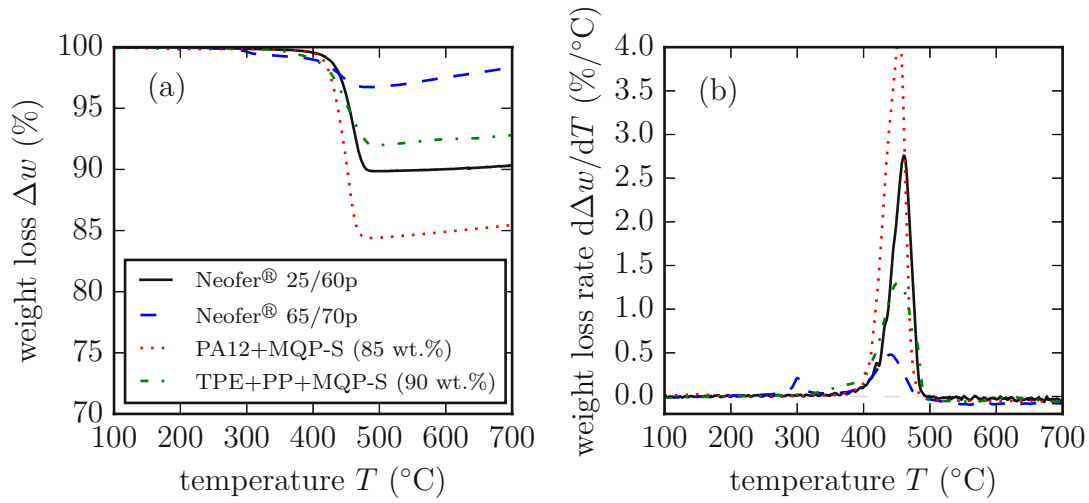


Figure 4.5: Thermogravimetric analysis (TGA) of different compound materials. (a) Weight loss Δw during TGA analysis. (b) Weight loss rate $d\Delta w/dT$ of the analysis.

The results of the TGA are summarized in table 4.3. It clearly shows that the samples with higher amount of magnetic filler have a lower temperature of thermal degradation and lower weight loss rates. The volumetric mass densities for the prefabricated compounds (Neofer[®]) are slightly higher as listed in the data sheets (table 4.1).

Table 4.3: Thermal degeneration temperature T_d , filling mass fraction w_f , volume fraction ϕ_f , and the calculated volumetric mass density ρ obtained from TGA curves.

sample	T_d (°C)	w_f (wt.%)	ϕ_f (vol.%)	ρ (g/cm ³)
Neofer [®] 25/60p	460	89	52.0	4.41
Neofer [®] 65/70p	440	96	76.5	5.92
PA12+MQP-S (85 wt.%)	450	84	41.6	3.68
TPE+PP+MQP-S (90 wt.%)	450	93	64.4	5.14

Obviously, the weight loss Δw increases at higher temperatures. This is allegeable by the nitrogen atmosphere during the test. On the one hand it avoid oxidation processes of the NdFeB particles, on the other hand the nitrogen can react with the elements of the powder to form nitrides. However, the nitrogen does not influence the determination of the degeneration temperature as well as the filling fraction. To avoid the formation of nitrides at high temperatures, an argon atmosphere is preferable.

4.5.2 Volumetric Mass Density of Printed Structures

To archive best magnetic properties, a high volumetric mass density of the 3D printed structures is desirable (equation 2.12). Conventional manufacturing methods like IM press the melted compound with a pressure up to 400 bar into the cavity. Due to the high injection pressure, the end product has a volumetric mass density of $\rho_{\text{comp}} = (1 - \phi_f)\rho_{\text{polymer}} + \phi_f\rho_{\text{NdFeB}}$. The 3D printing FDM process creates an object layer-by-layer. Even if the fill density in the slicer parameter is adjusted to 100 %, small defects on the infill occur. To estimate the deviation of the maximum volumetric mass density ρ_{comp} and the density of 3D printed structures, two different measurement methods are performed.

Scale Method

To determine the volumetric mass density ρ of 3D printed and IM structures consisting of Neofer[®] 25/60p, respectively and of PA12+MQP-S (85 wt.%), three cubes with a side length of $a = 10$ mm are printed and milled, respectively. This rough cubes are further grind to a side length of $a = 5 \pm 0.02$ mm. The mass of the cubes are measured with an analytical balance (ME 235P-OCE, Sartorius), with a precision of 0.01 mg. The volumetric mass density ρ of a cube with the side length of a is

$$\rho = m/a^3 \quad (4.1)$$

with the mass m of the cube. To determine the maximum measurement uncertainty, a error propagation calculation can be performed

$$\Delta\rho = \left| \frac{\partial\rho}{\partial m} \right| \Delta m + \left| \frac{\partial\rho}{\partial a} \right| \Delta a = \frac{\rho}{m} \Delta m + \frac{3\rho}{a} \Delta a . \quad (4.2)$$

Table 4.4 lists the measured side length a , mass m , and the calculated volumetric mass density ρ of the tested compounds. The measured ρ for the 3D printed and the

Table 4.4: Calculation of the volumetric mass density ρ for 3D printed and IM Neofer[®] 25/60p, and PA12+MQP-S (85 wt.%) compound.

sample	method	m (mg)	a (mm)	ρ (g/cm ³)
Neofer [®] 25/60p	3D printed	446 ± 1.4	5 ± 0.02	3.57 ± 0.05
	IM	544 ± 1.1	5 ± 0.02	4.35 ± 0.06
PA12+MQP-S (85 wt.%)	3D printed	406 ± 1.5	5 ± 0.02	3.25 ± 0.05

IM cube of Neofer[®] 25/60p deviates of around 22 %. For the PA12+MQP-S (85 wt.%) prints, the deviation between the measured and the theoretical value is approximately 15 %. This result can be interpreted that for the used setup, printer and slicer parameter, prints with the PA12 matrix filaments have a higher volumetric mass densities as comparable prints with a PA11 matrix.

3D μ -CT Investigation

To proof the former measurements of Neofer[®] 25/60p based on the scale method, a 3D micro-computer-tomograph (μ -CT) scan is performed to investigate the porosity of the 3D printed sample. The morphology is visualized in a SkyScan 1173 3D μ -CT device from Bruker with a source voltage of 130 kV, source current of 61 μ A, brass filter with 0.25 mm, frame average of 4, image pixel size 7.12 μ m, and an exposure time of 1.2 s. The dataset is analyzed with CT Analyser v.1.14.4.1 and CTvox v.3.3. A 3D printed cube of Neofer[®] 25/60p with an edge length a of 5 mm is prepared for the scan. In figure 4.6, the density distribution of the scan on different cross-sections is shown. It can be seen, that the density of the magnetic material (green) is higher for the first layers of the sample. The μ -CT scan results in a 26 % lower density as compared with full-dense injection molded parts. This is 4 % lower as measured by the scale method.

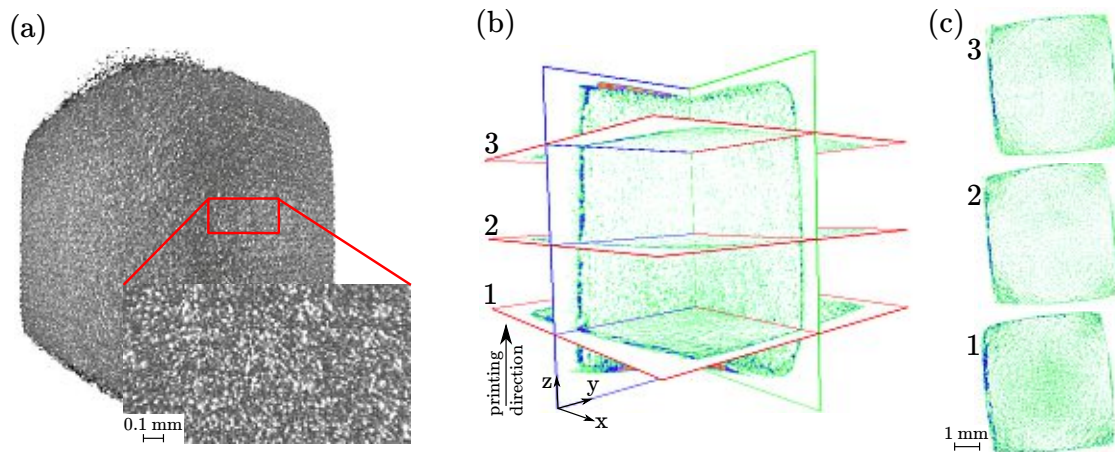


Figure 4.6: 3D μ -CT scan of a 3D printed cube ($a = 5$ mm) made of Neofer[®] 25/60p. (a) Surface of the printed cube, The spherical magnetic particles are clearly visible. (b) Cross-section of the scan with multiple planes orthogonal to the printing direction. (c) Topview of μ -CT scans orthogonal to the printing direction.

4.5.3 Magnetic Properties

The most important material parameters of this work are the magnetic properties of the 3D printed structures. This section describes these properties of the Neofer[®] 25/60p and the PA12+MQP-S compound.

Analysis Methods

To determine the magnetic properties of hard magnetic materials, hysteresis loop measurements are mandatory (figure 2.9). To measure the complete hysteresis loop, a sufficient high external magnetic field is required. Generally, this field should be two or three times larger than the coercive field [100]. Systems to measure the hysteresis loop can be divided into magnetically open and closed systems. For open systems, the internal field H_{int} is related to the external field H_{ext} (see also section 2.2.3)

$$H_{\text{int}} = H_{\text{ext}} - N \frac{J(H_{\text{ext}})}{\mu_0}. \quad (4.3)$$

The demagnetization factor N is equal to zero for a closed system, whereas N depends on the shape of the magnetic object for an open system. The demagnetizing factor of a uniformly magnetized ferromagnetic prism can be calculated according to equation A.2. To obtain the correct tilt of the hysteresis loop, the measured polarization $J(H_{\text{ext}})$ needs to be corrected to $J(H_{\text{int}})$.

An example of a magnetically closed system is a hysterezigraph. It uses an electromagnet to magnetize the device under test (DUT). Pickup coils detect the time variation of the polarization and the magnetic field strength (dJ/dt , dH/dt), respectively. Two integrators are necessary to process the signal from the pickup coils. The measurement procedure and requirements are defined in DIN EN 60404-5. Hysteresis measurements by a hysterezigraph is most common in industry.

The most sensitive system to measure magnetic fields changes is currently the superconducting quantum interference device (SQUID). It is able to detect field changes in the range of femto-Tesla. The principle is based on the magnetic flux quantization and the Josephson effect. A SQUID magnetometer is a open system therefore, the shape of the object influences the measurement.

The next two methods are relevant for this project, because they are available and usable for us at the TU Wien. The first one is the vibrating sample magnetometer (VSM).

fect changes the shape of the hysteresis loop as well as the coercivity of the investigated sample. Figure 4.8 shows hysteresis measurements of a IM sample of Neofer[®] 25/60p with different analysis methods. The data sheet values is a provided hysteresis curve from Magnetfabrik Bonn GmbH. It is measured accordingly DIN EN 60404-5 with a magnetically closed measurement setup. It is obvious that the VSM measurement fits very well with the data sheet values. On the other side, PFM measurements of the hysteresis loop differ compared with VSM measurements.

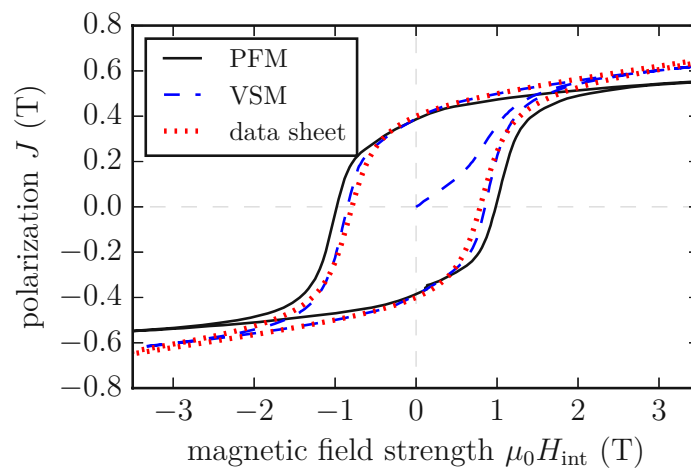


Figure 4.8: Hysteresis measurement of a IM sample of Neofer[®] 25/60p with different characterization methods.

The VSM measurements at the TU-Wien, are performed by a PFM11 from Hirst Industrial System. It charges a 22.5 kJ capacitor bank ($C = 5$ mF) to 3 kV in approximately 25 s. The whole charging process of the PFM, $f/2f$ selection (40 ms and 57 ms) and the data acquisition is computer controlled by using a Z80 microprocessor. The signal is integrated with a stable analogue integrator with selectable time constants, and further processed by an ADC card (PCI-416N, Datel) with a A/D sampling rate of 5 MHz and 14-bit A/D resolution. The system is capable of accepting samples up to 30 mm diameter and 10 mm length within a ± 1 % pickup coil homogeneity range. The maximum field is 5 T. It is calibrated with an absolute error in H and J of ± 1.5 % [103].

Results

Hysteresis measurements of the used filaments (Neofer[®] 25/60p and PA12+MQP-S) are performed by PFM, and VSM to measure the temperature dependence. For PFM measurements, cubes with a side length of $a = 10 \pm 0.2$ mm are printed. The deviation of the nominal size of a is too high for adequate hysteresis measurements. Therefore, the cubes are further processed by cutting and grinding to archive a side length of $a = 5 \pm 0.02$ mm. For VSM measurements, thin plates with a size of $4 \pm 0.05 \times 4 \pm 0.05 \times 0.25 \pm 0.05$ mm³ (L×W×H) are prepared. The demagnetization factor N (equation A.2) for a cube and for a thin plate with these dimensions is 1/3 and 0.07, respectively.

The first test investigates the magnetic isotropic behavior of the 3D printed cubic test specimens of the Neofer[®] 25/60p compound. PFM hysteresis measurements are performed in x , y , and in z magnetization direction to identify the magnetic behaviors of the layer structure of the printed cubes. All these measurements are carried out with the same parameters - temperature of 297 K and a magnetic field up to 4 T peak field. Figure 4.9(a) shows the hysteresis measurement of IM and 3D printed cubes for each magnetization direction. The injection molded sample shows an isotropic behavior, like the 3D printed cube which indicates, that the layer structure of the printing process is irrelevant for the magnetic properties. For the IM sample, B_r differ between the data sheet and the measured value of around 4 % (table 4.1) This deviation can be explained by the difference between VSM and PFM measurements as mentioned above. The deviation of the volumetric mass density ρ between the IM and the printed cube is 22 % and therefore, in the same range as the deviation of B_r of 25 %. The measured remanence B_r , the intrinsic coercivity H_{cj} , and the volumetric mass density ρ of the compounds are listed in table 4.5.

The temperature dependence of the compound materials is of vital importance for applications and the printing process. For this reason, temperature depended VSM measurements of both materials are performed. After magnetization of the sample (4 T) at 450 K, the remanence is measured subjected to to temperature ($B_r(T)$). For the investigated temperature range between 300 – 450 K, B_r shows a linear behavior. No VSM measurements are possible above 450 K, because the matrix material becomes pasty, which could damages the VSM. Figure 4.9(b) shows the relation $B_r(T)$ for the Neofer[®] 25/60p compound. The temperature coefficient α is -0.18 %/K and

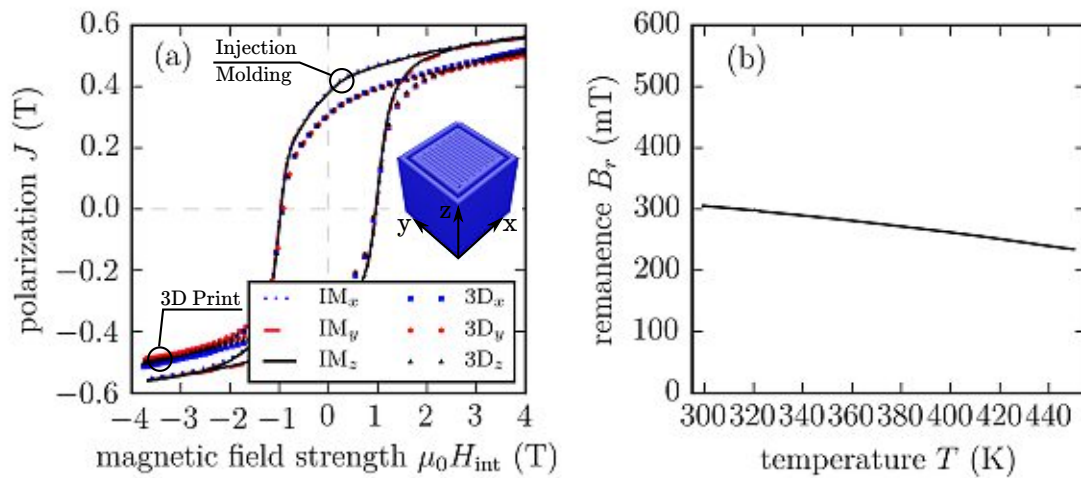


Figure 4.9: Magnetic properties of 3D printed Neofer[®] 25/60p. (a) PFM measurement of all three directions of space to investigate the isotropic behavior of the layered 3D printed cube. (b) VSM measurement of the temperature dependence of the remanence B_r .

-0.19%/K for the Neofer[®] 25/60p and the PA12+MQP-S compound, respectively. The complete hysteresis loops for various temperatures are shown in figure 4.10.

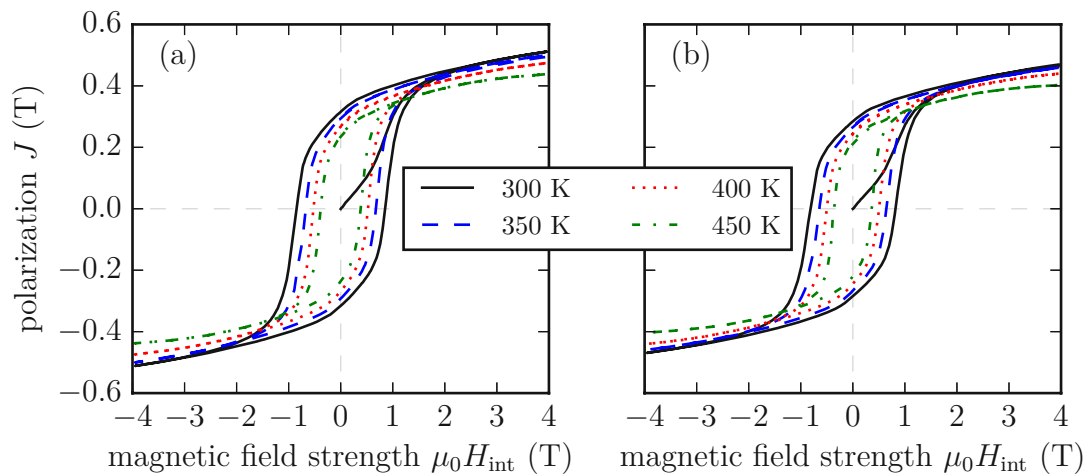


Figure 4.10: VSM measurements at different temperatures. (a) Neofer[®] 25/60p. (b) PA12+MQP-S-11-9.

A big advantage of the 3D printing setup with a mixing extruder is the possibility to mix two different materials as mentioned in section 3.1.1. With this feature, structures of a mixture of PA12+MQP-S compound and pure PA12 can be printed. This means

that B_r can be adjusted between 100 % and 0 % of the maximum value (4.5) for individual sections of the print and layers, respectively. To investigate the magnetic properties, cubes with different compound fractions ϱ_m are printed and measured in the PFM. Figure 4.11 shows the hysteresis loops for different ϱ_m and the dependence of $B_r(\varrho_m)$. It is obvious that B_r decreases linearly with the magnetic compound fraction ϱ_m , but the intrinsic coercivity H_{cJ} is independent of the compound fraction. This test confirms equation 2.12 and the assumptions of section 2.3.3.

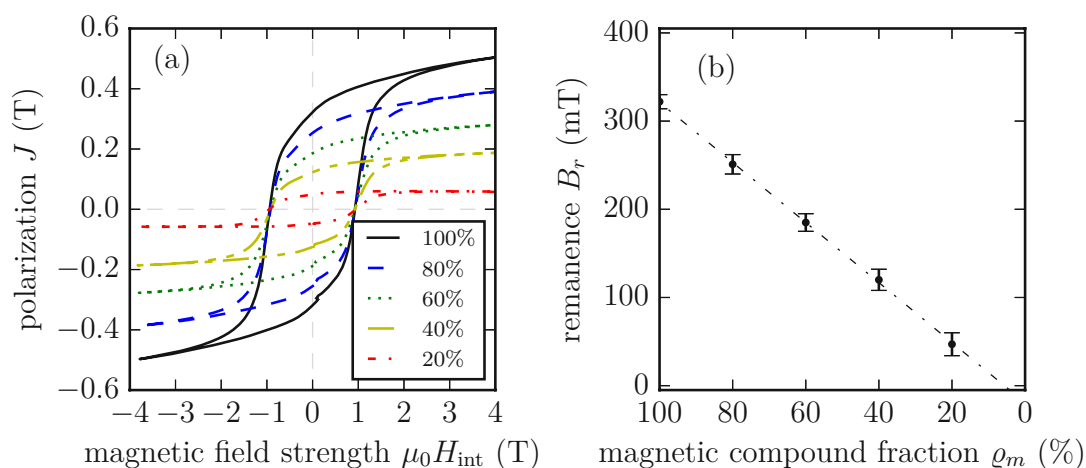


Figure 4.11: PFM measurements of PA12+MQP-S-11-9 with different compound fractions ϱ_m . (a) Hysteresis loops for different ϱ_m . (b) Remanence B_r for different ϱ_m .

Table 4.5: Summary of the magnetic properties of the 3D printed samples.

sample	B_r (mT)	H_{cJ} (kA/m)	α (%/K)
Neofer [®] 25/60p	310	740	-0.18
PA12+MQP-S (85 wt.%)	314	745	-0.19

4.5.4 Tensile Test

Mechanical properties of the working piece are of crucial importance for the design and the functionality. For this reason, tensile tests of pure PA12 and Neofer[®] 25/60p are performed. The standard test method for tensile properties of plastics is defined in ASTM Standard D638-10. The standard type-IV specimen specified in ASTM Standard D638-10 is printed (printer parameter as listed in table 3.1) for both materials. This dog-bone shaped specimen has a rectangular cross-section, 3.2 mm thick and 6 mm

wide. The total length of the specimen is 115 mm. The gauge length of the test section is 60.08 mm [104]. To reduce the statistical uncertainty and to determine the degree of variability in microstructure and mechanical properties between samples, four test structures are printed and tested for both materials. Pictures of the printed specimens before testing are shown in figure 4.12(a)(c).

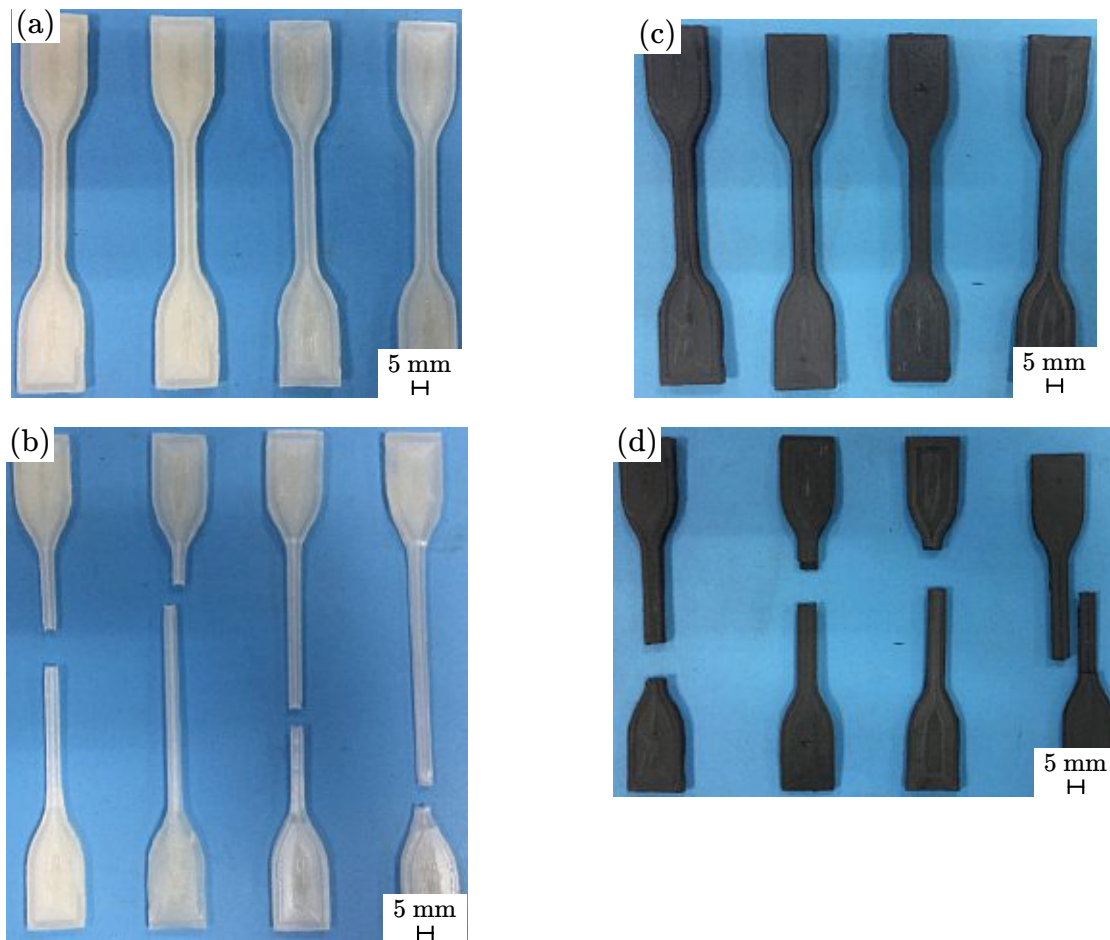


Figure 4.12: ASTM D638-10 Type IV specimens for tensile tests. (a) Prints with pure PA12. (b) PA12 prints after tensile tests. (c) Prints with Neofer® 25/60p . (d) Neofer® 25/60p after tensile tests.

A universal test machine (RM 100, Schenck Trebel) is used for tensile tests. All tests are performed at roomtemperature (295 K). A plot of the tensile stress-strain curves of Neofer® 25/60p and pure PA12 are shown in figure 4.13. The standard deviation of the measurements is marked with pale colors. Pictures of test structures after testing are

pictured in figure 4.12(b)(d). It is clearly visible that the tensile strain at break is much higher for pure PA12.

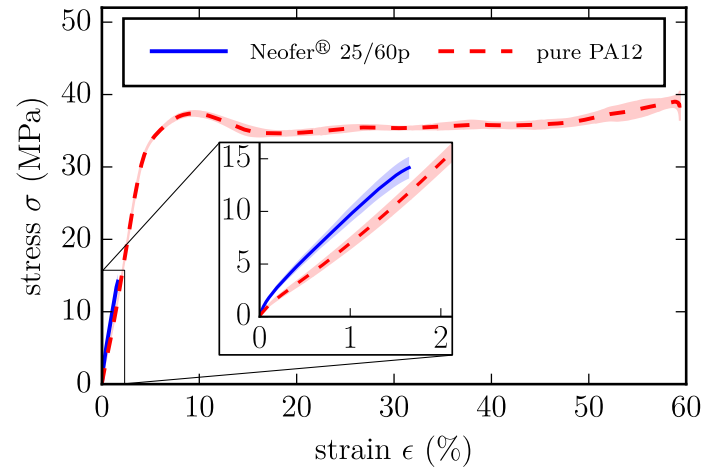


Figure 4.13: Tensile stress-strain test results of Neofer[®] 25/60p and pure PA12.

Mechanical properties of highly filled compounds as Neofer[®] 25/60p significantly depends on the powder fraction as well as the morphology of the powder particles. Polymer-bonded magnets made of irregular melt-spun powders have a higher tensile strength compared to those made from atomized spherical powders [64].

Test results of tensile tests are summarized in table 4.6. Manufacturer's data for tensile strength σ_m of pure PA12 (Polyking, 221-TR) is $\sigma_m = 60$ MPa and $\sigma_m = 30$ MPa for for Neofer[®] 25/60p. Therefore, the printing process halves the tensile strength σ_m . It should note, that the tool path (see section 3.1.2, as well as the fill density of the FDM printing process has a crucial impact on the tensile strength of the produced object [105].

Table 4.6: Tensile test results of Neofer[®] 25/60p and pure PA12. σ_m ...tensile strength, E ...Young's modulus, σ_b ...tensile fracture stress, and ϵ_b ...tensile strain at break.

sample	σ_m (MPa)	E (MPa)	σ_b (MPa)	ϵ_b (%)
pure PA12	38.95 ± 2.51	1099.52 ± 319.72	34.98 ± 4.72	65.75 ± 5.01
Neofer [®] 25/60p	14.46 ± 1.05	2192.48 ± 164.21	13.477 ± 1.17	1.81 ± 0.17

4.5.5 Dynamic Mechanical Analysis

The mechanical tensile test of last section is a quasi-static test procedure, but polymers are viscoelastic materials, i. e. they show viscous and elastic properties at the same time. The viscoelastic behavior depends on the temperature and the measurement frequency. The dynamic-mechanical analysis (DMA) enables the determination of the linear mechanical properties of polymer materials at different temperatures and measurement frequencies. The method is applicable to polymeric solids and melts.

The DMA measurement system (DMA 8000, Perkin Elmer) has a temperature range from -150 to $+600$ ° C and a frequency range between $0.01 - 500$ Hz. It has a force resolution of 1 nN and 5 nm for the length. Figure 4.14 shows the DMA measurements for pure PA12, PA12+MQP-S (85 wt.%), and Neofer[®] 25/60p at a measurement frequency of 1 Hz and 10 Hz. Detailed measurements of the storage modulus E' , loss modulus E'' and the dissipation factor $\tan(\delta) = E''/E'$ are performed. This tests give just a qualitative description of the material behavior, because to determine the absolute values of E' and E'' , a calibration of the DMA system would be necessary. An increase in the filler content shifted the glass transition (the peak in the loss modulus) to higher temperatures. This indicates that the powder particles constrained the polymer component [106]. It is also clearly visible that a higher filler content decrease the damping behavior of the material [107].

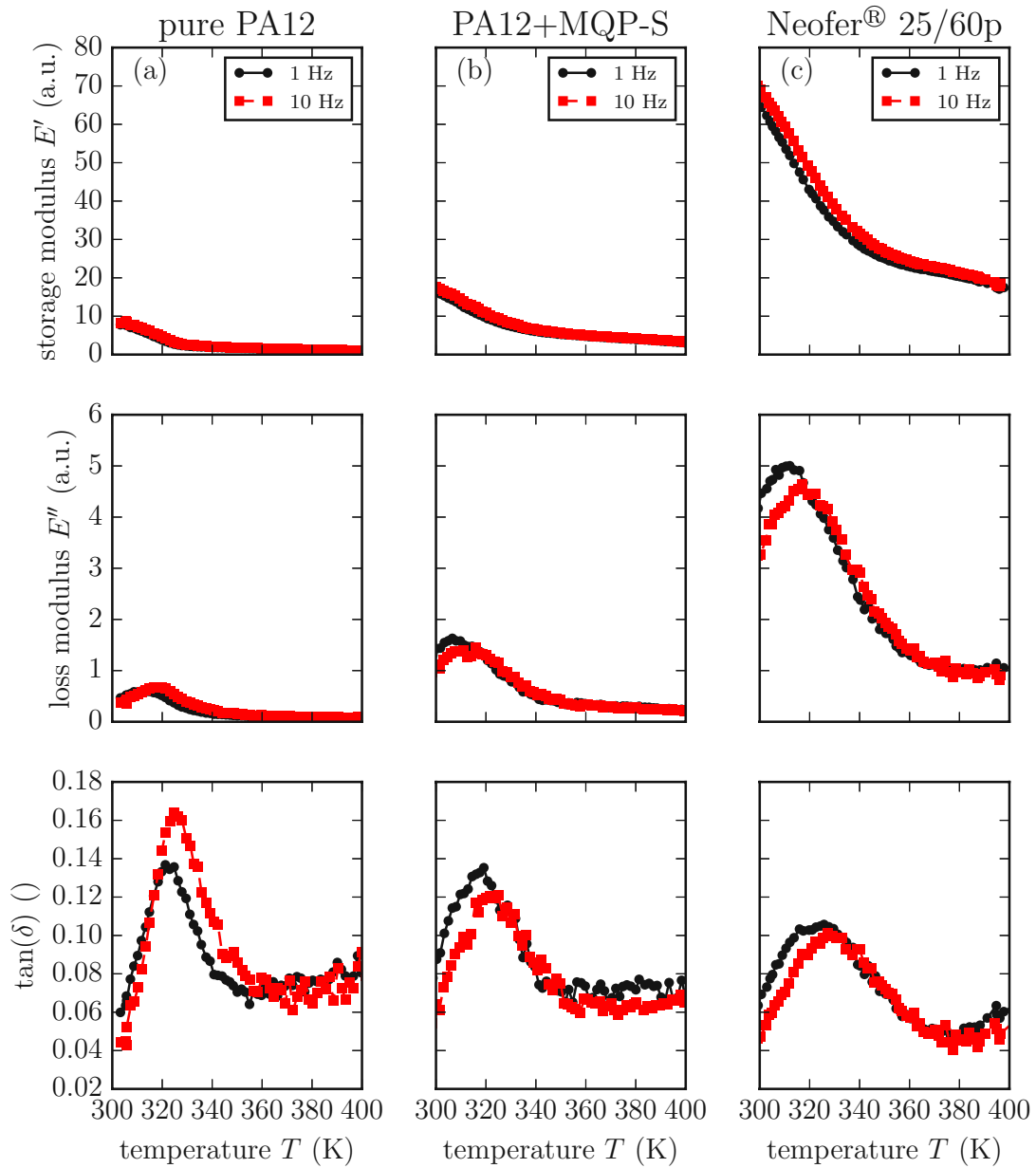


Figure 4.14: Dynamic-mechanical analysis (DMA) measurements of: (a) pure PA12, (b) PA12+MQP-S (85 wt.%), and (c) Neofer[®] 25/60p at a measurement frequency of 1 Hz and 10 Hz.

5 Simulation Framework

Portions of this chapter were previously published in [97,98] and have been reproduced with permissions of the coauthors and in accordance with the publisher's policy. Content which was not generated by the author of this thesis is explicitly denoted, copyright is held by Nature Publishing Group and American Institute of Physics.

5.1 Introduction

The main advantage of AM methods is the possibility to easily print objects with an arbitrary shape or even with a variable magnetic compound fraction in defined regions of the object. To get the most out of the 3D printed methodology, simulation tools are required to calculate the magnetic field distribution of a given printed structure. Several commercial finite-element (FEM) software packages exist (e.g. Comsol Multiphysics, Ansys, FEMME, Magnum.fe) to solve this so called Maxwell's magnetostatic forward problem. In contrast to the forward problem, the inverse problem, where, for a given magnetic field H outside the magnet, the magnetization M or polarization J within the magnet is reconstructed, is much harder to solve (figure 5.1).

A simulation framework based on a pure FEM implementation is introduced, as well as an implementation of an inverse stray-field code. The forward problem is a well-posed problem. This means, a solution exists and the solution is unique. On the other side, the inverse problem is ill-posed. To provide an approximated solution of the inverse problem, additional information is necessary. Different methods exist to find reasonable results [108]. This framework is a powerful tool to calculate the compound fraction or even the topology of an object for a desired external field distribution.

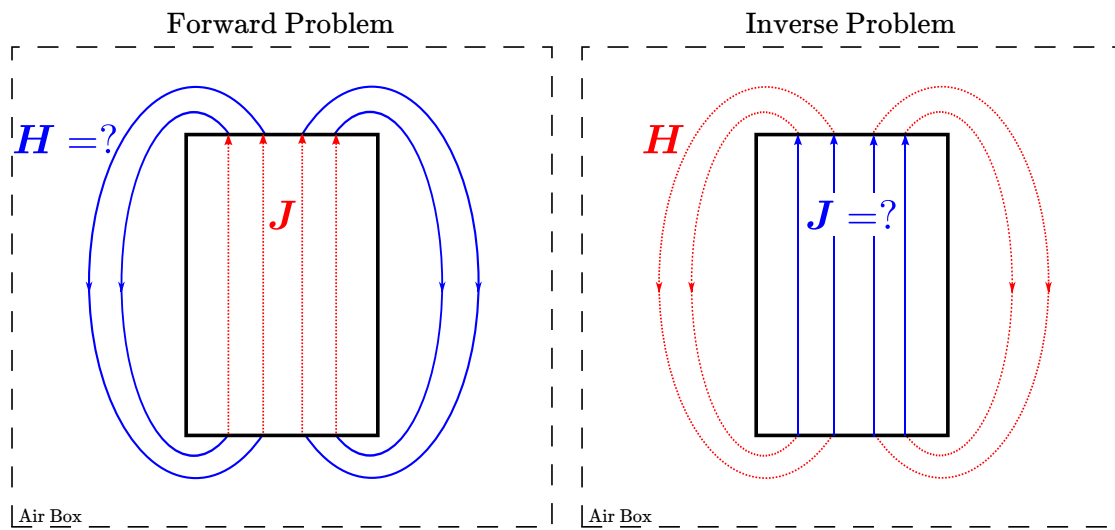


Figure 5.1: The forward problem computes the stray field H of a given object with a polarization J . This is a well-posed problem, with a unique solution. It is easy to compute with modern FEM simulation algorithms. For the inverse problem, outgoing from a predefined stray field H (i.e. a 3D field scan in a defined region outside the magnet) the polarization J should be calculated. It is an ill-posed problem and therefore, no exact solution exists. To solve this problem, a regularization method is necessary.

5.2 Stray Field Computation

This section deals with the solution of the Maxwell's magnetostatic forward problem. An implementation of linear isotropic magnetic materials (hard and soft) is described. Several benchmarks and numerical experiments show the effectiveness of this method.

5.2.1 Demagnetization Field

The demagnetization field, also called magnetic stray field, is the magnetic field H generated by the magnetization M of a magnet. Due to the long-range effect of H (the demagnetization field $H(r)$ depends on M at every point of the magnet), most naive numerical algorithms scale with $\mathcal{O}(N^2)$, where N is the number of degrees of freedom of the problem. Numerical methods for the calculation of the demagnetization field can be divided into three groups: (i) variational methods (e.g. FEM methods [109]), (ii) integral methods (e.g. fast Fourier-transform methods [110]) and (iii) a combination of them (e.g. FEM-BEM coupled methods [111]). A detailed introduction of some advanced algorithms can be found in [112].

In this work, the computation of the demagnetization field is implemented with a variational (FEM) method. The calculation is based on the classical linear and isotropic Maxwell's equations for electrostatics with current $\mathbf{J} = 0$

$$\nabla \cdot \mathbf{B} = 0 \quad (5.1)$$

$$\nabla \times \mathbf{H} = 0. \quad (5.2)$$

The constitutive equation in electromagnetism (equation 2.2) must be divided into three regions based on their magnetic characteristics. (i) The air space Ω_a outside a material, (ii) a ferromagnetic (soft magnetic) material region Ω_s , and (iii) a permanent magnetic material region Ω_p .

Air region Ω_a

$$\mathbf{B}_a = \mu_0 \mathbf{H}_a \quad (5.3)$$

where μ_0 is the vacuum permeability ($\mu_0 = 4\pi \times 10^{-7}$ Vs/(Am)).

Soft magnetic region Ω_s

$$\mathbf{B}_s = \mu_0 (\mathbf{H}_s + \mathbf{M}_s) = \mu_0 \mu_r \mathbf{H}_s \quad (5.4)$$

where μ_r is the relative permeability (for ferromagnetic materials: $\mu_r \gg 1$).

Permanent magnetic region Ω_p

$$\mathbf{B}_p = \mu_0 \mu_m \mathbf{H}_p + \mu_0 \mathbf{M}_0 \quad (5.5)$$

where μ_m is the recoil permeability of a permanent magnet. It is defined as the slope of the demagnetization curve (II quadrant of the hysteresis curve, figure 2.9(c)). Typical values for μ_m of RE magnets are between 1.05 and 1.20, and between 1.40 and 2.00 for polymer-bonded RE magnets [113]. $\mathbf{M}_0 = \mathbf{B}_r / \mu_0$ is the residual magnetization vector, with the remanence \mathbf{B}_r of the PM.

There exists two approaches to solve these governing equations. A magnetic scalar or a vector potential can be used to solve the above equations. The scalar potential can only be used if the current \mathbf{J} vanishes as in equation 5.2. Nevertheless, if the model

describes only linear magnetic materials ($\mu_r = \text{const.}$ and $\mu_m = \text{const.}$), the scalar potential is more advantageous, since it has only N degrees of freedom compared to $3N$ degrees of freedom for the vector-potential approach.

According to Helmholtz's theorem, the magnetic field \mathbf{H}_i can be expressed as the gradient of a scalar potential u

$$\mathbf{H}_i = -\nabla u_i \quad (5.6)$$

where $i \in \{a, s, p\}$ defines the three different regions. The magnetic field density \mathbf{B} of the entire space can be summarized to

$$\mathbf{B} = \begin{cases} -\mu_0 \nabla u & \text{for } \mathbf{r} \in \Omega_a \\ -\mu_0 \mu_r \nabla u & \text{for } \mathbf{r} \in \Omega_s \\ -\mu_0 \mu_m \nabla u + \mu_0 \mathbf{M}_0 & \text{for } \mathbf{r} \in \Omega_p. \end{cases} \quad (5.7)$$

In order to get a unique solution, a proper boundary condition is necessary. Far-away from the permanent magnetic region Ω_p , the magnetic field must fulfill the relation $\lim_{|\mathbf{r}| \rightarrow \infty} \mathbf{H} = 0$. This leads to the open boundary condition of the system

$$u(\mathbf{r}) = \mathcal{O}(1/|\mathbf{r}|) \quad \text{for } \mathbf{r} \rightarrow \infty. \quad (5.8)$$

5.2.2 Finite-Element Method

To find the demagnetization field of a complex problem, Poisson's PDE needs to be solved. This problem can be simplified by using the weak formulation of the Poisson equation. Weak form means, instead of solving the PDE of the underlying problem, an integral function is solved. The weak formulation leaves the requirements for smoothness and differentiability of the solution. By the choice of a suitable discrete function space, the PDE can be turned into a linear system of equations

To derive the weak formulation of the problem, equation 5.1 with the magnetic field density \mathbf{B} (equation 5.7) is multiplied by a so-called test function v and integrated over a region Ω

$$\int_{\Omega} \nabla \cdot \mathbf{B} v d\mathbf{r} = 0 \quad (5.9)$$

integration by parts using Green's identity yields

$$\int_{\Omega} \mathbf{B} \nabla v \, d\mathbf{r} + \underbrace{\int_{\partial\Omega} \mathbf{B} u \, ds}_0 = 0. \quad (5.10)$$

Restriction of the test function v to the Sobolev space H_0^1 and the open boundary condition, leads to a vanishing boundary term. Splitting the whole region Ω into the sub-regions with k soft magnetic regions and m permanent magnetic regions $\Omega = \Omega_a \cup \sum_i^k \Omega_{s_i} \cup \sum_j^m \Omega_{p_j}$ and insert equation 5.7, it can be written as

$$\begin{aligned} \int_{\Omega_a} \nabla u \nabla v \, d\mathbf{r} + \sum_{i=1}^k \left(\int_{\Omega_{s_i}} \mu_{r_i} \nabla u \nabla v \, d\mathbf{r} \right) \\ + \sum_{j=1}^m \left(\int_{\Omega_{p_j}} \mu_{m_j} \nabla u \nabla v \, d\mathbf{r} \right) = \sum_{j=1}^m \left(\int_{\Omega_{p_j}} \mathbf{M}_{0_j} \nabla v \, d\mathbf{r} \right). \end{aligned} \quad (5.11)$$

This formulation can be expressed as

$$a(u, v) = L(v) \quad (5.12)$$

with the bilinear form $a(u, v)$ given by

$$\begin{aligned} a(u, v) = \int_{\Omega_a} \nabla u \nabla v \, d\mathbf{r} + \sum_{i=1}^k \left(\int_{\Omega_{s_i}} \mu_{r_i} \nabla u \nabla v \, d\mathbf{r} \right) \\ + \sum_{j=1}^m \left(\int_{\Omega_{p_j}} \mu_{m_j} \nabla u \nabla v \, d\mathbf{r} \right) \end{aligned} \quad (5.13)$$

and the linear form $L(v)$ given by

$$L(v) = \sum_{j=1}^m \left(\int_{\Omega_{p_j}} \mathbf{M}_{0_j} \nabla v \, d\mathbf{r} \right). \quad (5.14)$$

Existence and uniqueness of the solution u is provided by the theorem of Lax-Milgram [114].

The FEM method is a discrete algorithm. This means, the weak formulation 5.11 must be discretized by finite-elements in a polyhedral mesh. Based on the definition of Ciarlet [115], a finite-element is defined by the:

- Geometric domain Ω_h of any shape where the element basis function is $\neq 0$.

- Local element space V_h of the domain Ω_h , what is a N dimensional vector space. Where N is the number of unknowns per element.
- Degrees of freedom $\psi_1, \psi_2, \dots, \psi_N$ on V_h of the finite-element. The basis function ϕ_i with $i = 1, \dots, N$ follows the relation $\psi_i(\phi_j) = \delta_{ij}$. Where δ is the Kronecker delta.

This work is based on the most common finite-element, the Lagrange element of first order. The geometric domain Ω_h is defined as a tetrahedral in 3D. The local element space is defined as first order polynomials \mathcal{P}_1 .

In order to obtain a discretized form of equation 5.12, the Galerkin approach can be used to find a discretized solution of $u \rightarrow u_h$ in the finite dimensional function space V_h by a tuple of coefficients u_i

$$u_h = \sum_{i=1}^N u_i \phi_i \quad (5.15)$$

where ϕ_i are the global basis functions (figure 5.2). The discrete formulation of the bilinear form 5.13 and linear form 5.14 can be written as

$$a(u_h, \phi_j) = \sum_{i=1}^N u_i a(\phi_i, \phi_j) = L(\phi_j). \quad (5.16)$$

This system can be formulated as a system of linear equations (matrix-vector multiplication)

$$\mathbf{A} \cdot \mathbf{u} = \mathbf{b} \quad (5.17)$$

with the matrix \mathbf{A} and the vector \mathbf{b} given by

$$\mathbf{A} = a(\phi_i, \phi_j) \quad (5.18)$$

$$\mathbf{b} = L(\phi_j). \quad (5.19)$$

Due to the choice of basis functions ϕ_i , which have local support, the system matrix \mathbf{A} is sparse. Solution of the system of equations 5.17 usually requires the inverse the system matrix \mathbf{A} . However, the inverse of a sparse matrix is a dense matrix in general. Computing the inverse of \mathbf{A} can be avoided by application of iterative solvers that

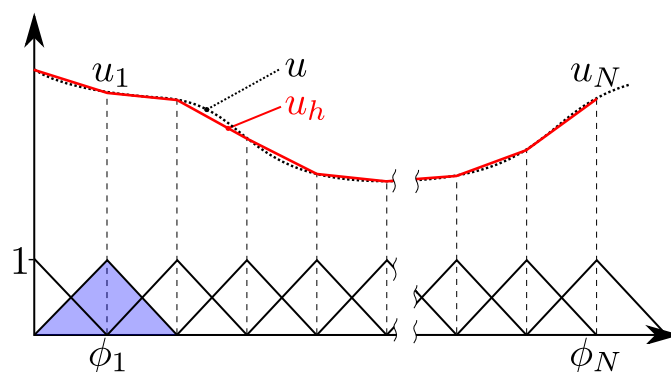


Figure 5.2: Principle of discretization. The 1D function u is approximated by u_h , which is a linear combination of linear basis functions ϕ_i with the coefficients u_i .

require matrix-vector multiplication only. In this work, the iterative numerical generalized minimal residual method (GMRES) is used to solve the linear system [116].

As mentioned above, to get a unique solution of the method, the boundary conditions have to be known. The boundary condition of equation 5.8 must be fulfilled for the calculation of the demagnetization field. Several methods exist to implement this boundary condition into the FEM method [112]. The simplest method to implement it, is the truncation method. It extends the mesh of the air region Ω_a by a large but finite size. At the surface of this extended region, the homogeneous Dirichlet boundary condition is applied. The main advantage of this method is the easy implementation, but on the other hand, due to the large extended region, many elements are added to the mesh, as well as it is not an accurate description of the problem. However, this easy implementation leads to proper simulation results as discussed in section 5.2.4.

5.2.3 Implementation in FEniCS

The finite-element package FEniCS is used to implement and solve the weak formulation (equation 5.17) of the demagnetization field problem and the inverse stray field and topology optimization method that is presented in section 5.3. FEniCS is an open-source software project with the goal to enable automated solution of differential equations [117]. This involves the automation of: (i) discretization, (ii) discrete solution, (iii) error control, (iv) modeling, and (v) optimization [118].

A mathematical problem, formulated in its weak form can be written in the unified form language (UFL) [119]. The core component of FEniCS is the dynamic object-

oriented library for finite element computation (DOLFIN) [120]. Its functionality integrates the other FEniCS components and handles communication with external libraries. Outgoing from an UFL code, the FEniCS form compiler (FFC) automatically generates efficient C++ code for the evaluation and assembly of system matrices [121]. A just-in-time (JIT) compiler enables the evaluation of multilinear forms from a Python scripting environment. Listing 5.1 shows the implementation of the weak formulation of equation 5.17 in FEniCS. The workflow of FEniCS with its different components is visualized in figure 5.3.

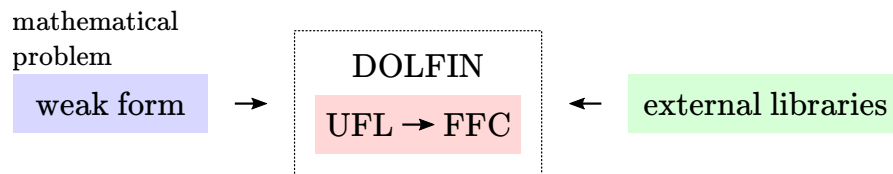


Figure 5.3: Workflow of FEniCS and their components and interplay.

To discretize a model by finite elements in a polyhedral mesh, a mesh generation tool is required. FEniCS provides a tool to generate meshes in 1D, 2D and 3D. However, the integrated meshing tool is only functional for simple models. To mesh a complicated geometry, modeled by CAD programs, the open-source software Salome 7.6 can be used to import CAD files or model a problem with the integrated CAD module. The meshing module of Salome uses a set of meshing algorithms and their corresponding conditions (hypotheses) to compute meshes. Especially the Netgen algorithm and tetrahedral elements are compatible with FEniCS [122].

Listing 5.1: FEniCS implementation of the weak formulation of the demagnetization field problem as described above.

```

1  # Function space of the mesh
2  V = FunctionSpace(mesh, 'CG', 1)
3
4  # Set up test and trial functions
5  v = TestFunction(V)
6  u = TrialFunction(V)
7
8  # Bilinear form
9  a = inner(grad(u), grad(v))*dx(0) + # Air domain
10     mu_r*inner(grad(u), grad(v))*dx(1) + # Soft magnetic domain
11     mu_m*inner(grad(u), grad(v))*dx(2) # Hard magnetic domain
12
13 # Linear form
14 L = inner(M_0, grad(v))*dx(2)
15
16 # Create Dirichlet boundary condition
17 bc = DirichletBC(V, Constant(0.0), DomainBoundary())
18
19 # Compute solution
20 solve(a == L, u, bc, solver_parameters={'linear_solver': 'gmres'})

```

5.2.4 Validation and Numerical Experiments

The presented implementation of the demagnetization field computation is validated and benchmarked by several tests. The first one compares the analytical stray-field solution of an uniaxial magnetic domain (equation A.3) with the calculated field of the implemented stray field code and the commercial software Magnum.Fe [123]. Magnum.Fe is also based on FEniCS, but compared to the presented truncation method, it uses a hybrid FEM/BEM method to solve the open-boundary problem. An unit cube (side length $a = 1$) with an extended air region around the cube is meshed by Salome. To estimate the discretization error of the problem, the same geometry is meshed with different sizes of tetrahedral elements. The L_2 error-norm between simulation \mathbf{H}_{sim} and the analytical solution \mathbf{H}_{ana} in the permanent magnetic region Ω_p is

$$\|\mathbf{H}_{\text{sim}} - \mathbf{H}_{\text{ana}}\|_2^2 = \int_{\Omega_p} |\mathbf{H}_{\text{sim}} - \mathbf{H}_{\text{ana}}|^2 dr. \quad (5.20)$$

Figure 5.4(a) shows the mesh of the permanent magnetic region Ω_p and the air region Ω_a around the unit cube. In this test, the external region is 5 times larger than Ω_p in each spatial dimension as suggested in [124]. The magnet is calculated as an ideal permanent magnet with a recoil permeability of $\mu_m = 1$ (the magnetization is independent from the acting field). Figure 5.5(a) plots the error as a function of the number of elements N_E of the mesh. The discretization error decreases with N_E . For a rough mesh, the error is in the same range for the FEM and the hybrid FEM/BEM method. When N_E increases, the error for the FEM/BEM method decreases faster than for the pure FEM approach.

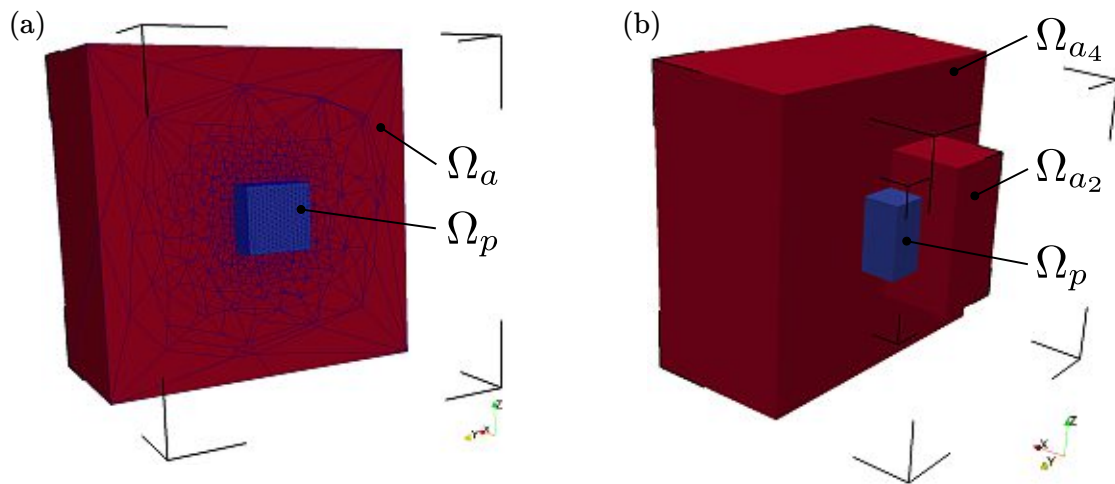


Figure 5.4: Validation of the demagnetization field calculation. (a) Air box Ω_a around a cubic magnet Ω_m . (b) Error estimation of the truncation method with different air box size factors.

On the other hand, the computing time is a crucial factor for the effectiveness of a simulation framework. For this reason, the computation time t for calculation of the demagnetization field is investigated. The setup time for the assembly of the FEM matrices is excluded from the timing. All simulations are carried out at the Vienna Scientific Cluster (VSC-3). It consists of 2020 nodes, each equipped with 2 processors (Intel Xeon E5-2650v2, 2.6 GHz). The computation time t for both methods is shown in figure 5.5(b). The hybrid FEM/BEM method is around 3 times faster than the pure FEM with the truncation method.

The next test validates the general rule of thumb for the truncation method as proposed by Chen [124]. It claims proper simulation results if the outer boundary is located at least 5 times the distance between the most remote outer surface and the center. Start-

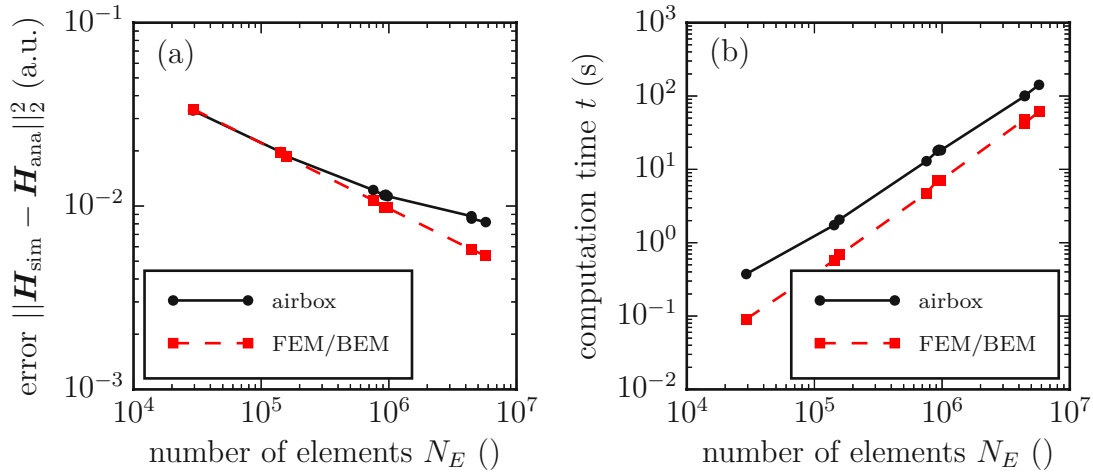


Figure 5.5: Validation of the FEM method for the demagnetization field calculation. (a) The L_2 error-norm between the simulated field H_{sim} and the analytical solution H_{ana} in the permanent magnetic region Ω_p , as a function of the number of elements N_E for the pure FEM implementation and a hybrid FEM/BEM method. (b) Computation time t as a function of the number of elements N_E for both methods.

ing point is the same unit cube as above, but instead of a variable number of elements N_E , the size of the outer air box domain Ω_a is variable by an air box size factor. Figure 5.4(b) illustrates the permanent magnetic region Ω_p with two air boxes with different air box size factors. The same L_2 error-norm 5.20 as above is calculated. Figure 5.6 shows the error as a function of the air box size factor for three different maximum sizes of the tetrahedral elements. The error decreases until the air box is 5 times larger than the magnetic region. This small numerical experiment confirms the general rule of thumb that a 5 times larger air region is sufficient.

Last tests show the effectiveness of the implemented FEM routine for the calculation of an ideal permanent magnet. To validate the simulation capabilities of a non-ideal permanent magnet with soft magnetic domains, a more sophisticated example is presented. A permanent magnetic yoke, as pictured in figure 5.7(a) is simulated with the demagnetization field calculation implemented in FEniCS and the commercial software Comsol Multiphysics 5.2. It consists of a permanent magnetic domain Ω_p with a recoil permeability $\mu_m = 1.05$ and a remanence $B_r = 1$ T along the z -axis, a soft magnetic region with a relative permeability $\mu_r = 1000$ and an air region of interest (ROI) Ω_f . For the simulation in FEniCS, the yoke is modeled and meshed in Salome, for the

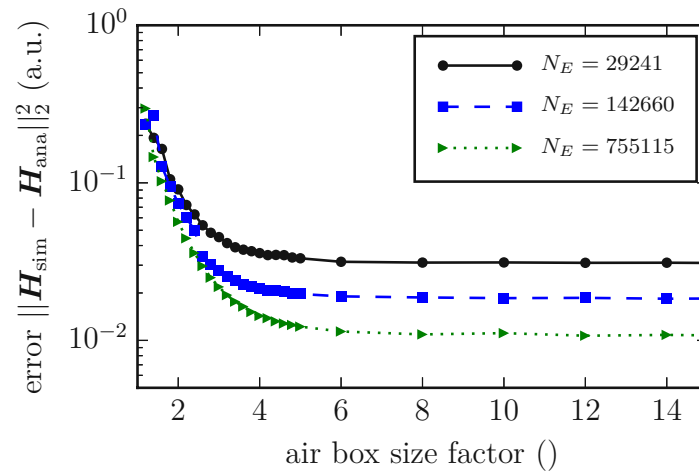


Figure 5.6: Discretization error as a function of the variable air box size factor for different maximum sizes of the tetrahedral elements.

Comsol simulation, the internal modeler and meshing tool is used. Comsol solves the demagnetization field problem with the same truncation approach as discussed above. The air box around the yoke, is 5 times larger as the magnetic domains Ω_p and Ω_s . The vector field of the magnetic field density \mathbf{B} , computed by the implemented FEM method in Ω_p and Ω_s is pictured in figure 5.7(b). Obviously, the presented yoke is not a good design to concentrate the flux in the ROI. In section 5.4.2, an optimized design is presented that maximize \mathbf{B} in Ω_f . However, this test should only compare the two stray-field simulation frameworks. For this reason, a line scan of \mathbf{B} in the middle of Ω_f , simulated with both methods, is shown in figure 5.7(c). Note, the magnetic flux density B_z is reduced by a factor of 1000. The absolute error $\Delta\mathbf{B}$ between both methods is plotted in figure 5.7(d).

This section showed the effectiveness of the implemented FEM method to calculate the stray field of permanent and soft magnetic models. Nevertheless, in fact, the presented FEM method, as well as most commercially available FEM tools to calculate the demagnetization field are only a good approximation for anisotropic permanent magnets. Isotropic magnetic materials have no distinguished magnetization direction. Rather the magnetization is influenced by the demagnetization field. For a proper description of such isotropic materials, a complete characterization of the material, as well as non-linear simulation tools are required. Another approach takes the simulation of

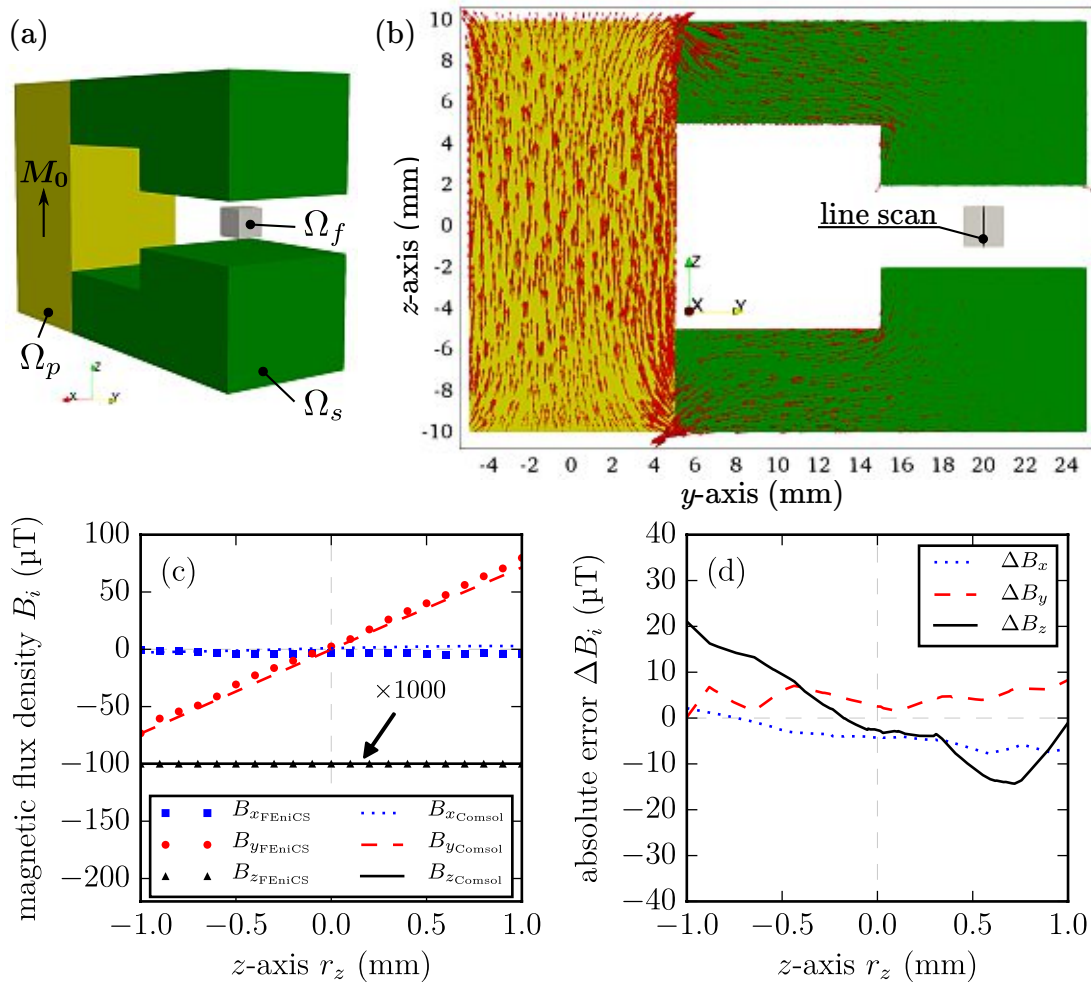


Figure 5.7: Comparison of the stray field between the implemented FEM method with Comsol Multiphysics. (a) Simulation model consists of the permanent magnetic region Ω_p , the soft magnetic domain Ω_s , and the air region of interest (ROI) Ω_f . (b) Vector field of the magnetic field density B , computed by the implemented FEM method in Ω_p and Ω_s . (c) Line scan of B , simulated with both methods. (d) Absolute error ΔB between both methods.

macroscopic isotropic permanent magnets by a freezing field [125]. However, the implemented FEM method of this work do not account for magnetization changes due to demagnetization fields, since it was shown in [125] that this effect is negligible for our application.

5.3 Inverse Stray Field Simulation

The idea behind the presented simulation tool is the possibility to compute the magnetic field distribution of 3D printed structures. The simulation framework that is presented in this section, goes beyond this magnetostatic forward problem. To find structures that create a tailored magnetic field distribution in a defined area, the so-called inverse stray-field problem must be solved. The inherent difficulty of this inverse problem is due to the facts that (i) the inverse problem is not unique and (ii) the underlying system of equations is ill-conditioned.

The generated stray field of a given magnetic system can be designed with different methods. Examples are an inverse magnetic field computation based on a FEM method where the magnetization M of a defined structure is optimized [97, 126]. Shape optimization improves existing designs for better performance [127]. The reciprocity theorem can be employed to calculate the optimal remanent flux density of a permanent magnet system [128]. Parameter variation simulations can be used to find an optimal layout of predefined magnetic structures [129, 130].

Based on the demagnetization-field implementation in FEniCS, an adjoint variable method (AVM) is used to solve the inverse stray-field problem. The AVM method is implemented with the library Dolfin-Adjoint for the automatic derivation of the adjoint equation of a given forward problem [131]. Dolfin-adjoint is a framework for the solution of partial differential equation constraint optimization problems.

5.3.1 Adjoint Variable Method

The inverse problem can be solved by the adjoint variable method (AVM) [132]. It is a well-known method for sensitivity analysis using FEM. Many different applications, ranging from sensitivity analysis in mechanical [133] or electromagnetic systems [134] to topology optimization are based on this method. The main advantage of this method

is the low computational and storage costs compared to other techniques [135].

For the optimization, we consider a general objective function J that should be minimized

$$\min_M J(\mathbf{M}, \mathbf{H}) \quad (5.21)$$

for the inverse stray-field computation, the optimization parameter is the magnetization M . Additionally, control constraints can be applied

$$M_{\min} \leq M \leq M_{\max} \quad \text{for } \mathbf{r} \in \Omega_p. \quad (5.22)$$

For the sensitivity analysis, it is necessary to calculate the functional gradient dJ/dM . The starting point for the AVM is the linear system of equations 5.17

$$\mathbf{A} \cdot \mathbf{u} = \mathbf{b} \quad (5.23)$$

where \mathbf{A} is the symmetric sparse FE matrix whose entities are independent of \mathbf{u} . The derivative of the linear system 5.23 with respect to the design variable M is

$$\mathbf{A} \frac{\partial \mathbf{u}}{\partial M} + \frac{\partial \mathbf{A}}{\partial M} \mathbf{u} = \frac{\partial \mathbf{b}}{\partial M} \quad (5.24)$$

$$\Rightarrow \mathbf{A} \frac{\partial \mathbf{u}}{\partial M} = -\frac{\partial \mathbf{A}}{\partial M} \mathbf{u} + \frac{\partial \mathbf{b}}{\partial M}. \quad (5.25)$$

The direct method calculates $d\mathbf{u}/dM$ directly by equation 5.25 and use this solution for the calculation of the gradients of J . On the other hand, the AVM method uses the adjoint variable λ to solve the problem. The adjoint equation of the system can be defined as

$$\mathbf{A} \lambda = \frac{\partial J}{\partial \mathbf{u}}, \quad (5.26)$$

Multiply λ on both sides of 5.25

$$\lambda \mathbf{A} \frac{\partial \mathbf{u}}{\partial M} = -\lambda \frac{\partial \mathbf{A}}{\partial M} \mathbf{u} + \lambda \frac{\partial \mathbf{b}}{\partial M}. \quad (5.27)$$

Transpose the equation and use the adjoint equation of the system

$$\frac{\partial J}{\partial M} = -\mathbf{u}^T \frac{\partial \mathbf{A}}{\partial M} \lambda + \frac{\partial \mathbf{b}^T}{\partial M} \lambda. \quad (5.28)$$

The computation of the functional gradient dJ/dM can be easily obtained by solving the adjoint equation 5.26. Solving this adjoint system is efficient if there is a small

number of functionals but a large number of parameters. Therefore, this method fits perfectly for the FEM method, where only one functional is of interest, but many elements as input parameter are available. The algorithm can be sketches as pictured in figure 5.8.

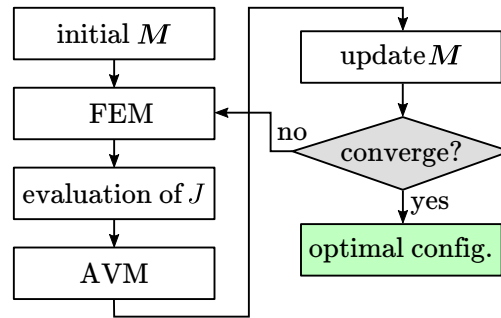


Figure 5.8: Optimization procedure by the adjoint variable method (AVM).

As mentioned above, the inverse problem is ill-posed. To provide an approximate solution of the inverse problem, additional information is necessary. Different methods exist to find reasonable results [108]. Here, the Tikhonov regularization is implemented in the inverse-stray field computation framework. Solving the minimization problem of the following objective function, results in the unknown magnetization M for each finite element of the model in the region Ω_p

$$J = \int_{\Omega_f} |\mathbf{H}_{\text{sim}} - \mathbf{H}_{\text{exp}}|^2 d\mathbf{r} + \underbrace{\alpha \int_{\Omega_p} |\nabla M|^2 d\mathbf{r}}_{\text{regularization}} \quad (5.29)$$

where \mathbf{H}_{sim} is the stray field calculated by the forward problem in a defined region Ω_f , with the magnetic potential u . \mathbf{H}_{exp} is the measured or target stray field in the same region Ω_f . $\alpha \geq 0$ is the Tikhonov regularization parameter. In this case, α has unit m^2 . Usually, a smooth magnetization distribution is desired, this leads to a minimization of ∇M in Ω_p . The inverse problem is solved by means of a continuum approach. This being said, no individual particles are considered, but instead, the particle density is approximated by a continuous density field. As a consequence, there is no general restriction on the mesh size in order to retrieve reasonable results. We discretize all fields (\mathbf{H}_{sim} , \mathbf{H}_{exp} , M) with piecewise affine, globally continuous functions and apply the truncation method for the forward problem and the adjoint problem.

The main challenge for this regularization is the proper choice of a suitable parameter α . If α is too small, the solution will be dominated by the contributions from the data errors. If α is too large, the solution is a poor approximation of the original problem. A well-known method to find an optimal α , is the so-called L-curve method [136]. For this method, the solution norm $\|\nabla M\|_2^2$ is plotted over the residual norm $\|\mathbf{H}_{\text{sim}} - \mathbf{H}_{\text{exp}}\|_2^2$ in a log-log scale for varying $\alpha \in [0, \infty)$. The optimal residual parameter α is where the curve has the maximum curvature (corner of the L-curve). This α value gives a good compromise between the change of the residual norm and the reduction of the solution norm.

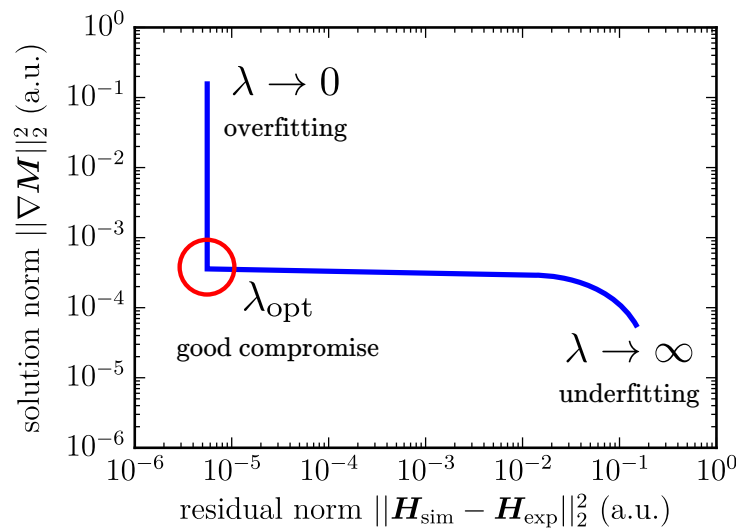


Figure 5.9: Theoretical L-curve to determine the best choice for the regularization parameter α . At the corner the curvature of the L-curve is maximal, which identifies the best compromise between noise in the residual norm and a poor approximation of the original problem.

5.3.2 Implementation in FEniCS & Dolfin-Adjoint

To solve the inverse stray field simulation with the AVM method, the well-suited Dolfin-Adjoint library is used [131, 137]. Dolfin-adjoint contains a framework to solve PDE constraint optimization problems. It automatically derives the discrete adjoint and tangent linear models from a forward model implemented in FEniCS and DOLFIN, respectively. Listing 5.2 shows the implementation of the minimization problem of equation 5.29 in FEniCS and Dolfin-Adjoint.

To solve the minimization problem in equation 5.29, the quasi-Newton L-BFGS-B

optimization algorithm, as well as the IPOPT software library for large-scale nonlinear optimization systems are used [138, 139]. These two algorithms allow bounds for the design parameters.

Listing 5.2: Implementation of the inverse stray field problem in FEniCS and Dolfin-Adjoint

```

1 # Set up forward solution with an initial magnetization
2
3 # Functional
4 J = Functional((inner(H_sim-H_exp, H_sim-H_exp))*dx(2) # field box
5               + alpha*inner(nabla_grad(M), nabla_grad(M))*dx(1)) # magnet
6
7 # Design parameter --> magnetization
8 control = Control(M)
9
10 # Set up minimization problem
11 rf = ReducedFunctional(J, control)
12 problem = MinimizationProblem(rf)
13
14 # Find the optimal magnetization
15 M_opt = minimize(rf, method="L-BFGS-B",
16                 bounds=M_min_max, options={"gtol": 1e-6})

```

5.3.3 Validation and Numerical Experiments

The performance of the implemented inverse stray-field computation is validated by a permanent magnetic unit cube Ω_p with a flower-state magnetization M . The stray field calculation is a scale-invariant problem, therefore length units are irrelevant for the result. The generated stray field of the magnet is measured in six field domains Ω_f with a thickness of 0.2 and an air-gap of 0.1 around the magnet. Figure 5.10(a) shows the magnetic and the field box volume of the problem definition. The flower-state magnetization in Ω_p is parameterized by

$$\mathbf{M} = \begin{pmatrix} \sin(c_{\text{tilt}}\theta) \cos(\phi) \\ \sin(c_{\text{tilt}}\theta) \sin(\phi) \\ \cos(c_{\text{tilt}}\theta) \end{pmatrix}, \quad \begin{aligned} \theta &= z\sqrt{x^2 + y^2} \\ \phi &= \arctan(y/x) \end{aligned} \quad (5.30)$$

where c_{tilt} is a parameter to change the tilt of the magnetization vectors. To simulate measurement errors, Gaussian noise with zero mean and a standard deviation σ

is added to the calculated field of the forward problem. All simulations are performed with a tilt parameter of $c_{\text{tilt}} = 2$, three different standard deviations $\sigma = 10^{-9}, 10^{-3}, 10^{-2}$, and various regularization parameters α to find the optimal parameter α_{opt} .

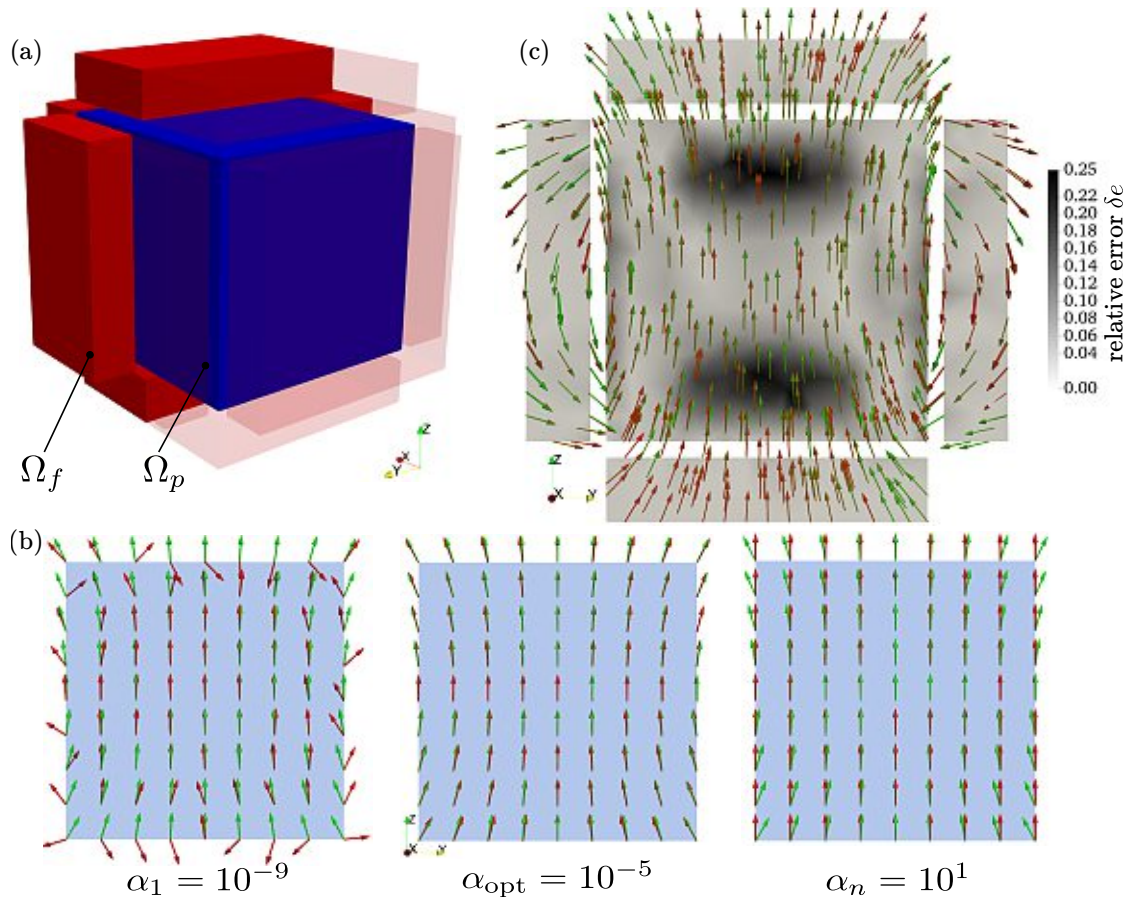


Figure 5.10: Geometric definitions of the problem, and the reconstructed magnetization. (a) Magnetic domain Ω_p as a unit cube with six field boxes Ω_f around the magnet. (b) Cut through the xy -plane of the magnetic domain Ω_p with the reconstructed magnetization M for three different regularization parameters α . (c) Cut through the xy -plane with the flower state magnetization of the forward problem and the stray field density (green vectors). Reconstructed magnetization and the generated field with an optimal regularization parameter $\alpha_{\text{opt}} = 10^{-5}$ (red vectors). The relative error between M of the forward problem and the reconstructed magnetization is visualized by the gray scale.

Figure 5.10(b) shows the magnetization M of the unit cube for three different regularization parameters α . As expected, without a regularization or with a small parameter α , the magnetization has an unphysical distribution, it is over-fitted. By increasing α , the magnetization is more smooth and is nearly the magnetization of the forward

problem (equation 5.30). If α is too large, the magnetization is equal to one and is therefore a poor approximation of the original problem.

A cut through the xy -plane of the optimal reconstructed magnetization ($\alpha_{\text{opt}} = 10^{-5}$) for $\sigma = 10^{-2}$ is shown in figure 5.10(c). The flower state magnetization of the forward problem and the stray field-density (green vectors) fits well with the reconstructed magnetization and stray field in the field boxes (red vectors). The relative error between M of the forward problem and the reconstructed magnetization is visualized by the gray scale. Inside the magnetic domain Ω_p , the error is smaller than 0.25, for the field boxes Ω_f , the relative error is below 0.1.

To find the optimal regularization parameter α_{opt} , the L-curve method, as described above, is used. Figure 5.11(a) shows the L-curve for the various standard deviations of the noise as well as for different minimizers. The optimal parameter for $\sigma = 10^{-2}$ is $\alpha_{\text{opt}} = 10^{-5}$. Both L-BFGS-B and IPOPT minimizer show a similar performance. For $\sigma = 10^{-2}$ and $\sigma = 10^{-3}$ both methods converges at around 20 iterations, and for $\sigma = 10^{-9}$ at around 50 iterations (figure 5.11(b)). With this numerical experiment, the effectiveness of the inverse-stray field computation framework is shown.

5.4 Topology Optimization

The main disadvantage for the generation of a tailored magnetic field with above method is the fact, that an initial geometry of the magnet is required. In contrast, topology optimization allows the designer of magnetic systems to find a suitable topology of the magnets from scratch. Topology optimization was initiated by mechanical and structural engineers [132, 140]. Nowadays, it is a well-established method for magnetic field problems. Possible applications include optimization of write heads of hard disks [141], optimization of magnetostrictive sensor applications [142], designing of C-core actuators [143], and optimization of rotors of brushless DC motors [144].

5.4.1 Methodology

In this work, the density method (also known as solid isotropic microstructure with penalization (SIMP)) is used to solve the topology-optimization problems. This method considers the density ρ of the material in each element, which ranges from 0 (void) to 1

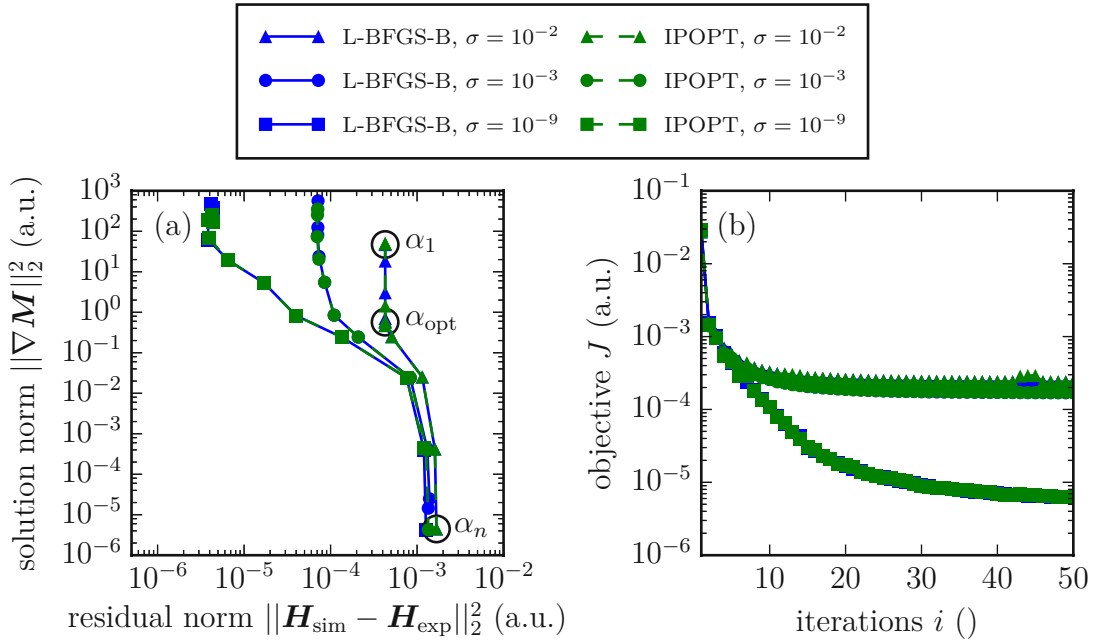


Figure 5.11: Comparison of different solvers to reconstruct the flower state magnetization M for different standard deviations σ of the noise. (a) L-curves to find the optimal regularization parameter α_{opt} . (b) Value of the objective function J as a function of the solver iterations i .

(bulk). This leads to one optimization variable per element. Intermediate densities are penalized in this approach, which means that the density of the final design should be only 0 or 1 [132]. For permanent magnetic systems, the magnetization of an element in the design domain $\Omega_p \in \mathbb{R}^3$ can be formulated for the design method as

$$M(\varrho) = \varrho^k M_0 \quad (5.31)$$

where $\varrho \in [0, 1]$ is the density value of a FEM element, $k = 1$ is the penalization parameter [142], and M_0 is the magnetization vector. For soft magnetic materials, the relative permeability μ_r in the design domain $\Omega_s \in \mathbb{R}^3$ can be reformulated for the design method to

$$\mu_r(\varrho) = (\mu_{r0} - 1)\varrho^k + 1 \quad (5.32)$$

for topology optimization of soft magnetic materials, a penalization parameter of $k = 4$ leads to good results.

The general topology-optimization problem with the density method can be formulated as

$$\begin{aligned} \text{Find: } & \min_{\varrho} J(\varrho) \\ \text{subject to: } & \int_{\Omega_i} \varrho(\mathbf{r}) d\mathbf{r} \leq V; \\ & 0 \leq \varrho(\mathbf{r}) \leq 1, \mathbf{r} \in \Omega_i \end{aligned} \quad (5.33)$$

with the objective function J and the maximum Volume V of the design as a constraint, $i \in \{p, s\}$ defines the permanent and soft magnetic domain, respectively. The only difference in the implementation between the inverse stray-field computation, as described above, and the topology optimization presented here is the optimization variable. For topology optimization, the design variable is the density ϱ and not the magnetization vector M .

5.4.2 Validation and Numerical Experiments

To proof the effectiveness of our topology-optimization framework, the magnetic field B_z in a small target volume Ω_f should be maximized and compared with a theoretical consideration (figure 5.12(a)). The design domain Ω_p has the dimension $R = 10$ mm, $h = 7$ mm, and the target domain is a cube with the side length $a = 0.1$ mm, 0.1 mm above the design domain. To maximize B_z at Ω_f , the objective function has the following form:

$$J(\varrho) = \int_{\Omega_f} \frac{1}{|H_z(\varrho)|^2} d\mathbf{r} \quad (5.34)$$

with the magnetic field $H_z(\varrho)$. The result of the topology optimization is a conical permanent magnet with a cone angle of $\alpha \approx 35.2^\circ$.

The theoretical geometry of a magnet that creates a maximum field in a point above the magnet can be simply considered by magnetic dipoles $\boldsymbol{\mu}$ in a given design area Ω_p (figure 5.12(b)). The magnetic flux density \mathbf{B} of a magnetic dipole is [34]

$$\mathbf{B}(\mathbf{r}) = \frac{\mu_0 \boldsymbol{\mu}}{4\pi r^2} \frac{3\mathbf{r}(\boldsymbol{\mu} \cdot \mathbf{r}) - \boldsymbol{\mu} r^2}{r^3}, \quad (5.35)$$

with the vacuum permeability μ_0 and the distance \mathbf{r} to the dipole. Consider B_z in the xz -plane, and for $\boldsymbol{\mu} \parallel \mathbf{e}_z$:

$$B_z(\mathbf{r}) = \frac{\mu_0 \mu}{4\pi r^2} \underbrace{\left(\frac{3z^2 - r^2}{r^3} \right)}_{\gamma > 0}. \quad (5.36)$$

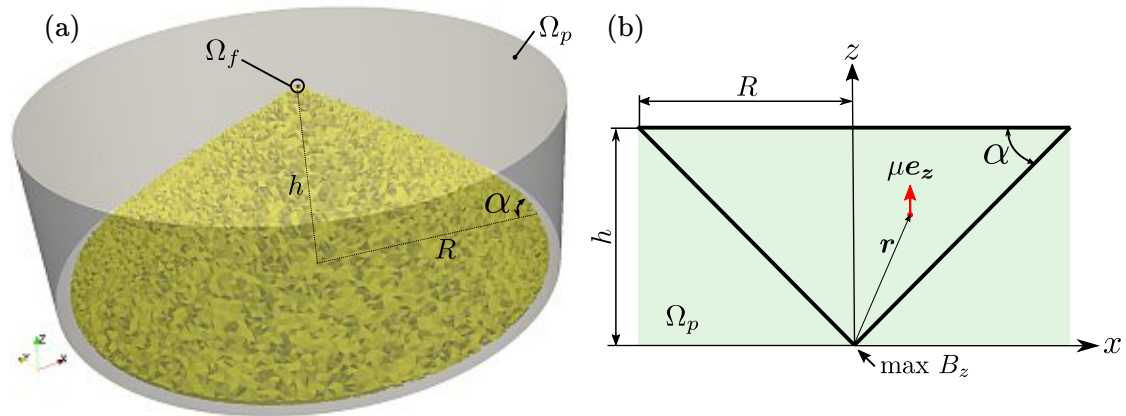


Figure 5.12: Validation of the topology optimization framework. (a) Maximize B_z in the region Ω_f above the design volume Ω_p . The resulting cone has the same angle $\alpha \approx 35.2^\circ$ as theoretically predicted. (b) Sketch for the calculation of the optimal angle α of a conical permanent magnet.

The field component B_z of a dipole is positive for $\gamma > 0$, and negative for $\gamma < 0$. Therefore, the dipoles must be positioned at all locations where this relation is fulfilled. This will lead to a maximum field component B_z . For the surface condition $\gamma = 0$, following relation holds:

$$z = \pm \frac{x}{\sqrt{2}}, \text{ or:} \quad (5.37)$$

$$\tan \alpha = \frac{1}{\sqrt{2}}.$$

Hence, the optimal shape is a cone with an angle $\alpha \approx 35.26^\circ$. This calculation confirms the result of the numerical topology optimization.

Next, the same problem as above is considered, but with a cubic design domain Ω_p with a side length $a = 10$ mm, and a hard volume constraint. The magnetic field B_z in Ω_f is simulated for different volume fractions V/V_{\max} . Figure 5.13(a) shows the geometry and the solution for two different volume fractions (40 %: blue, 100 %: yellow). In figure 5.13(b), B_z is plotted in relation of the volume fraction $V/V_{\max} \in [1, 100]$ %.

It is found, that with only 40 % of magnetic material, 94 % of the maximum B_z is attainable. These examples show that topology optimization can be used to find the topology of a permanent magnet for a given target field. Furthermore, this method can be used to reduce the amount of applied magnetic material.

As last example, the soft magnetic yoke from section 5.2.4 (figure 5.7) should be op-

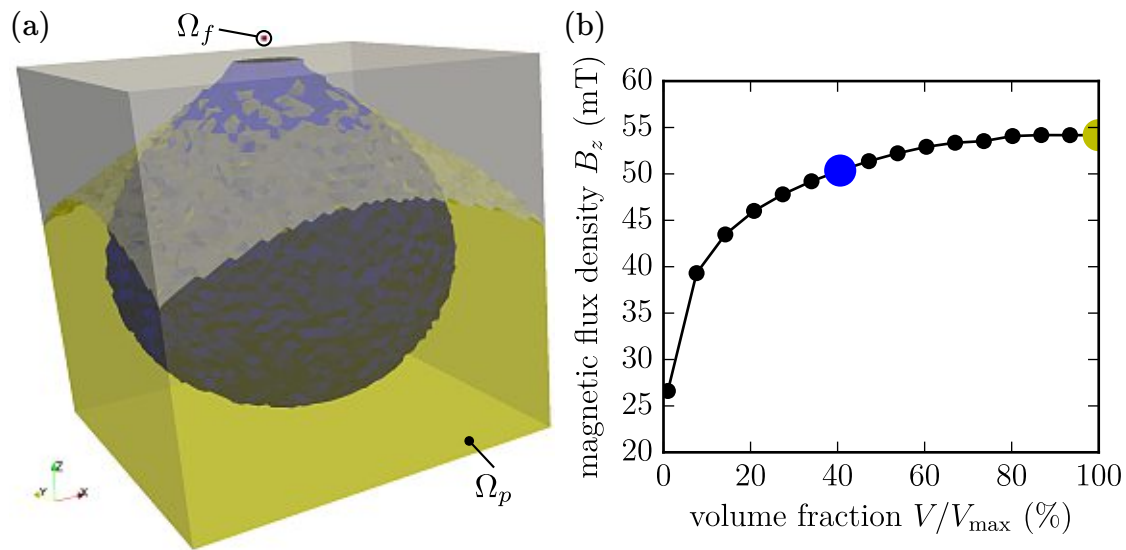


Figure 5.13: Maximize B_z with different volume constraints of the design volume Ω_p . (a) Topology of two different volume constraints (40 %: blue, 100 %: yellow). (b) Maximum B_z with different volume constraints.

timized in order to maximize the magnetic field in the field box Ω_f . The design domain is divided into a two parts. The first domain is the former permanent magnetic domain Ω_p . Now, each element of the design domain can consist of either permanent or soft magnetic material. The second, former soft magnetic Ω_s domain, can be either soft or non-magnetic. The relative permeability μ_r , recoil permeability μ_m and the magnetization M_0 are unchanged compared to the former example.

Figure 5.14(a) shows the result of the topology optimization for the given problem. The vector-field distribution of the magnetic field density \mathbf{B} is pictured in figure 5.14(b). Compared to the initial design in figure 5.7(b), a much smoother transition of \mathbf{B} between permanent and soft magnetic material can be observed, as well as the soft magnetic yokes are optimized in order to form a flux concentrator. A line scan through Ω_f of the initial and the optimized design can be seen in figure 5.7(c). The optimized design generates more than double the maximum field in the middle of the field box.

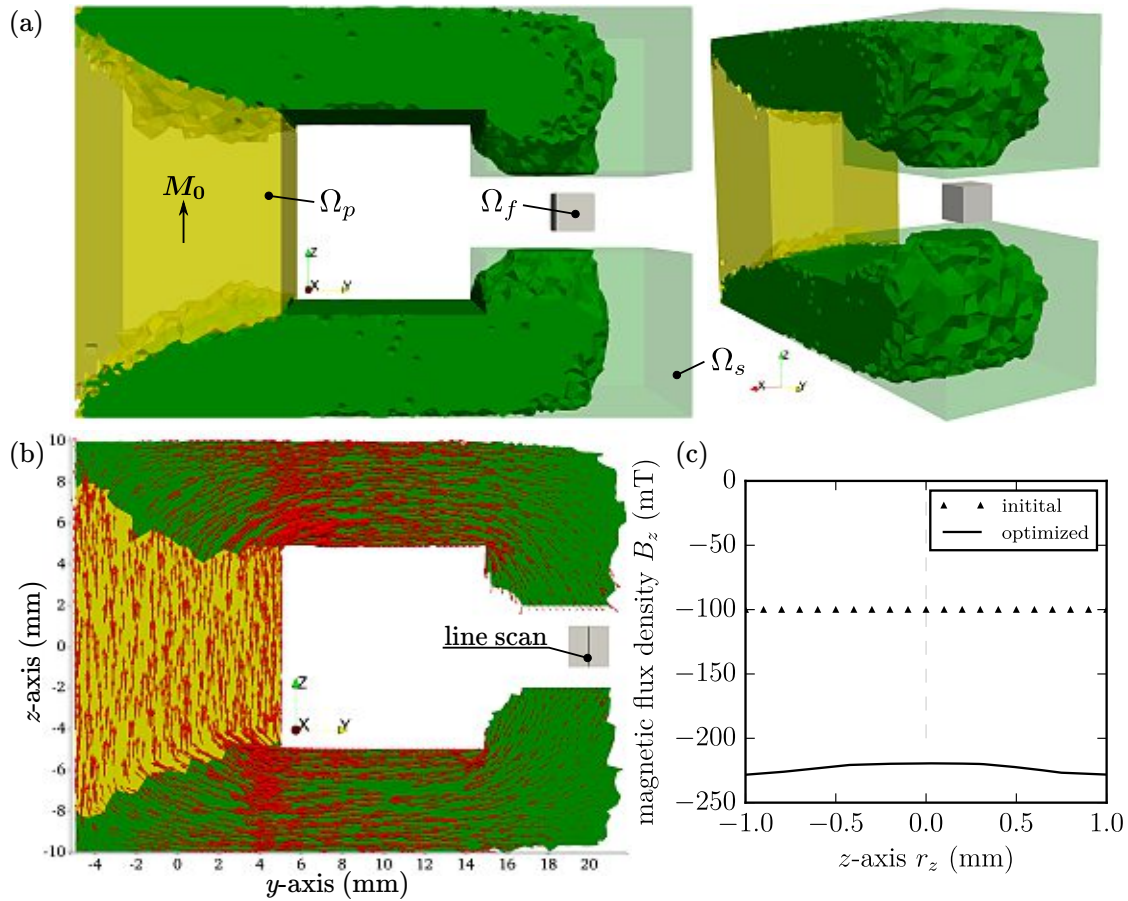


Figure 5.14: Topology optimization of a permanent and soft magnetic combined yoke. (a) Optimization of the topology to maximize the field in the field box Ω_f , permanent magnetic material in yellow, soft magnetic material in green (outer box is the initial topology). (b) Vector field of the magnetic field density B , in Ω_p and Ω_s . (c) Line scan through Ω_f compared with the initial design and the optimized topology.

6 Applications

Portions of this chapter were previously published in [82, 97, 98] and have been reproduced with permissions of the coauthors and in accordance with the publisher's policy. Content which was not generated by the author of this thesis is explicitly denoted, copyright is held by American Institute of Physics and Nature Publishing Group.

6.1 Introduction

The last chapters gave an overview about AM methods in general and a detailed description of our setup. Production of magnetic compound materials are described, as well as characterized. Simulation and design tools, to find a magnetic design that generate a specific stray field distribution are presented. Now, it is time to combine and apply all presented methods to 3D print polymer-bonded magnets for a tailored magnetic field. Several "real-world" problems are presented that underline the effectiveness of the 3D printing method.

6.2 Magnetic Speed Wheel Sensing

The first application deals with a magnetic speed wheel sensing system. Such high precision sensor systems are embedded in many applications, especially in automotive application, e.g. in anti-blocking system (ABS) or engine management systems [50]. A possible design of such speed sensors consist of a magnetic field sensor, e.g. Hall effect or giant magnetoresistance (GMR) sensor, a permanent magnet which provide a bias field, and a soft magnetic wheel. Normally, the magnet is underneath the sensor (back-bias magnet) and the rotating wheel modulates the magnetic field of the back-bias magnet. The rotational velocity of the wheel is direct proportional to the modulation of

the field. Figure 6.1(a) shows a sketch of a possible wheel speed sensing arrangement.

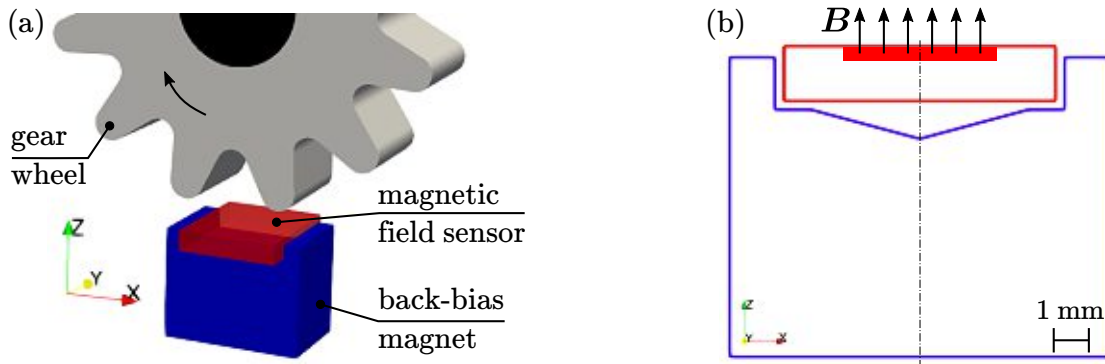


Figure 6.1: Magnetic wheel speed sensing. (a) Principle of the magnetic speed sensing. A permanent magnet is underneath the magnetic field sensor (back-bias magnet). A soft magnetic gear periodically modulates the bias field of the magnet. (b) Special back-bias magnet for giant magnetoresistance (GMR) sensors.

A possible assembling method is to overmold the sensor by polymer-bonded magnetic material by IM [50]. This application shows the full potential of polymer-bonded magnets, an accurate field distribution is, in some cases, more important than a maximum field. If a GMR sensor is designated to detect the field modulation, some special magnetic design criteria must be considered. GMR sensors are in-plane sensitive and the linear range is very small [87]. This means that the back-bias magnet must have very low magnetic in-plane field components. This can be achieved by a specific design of the magnet. Figure 6.1(b) shows the cross-section of a well-known geometry that minimizes the components of the magnetic stray field B in x and y direction in a wide range along the x -axis r_x . This complex design can be easily manufactured by IM, but up-to-now, no single-unit production process is available for prototyping of such magnets.

6.2.1 3D Printed Back-Bias Magnet

Outgoing from the design as described above, a back-bias magnet for speed wheel sensing is 3D printed with Neofer[®] 25/60p. The overall size of the magnet is $7 \times 5 \times 5.5 \text{ mm}^3$ ($L \times W \times H$) with a layer height of 0.1 mm and features with a thickness of 0.8 mm. After the printing process, the magnet is magnetized in an electromagnet as described in section 3.4. An area scan above the magnet as pictured in figure 6.2(a) is performed. Figure 6.2(b) shows a line scan and FEM simulation results 2.5 mm above the pyramid

tip (T). Comparison points out a good conformity between simulation and measurement. A picture of the printed magnet is illustrated in figure 6.2(c).

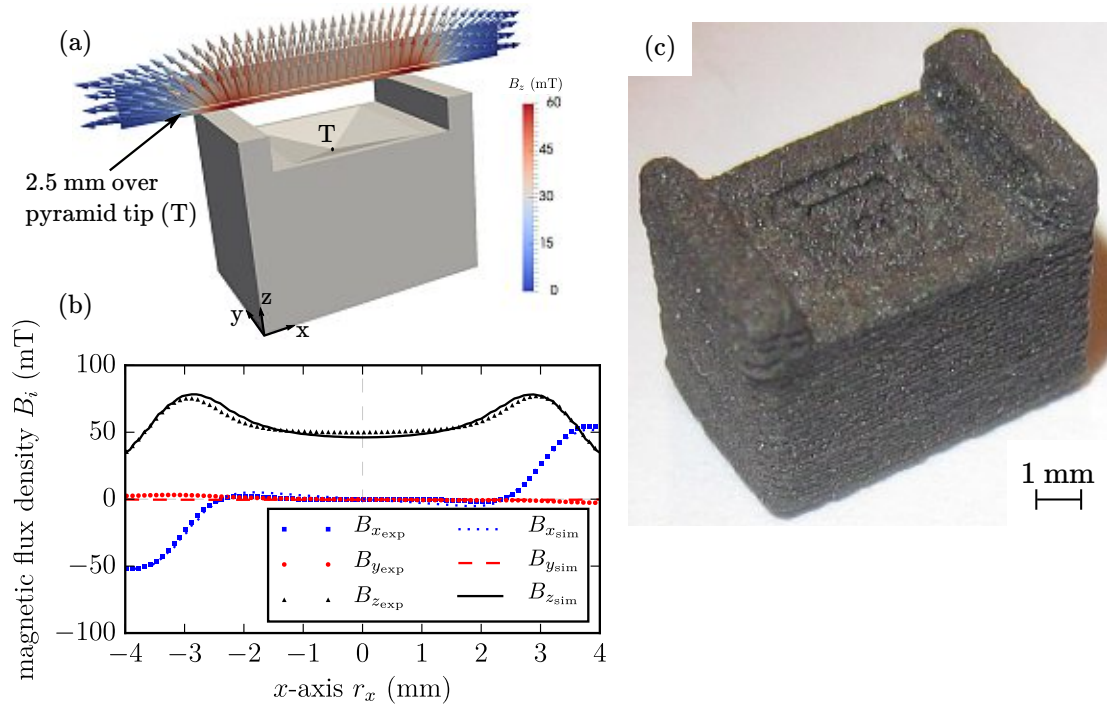


Figure 6.2: 3D printed back bias magnet for magnetic speed sensing applications. (a) Geometry of the back-bias magnet, and area scan of \mathbf{B} with a step size of 0.1 mm in the middle of the printed magnet. (b) Line scan 2.5 mm over pyramid tip (T) compared with FEM simulations of the back-bias magnet with perfect shape. (c) Printed isotropic NdFeB magnet with Neofer® 25/60p with optimized shape to suppress B_x and B_y along the x -axis r_x .

6.2.2 Reconstructed Topology

As described in section 5.4, topology optimization is a well-known method to design permanent magnets. This section shows a method for the reverse engineering of permanent magnets. This means, that the unknown geometry of a permanent magnetic system can be reconstructed from field measurements. The objective function for the minimization problem in equation. 5.33 can be written as

$$J(\varrho) = \int_{\Omega_f} |\mathbf{H}_{\text{sim}}(\varrho) - \mathbf{H}_{\text{exp}}|^2 d\mathbf{r} \quad (6.1)$$

where $\mathbf{H}_{\text{sim}}(\varrho)$ is the the simulated field and \mathbf{H}_{exp} is the measured external field outside the magnet.

The former printed back-bias magnet with these special characteristics is scanned with the 3D Hall sensor in a target field volume Ω_f of size $10 \times 10 \times 2 \text{ mm}^3$ ($L \times W \times H$), 0.5 mm above and under the magnet, with a resolution of 0.2 mm (figure 6.3(a)). Figure 6.3(b) shows the design domain Ω_p with the dimension $7 \times 4.5 \times 5.5 \text{ mm}^3$ ($L \times W \times H$) and the reconstructed topology of the permanent magnet. The mesh of Ω_p consists of 476, 225 tetrahedral elements. It is found, that the reconstructed geometry has a different shape as the original one. There is no pyramid tip in the middle of the magnet and the bars on the top are not vertical. Interestingly, the volume of the reconstructed, topology optimized structure is around 5 % lower than the volume of the original structure.

The output of the reconstruction is used to generate a model for the 3D printing process. The model is printed with the same printing parameters, and material (Neofer[®] 25/60p) as the original one. Figure 6.3(c) displays a line scan 2.5 mm above the pyramid tip (T). Comparison between the original printed magnet and the reconstructed optimized magnets points out a good agreement. A picture of the printed, reconstructed polymer-bonded magnet is shown in Figure 6.3(d).

6.3 Magnets with a Variable Magnetic Compound Fraction

As described in section 3.1.1, our 3D printer has the possibility to mix two materials during the printing process. It is used to mix magnetic compound filaments (PA12+MQP-S (85 wt.)) with pure commercial PA12 filaments. The magnetic compound fraction and therefore, the remanence B_r is a function of the layer number and building height, respectively.

6.3.1 Reconstructed Magnetization Distribution

To benchmark the variable magnetic compound fraction printing method, a cuboid of size $10 \times 40 \times 10 \text{ mm}^3$ ($L \times W \times H$) with an absolute value magnetic distribution function ($\varrho_m = 100 \% / (W/2) |r_y| \%$) is printed (figure 6.4(a)). The sample is magnetized inside an electromagnet with 1.9 T along the z -axis. A volume scan ($12 \times 40 \times 2 \text{ mm}^3$ ($L \times W \times H$)) with a spatial resolution of 0.2 mm in the magnetization direction r_z) of the produced stray field above and under the magnetized cuboid is pictured in figure. 6.4(b). This

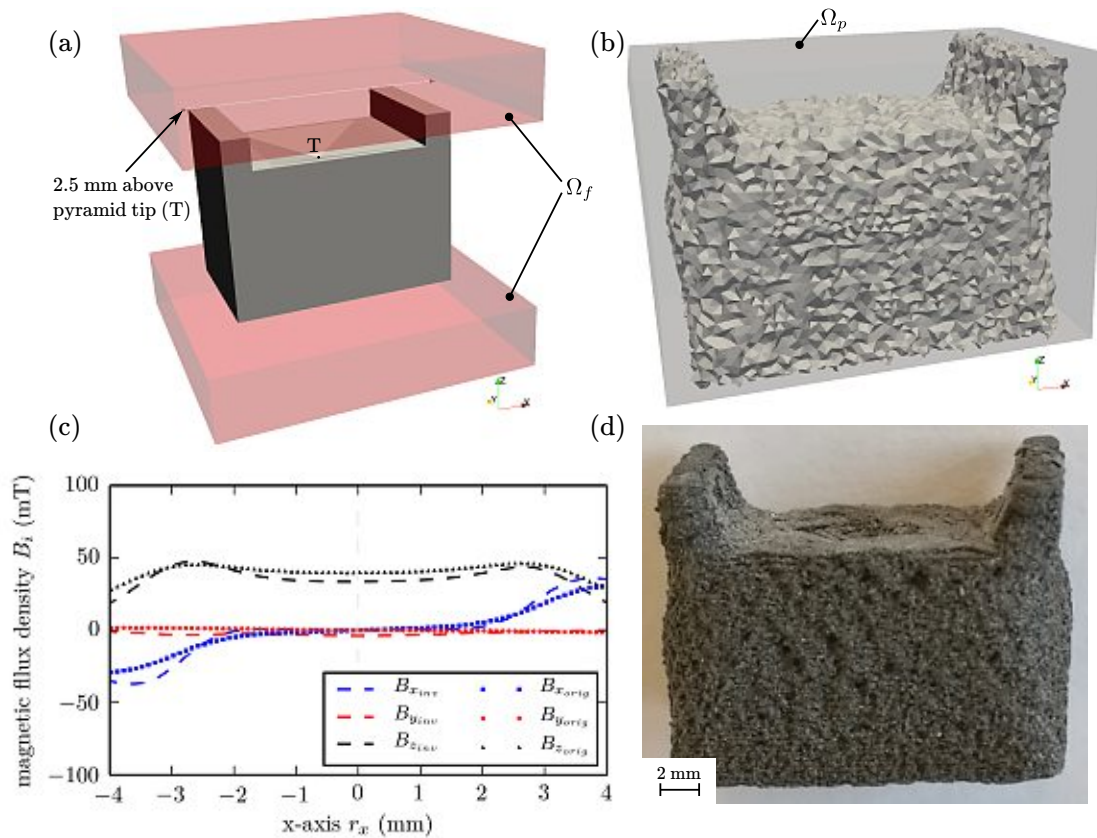


Figure 6.3: Reconstructed topology of the scanned back-bias magnet. (a) Geometry of the back-bias magnet that generates a specific field. The magnetic field of the field boxes Ω_f are scanned and used for the topology optimization. (b) Reconstructed magnet from measurement data. (c) Line scan of the magnetic field 2.5 mm above the original and the reconstructed, printed magnet. (d) Picture of the printed magnet.

measurement will be used to reconstruct the magnetization distribution inside the magnet and therefore, deduct the quality of the printed magnet.

The measured \mathbf{H}_{exp} is the input for the inverse stray field calculation (equation 5.29). The simulation is performed for a range of different Tikhonov regularization parameters $\alpha = 10^x \text{ m}^2$ with $x \in [-9.4, 3]$ and a step size of 0.4. First, the region with the optimal parameter α is limited; then, the maximum curvature in this region is calculated. Figure 6.5(a) shows the L-curve with the different α values, and the optimal solution with $\alpha_{\text{opt}} = 6.4 \times 10^{-3} \text{ m}^2$. The mesh of the simulation consists of 315,941 tetrahedral elements with a mesh size of the magnetic region of 0.25 mm. Figure 6.5(b) illustrates the magnetization distribution M_z , which is proportional to the magnetic

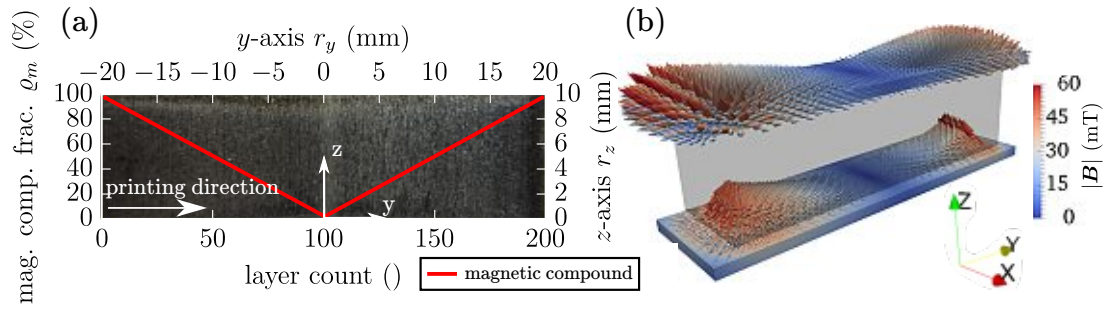


Figure 6.4: 3D print of a polymer-bonded magnet with a variable magnetic compound fraction. (a) Picture of the printed cuboid ($10 \times 40 \times 10 \text{ mm}^3$ ($L \times W \times H$)), and the magnetization distribution along the y -axis r_y . (b) Volume scan of the produced stray field above and under the printed magnet.

compound fraction distribution inside the magnet. The magnetization M_z is a function of r_y as expected, but it also depends on r_z . In our case, only measurements under and above the magnet are used. Therefore, the algorithm cannot reconstruct the ideal distribution, and the print is not perfect. However, the example shows good conformity between experimental and simulation results. A line scan 1.5 mm above the magnet compared with simulation results is shown in figure 6.5(c). It points out a good agreement between measurement and results from the inverse stray field calculation. The magnetization distribution along the y -axis in the middle of the magnet is plotted in figure 6.5(d). The reconstructed magnetization $M_{z_{\text{inv}}}$ fits very well with the ideal magnetization distribution of $M_{\text{ideal}} = M_{\text{max}} / (W/2) |r_y| \text{ mT}$ or $\varrho_m = 100 \% / (W/2) |r_y| \%$ for the magnetic compound fraction distribution, where M_{max} is the maximum magnetization and W is the width of the magnet. The reconstructed components $M_{x_{\text{inv}}}$ and $M_{y_{\text{inv}}}$ are small compared to the z component. This complies with the expectations of the printed permanent magnet.

6.3.2 Tailored Magnetic Stray Field

Instead of using the inverse stray field method to investigate already printed magnets, the method can also be used to design magnets with specific stray field properties. As examples, we compute the optimal magnetization distribution for a hollow cylinder geometry for different target fields inside the cylinder. The hollow cylinders have the dimension in mm $\varnothing 25$, $\varnothing 20$, and 50 (d_{outer} , d_{inner} , L) with a linear and constant stray field distribution inside the hollow magnet. Figure 6.6(a) shows the model of the mag-

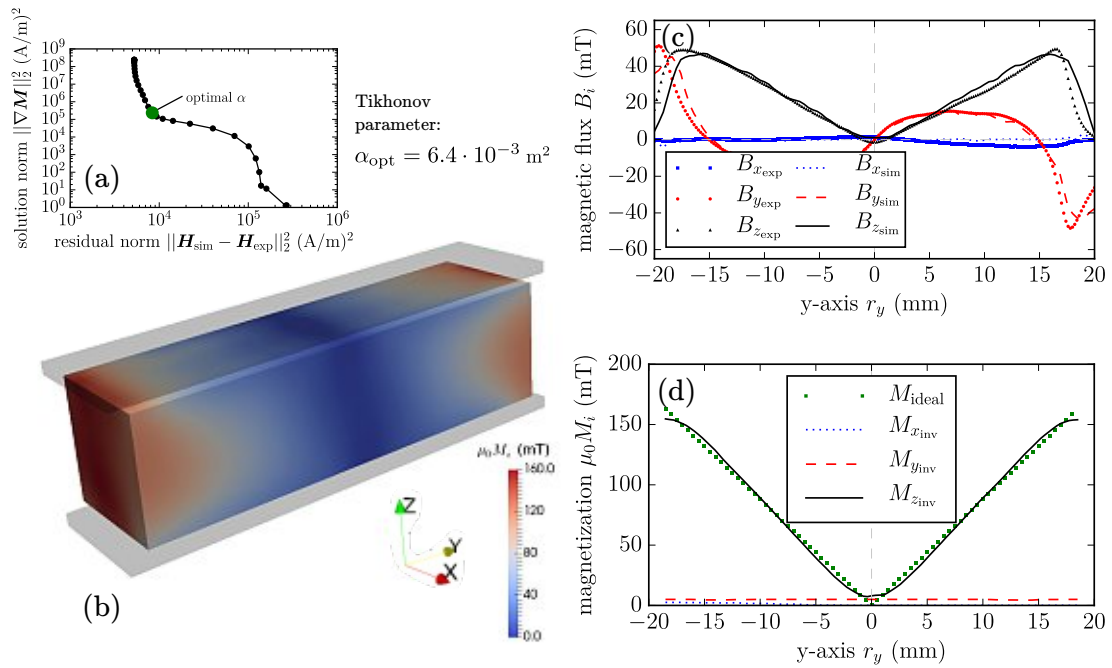


Figure 6.5: Reconstructed magnetization of a cuboid printed structure. (a) L-curve to find the optimal Tikhonov regularization parameter α . (b) Reconstructed magnetization distribution $\mu_0 M_z$ of the magnet. (c) Line scan of the stray field 1.5 mm above the magnet compared with the inverse stray field simulation results. (d) Ideal magnetization in the middle of the magnet along the y -axis r_y compared with the reconstructed magnetization distribution.

net with the magnetic region Ω_p and the region for the predefined stray field Ω_f . The mesh Ω of the simulation consists of 455,306 tetrahedral elements with a mesh size of the magnetic region Ω_p of 0.4 mm. The printing direction is along the z -axis. For this reason, the variable \mathbf{H}_{exp} in equation 5.29 does not represent the measurement data but rather the desired stray field in distributions Ω_f . M_x and M_y are fixed to zero, and the maximum of M_z is limited to the used magnetic material. Otherwise, the real printed magnet cannot reach the desired magnetization. Two different stray field distributions are tested. The first is a constant magnetic flux density of $B_z = 5.5$ mT along the z -axis $r_z \in [10, 40]$ mm; the second one is a linear increasing field of $B_z = 2 + 0.15r_z$ mT/mm along the z -axis $r_z \in [10, 40]$ mm. A constant magnetic field inside a hollow cylinder can be used to calibrate sensors where the sensor position is changing. A linear increasing field can be used to realize a linear positioning system. In this case, a 1D sensor is enough for an accurate position detecting system [129].

The resulting magnetic compound fraction distribution along the z -axis is plotted in figure 6.6(b). Figure 6.6(c) shows the comparison between simulations and measurements in the middle of the hollow cylinders. The inverse stray field simulation for both examples is performed for various Tikhonov regularization parameter $\alpha = 10^x \text{ m}^2$ with $x \in [-10, 1]$. The L-curve for both simulations is presented in figure 6.6(d). α_{opt} is clearly visible and is marked in green ($\alpha_{\text{opt}} = 2.5 \times 10^{-7} \text{ m}^2$ for both designs). Inside the field boxes with the dimensions in mm of $\varnothing 2, 30$ (d, L), a good conformity between printed and simulated magnets is given. A picture of one of the printed magnets is presented in figure 6.6(e).

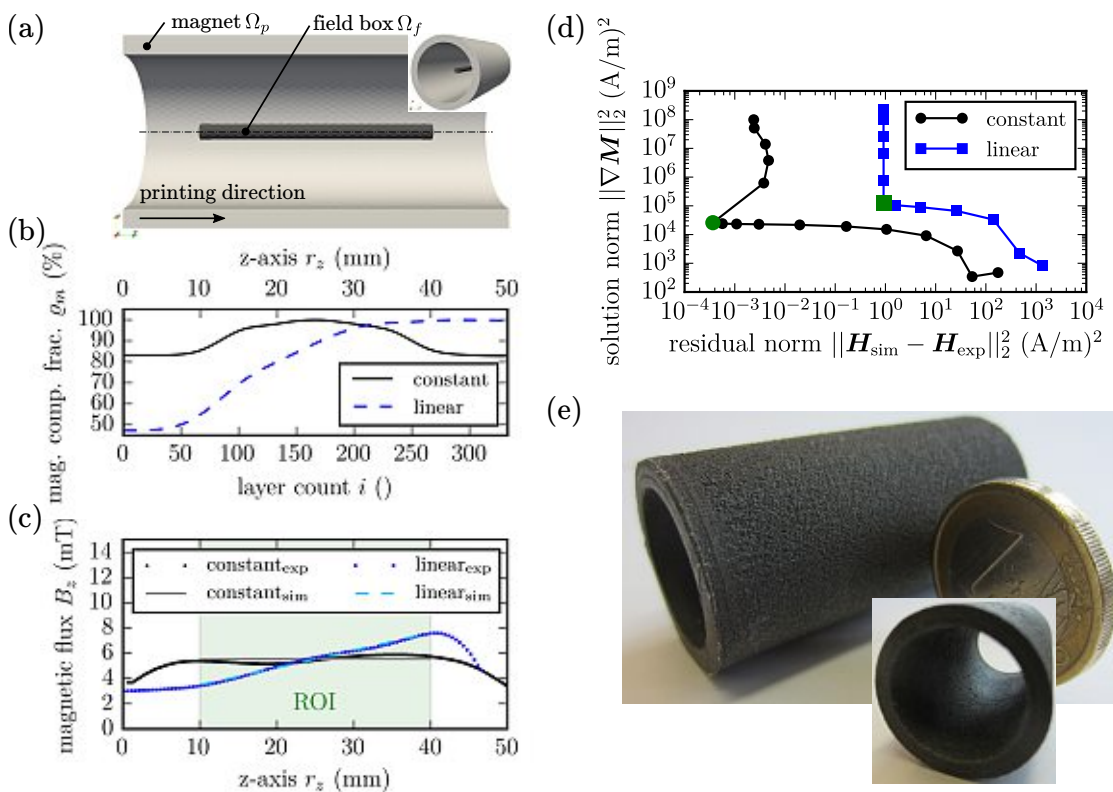


Figure 6.6: 3D prints of magnetic hollow cylinder with a variable magnetic compound fraction distribution to generate a predefined stray field inside the cylinder. (a) Model of the hollow cylinder magnet with the dimension in mm ($\varnothing 25, \varnothing 20, 50$ ($d_{\text{outer}}, d_{\text{inner}}, L$)) with a predefined stray field in the field box ($\varnothing 2, 30$ (d, L)). (b) Magnetic compound fraction distribution ϱ_m along the z -axis r_z to create a constant and linear stray field in the field box, respectively. (c) Stray field measurements of B_z compared with inverse stray field FEM simulations in the middle of the hollow cylinder for the linear and constant field generations magnet, respectively. (d) L-curve for both designs to find the optimal Tikhonov regularization parameter α . (e) Picture of the hollow cylindrical magnet.

The error between measurements and simulations is plotted in figure 6.7(a). The error changes along the z -axis, and it is around 6% for the constant and 4% for the linear design. Another important feature of this magnetic design is the homogeneity of B_z . The homogeneity is defined as $\tau = (B_z(r)/B_z(0) - 1)100\%$. Figure 6.7(b) shows a plot of the homogeneity τ within a radius of $r = 2.5$ mm on three planes ($r_z = 15, 25, 35$ mm) inside the hollow cylinder. The deviation of the homogeneity is lower than 2%.

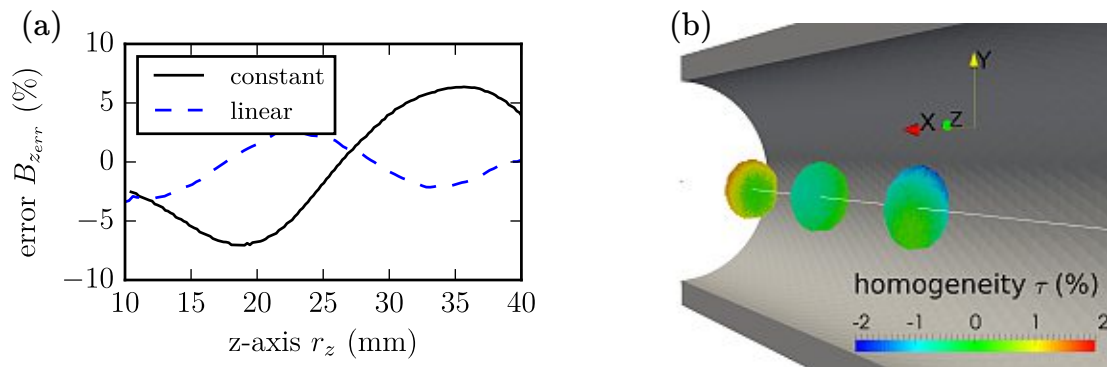


Figure 6.7: Errors of the printed magnets for a predefined stray field. (a) Error between the measured stray field and the inverse stray field simulation along the z -axis r_z for the linear and constant stray field generator magnets. (b) Homogeneity τ within a radius of $r = 2.5$ mm on three planes ($r_z = 15, 25, 35$ mm).

6.4 Linear Position Measurement Setup

Linear position detection systems measure the position of an object in one direction. Magnetic measurement systems have some great advantages compared with other systems such as, it is contact-free, low power, cost effective, and it is miniaturizable [145]. Currently, most magnetic measurement systems measure the field of a magnetic system and convert the sensor output signal to the position of the object. A disadvantage of these systems is, that without an optimization of the bias magnet, the position of an object as a function of the sensor output is highly non-linear. Additionally, during the manufacturing process of such measurement systems, production tolerances are unavoidable. Parameter variation simulations for such systems already exist [129]. These kind of simulations are restricted, because they need an initial layout of the permanent magnetic system.

Here, a polymer-bonded permanent magnetic system should generate a linear field in a wide range above, and along the y -direction of the system. Additionally, the volume should be minimized with a constraint. A model of the system is pictured in figure 6.8. It consist of a predefined not changeable socket. On both sides of the socket a cubic design domain Ω_{p1} and Ω_{p2} for the permanent magnets with a side length of $a = 10$ mm are given. The gap between the two domains is 5 mm. The 3D Hall sensor as described above has a detection volume of $0.22 \times 0.22 \times 0.20$ mm³ ($L \times W \times H$) and it is used for the determination of the position. The target field volume Ω_f has the dimension of $1 \times 5 \times 1$ mm³ ($L \times W \times H$). Therefore, a tolerance of ± 0.78 mm for the sensor position is provided. The target field domain is 1.5 mm above the permanent magnetic setup.

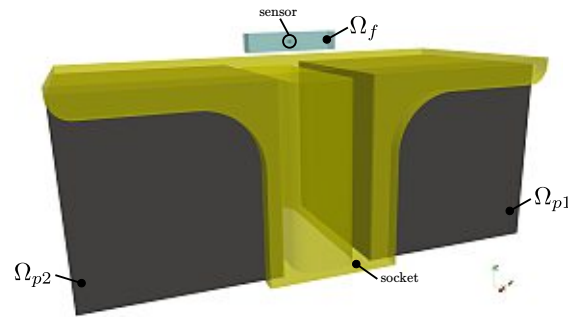


Figure 6.8: Setup of a magnetic configuration to linearize B_z in the region Ω_f .

The bias magnet should generate a target field $H_{z_{\text{theor}}}(r_z) = H_{\text{max}}/W r_y$ with $\mu_0 H_{\text{max}} = 35$ mT. The objective function for the minimization problem in equation 5.33 of this system can be formulated as

$$J(\varrho) = \int_{\Omega_f} |H_{z_{\text{sim}}}(\varrho) - H_{z_{\text{theor}}}(r_z)|^2 d\mathbf{r} \quad (6.2)$$

where $H_{z_{\text{sim}}}(\varrho)$ is the simulated field component in z direction.

The mesh of one design domain consist of 567,888 tetrahedral elements. Simulations are performed with five different volume constraints ($V = 300, 500, 1000, 1500$, and V_{max}) in mm³. To create a linear magnetic field, design domain Ω_{p1} is magnetized in z -direction and Ω_{p2} is magnetized in $-z$ -direction. Figure 6.9(a) shows the magnetic design with the different volume constraints. The field component B_z , 2 mm above the magnetic system for the different volume constraints is plotted in figure 6.9(b), and

the deviation of the simulated field with the theoretical field $B_{z_{\text{theor}}}$ is plotted in figure 6.9(c). The solution without a volume constraint and with a maximum volume of $V = 1500 \text{ mm}^3$ is almost the same. If the maximum applicable volume decrease, the deviation between the target magnetic field $H_{z_{\text{theor}}}$ and the simulated field increase. However, the system can be optimized in both ways. To save volume and costs, or to maximize the linearity of the system. For a good compromise between applied volume and linearity of the system, a value of $V = 1000 \text{ mm}^3$ leads to a maximum deviation of $e = 0.3 \text{ mT}$ regarding $H_{z_{\text{theor}}}$ and a positioning accuracy of $4.2 \text{ }\mu\text{m}$, respectively. For a low-cost system with a volume of only $V = 300 \text{ mm}^3$ the deviation increase to $e = 1 \text{ mT}$ and a positioning accuracy of $142 \text{ }\mu\text{m}$, respectively.

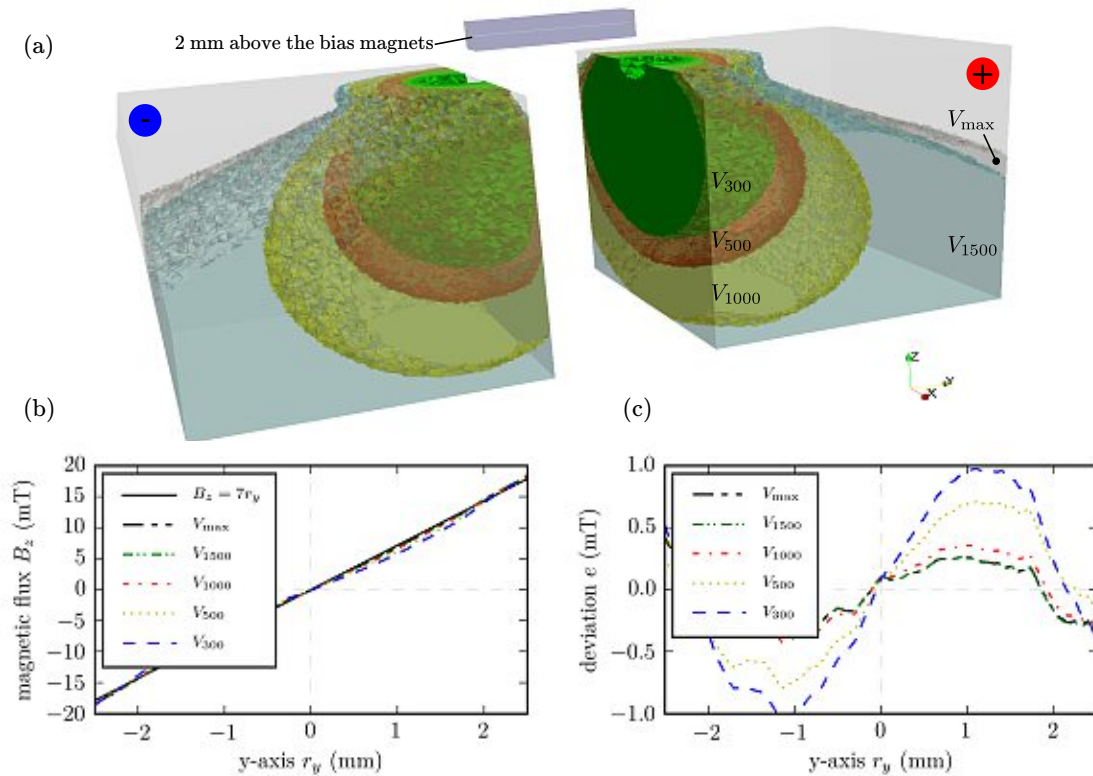


Figure 6.9: Topology optimized magnetic configuration with different volume constraints. (a) Picture of the topology with different volume constraints. (b) Stray field B_z 2 mm above the magnets with different volume constraints. (c) Deviation between simulation and the given linear increasing field.

To verify these simulation results, the magnetic system is printed and the external field is characterized with two different volume constraints ($V = 300 \text{ mm}^3$ and $V =$

1000 mm³). Figure 6.10(a) shows the system for these two volume constraints. The optimized magnets are printed with the same configuration and setup as described above. After the printing process, the magnets are magnetized inside the electromagnet with a maximum magnetic field of 1.9 T. The socket is printed with pure PA12, and the system is assembled with the two magnetized magnets.

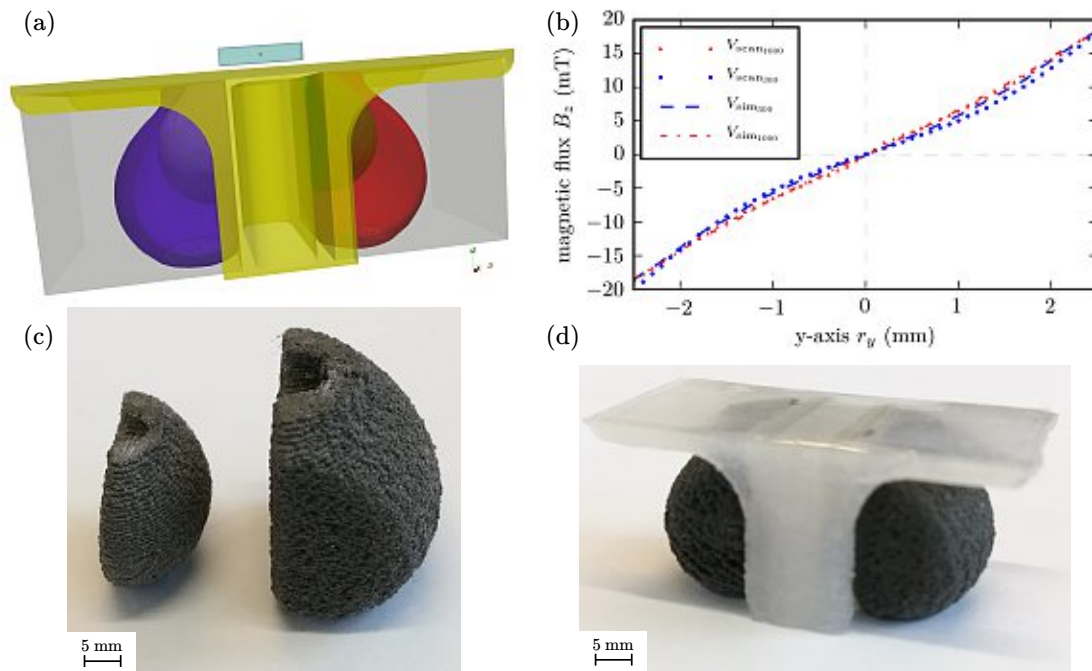


Figure 6.10: Comparison between simulations and measurements of the printed magnetic setup. (a) Setup for two different volume constraints (V_{1000} , V_{300}). (b) Line scan of the external field B_z , 2 mm above the system compared with simulation results for both volume constraints. (c) Picture of the magnets for both constraints (right: V_{1000} , left: V_{300}). (d) Picture of the hole magnetic setup for V_{1000} .

Figure 6.10(b) displays a comparison between magnetic field scans of the printed structures and the simulated magnetic field 2 mm above the magnet. For the magnetic field scanning, the 3D field mapping setup, as described above is used. It shows a good agreement between the topology optimized and the printed magnet. Figure 6.10(c) pictures the printed magnets for both volume constraints (right: V_{1000} , left: V_{300}), and figure 6.10(d) from the whole magnetic system with the printed socket for $V = 1000$ mm³.

6.5 Magnetic Scale

Last application showed a magnetic absolute linear positioning system. An advantage of such systems are the continuous measurement of distances. On the other side, such systems are only practicable for small distances. To measure positions up to 200 m by magnetic systems, another technique is necessary [146]. One possibility is to magnetize a scale with a defined magnetic pattern. Advantages of such magnetic encoder systems are: (i) compact design, (ii) affordable, (iii) a high reliability, and (iv) a minimum resolutions in the range of μm . One application of such magnetic encoder scale is the attitude control of a super-high speed elevator car [147].

In this work, the capability to generate such a magnetic scale by the “maxel” printer (see section 3.3) is investigated. As explained above, the minimum resolution of our setup is 0.5 mm and is therefore, much higher as for state-of-the-art systems. Nevertheless, the presented “maxel” printer can magnetize any pattern on a 3D printed magnetic structure.

To test the effectiveness of our system, two cuboid of size $10 \times 5 \times 3 \text{ mm}^3$ ($L \times W \times H$) are printed with Neofer[®] 25/60p. The first “printed” pattern are stripes, the second one a chessboard pattern. Both patterns are produced with the minimum resolution of 0.5 mm. After each 3D printed layer, the “maxel” printer magnetize the surface of the cuboid with the characteristic pattern. The result of printed stripes structure is pictured in figure 6.11(a) and for the chessboard pattern in figure 6.11(b). The peak of the field amplitude B_z varies with the position of the x -axis. This can be explained by the generation process of the “maxels”, A “maxel” with $+z$ -magnetization will be demagnetized a little bit by a “maxel” with a $-z$ -magnetization. However, these two examples show the effectiveness of the “maxel” printer to produce a magnetic scale with a resolution of 0.5 mm.

6.6 Larmor Spin-Rotator

The last application of this thesis deals with a Larmor spin-rotator. For measurements with neutrons, a high efficient spin-manipulation mechanism is required. As an example, neutron interferometry was first demonstrated in 1974 at the 250 kW Triga MARK-II reactor at the Technical University of Vienna [148]. In order to demonstrate quantum

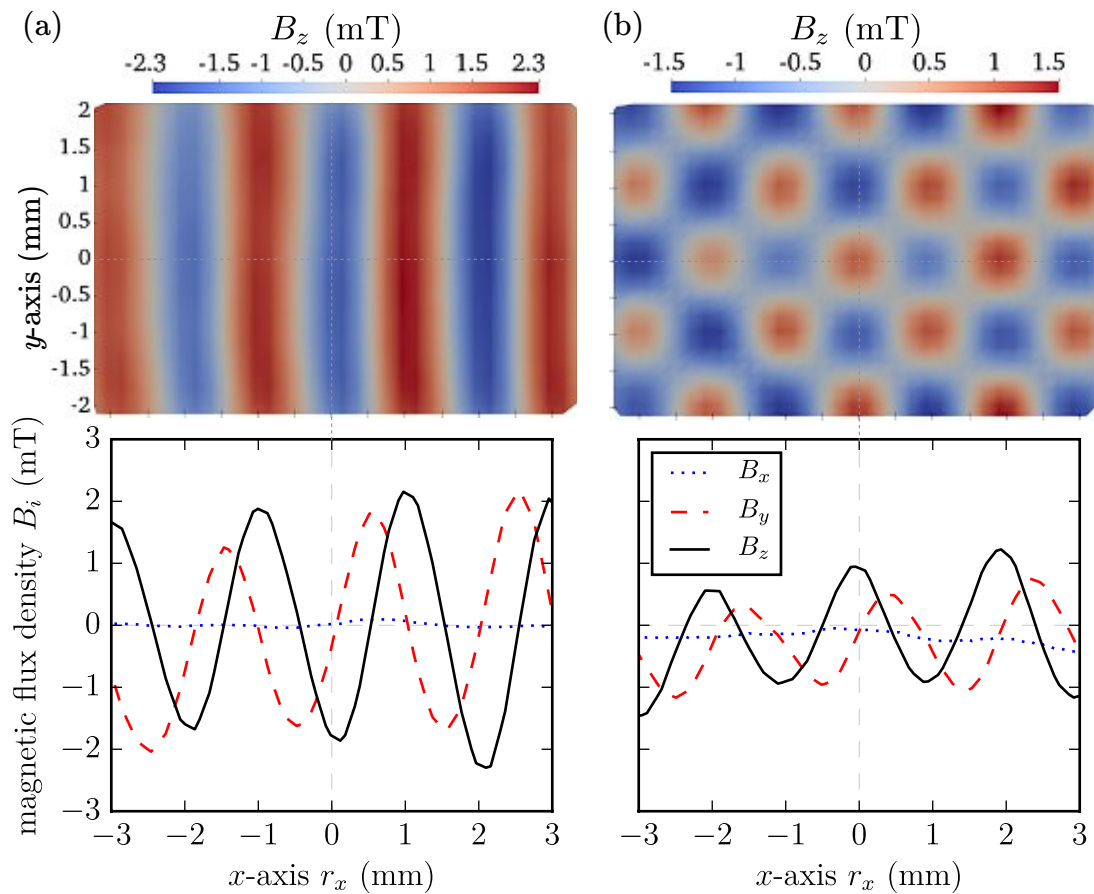


Figure 6.11: Magnetic linear incremental scales. (a) Area and line scan ($y = 0$ mm) of a 1D linear magnetic scale (pitch=2 mm), 1 mm above surface of a 3D printed structure (Neofer[®] 25/60p). (b) Area and line scan ($y = 0$ mm) of a chessboard pattern to generate a 2D magnetic scale (same material and measurement parameters).

mechanical properties of matter, neutron interferometry experiments are indispensable nowadays. One example, among others, is the test of Bell's inequality [149]. Testing of Bell's inequality violation can be only shown with a high interference contrast and a high spin polarization.

This section describes a complete new design of a Larmor spin-rotator. Inverse stray field and topology optimization simulations are performed to find an optimal shape of a permanent magnetic setup. Such a system has several advantages compared to previous systems. The effectiveness is shown with comparison between magnetic simulations and measurements as well as with tests with neutrons from the Triga MARK-II

reactor.

6.6.1 Current Setup

The current setup to test Bell's inequality violation at the Atominstitut of the Technical University of Vienna is shown in figure 6.12 [150]. The Larmor spin-rotator has a Helmholtz coil geometry. It applies an additional field to the guide field in z -direction locally, and thereby change the spin precession in the xy -plane. The rotation angle is given by

$$\alpha(B_z) = \frac{2\mu_N l}{\hbar v} B_z \quad (6.3)$$

where $\mu_N = -9.6623647 \times 10^{-27}$ J/T is the magnetic moment of a neutron, l is the length of the coil and v is the velocity of the neutrons.

Such a Larmor spin-rotator must have high homogeneous field along the neutron beam path. Because an inhomogeneous field would lead to a dephasing of the neutron and therefore, to a loss in contrast of the measurement. Another crucial point is the thermal stability of the setup. A change of temperature during the measurement leads to a loss in contrast as well as a phase drifts occur, e.g., a temperature change of 1 °C results in 1.92 rad phase shift. For this reason the current Larmor spin-rotator is water-cooled (figure 6.12(b)), but this leads to a complex setup of the experiment, as well as a temperature rise cannot be completely excluded.

To improve the current design, the actual condition should be examine more in detail. The neutron path is simplified by a field box Ω_f with a size of $7 \times 7 \times 40$ mm³ ($a \times a \times L$). To describe the influence of the magnetic field on the phase shift of the neutrons, the action Θ is defined as

$$\Theta = \frac{1}{a^2} \int_{\Omega_f} |B_z| dr. \quad (6.4)$$

To rotate the neutrons of $\alpha = \pi$, an action of $\Theta = 35$ mT · mm is necessary. The action of the current Helmholtz coil geometry is calculated by Magnum.fe. Figure 6.13(a) shows the geometry as well as field box with vectors of the magnetic field. The field shows an inhomogeneous behavior outside the coil. A calculation of the current I to reach an action of $\Theta = 35$ mT · mm is plotted in figure 6.13(b). An optimized design should be find with these results.

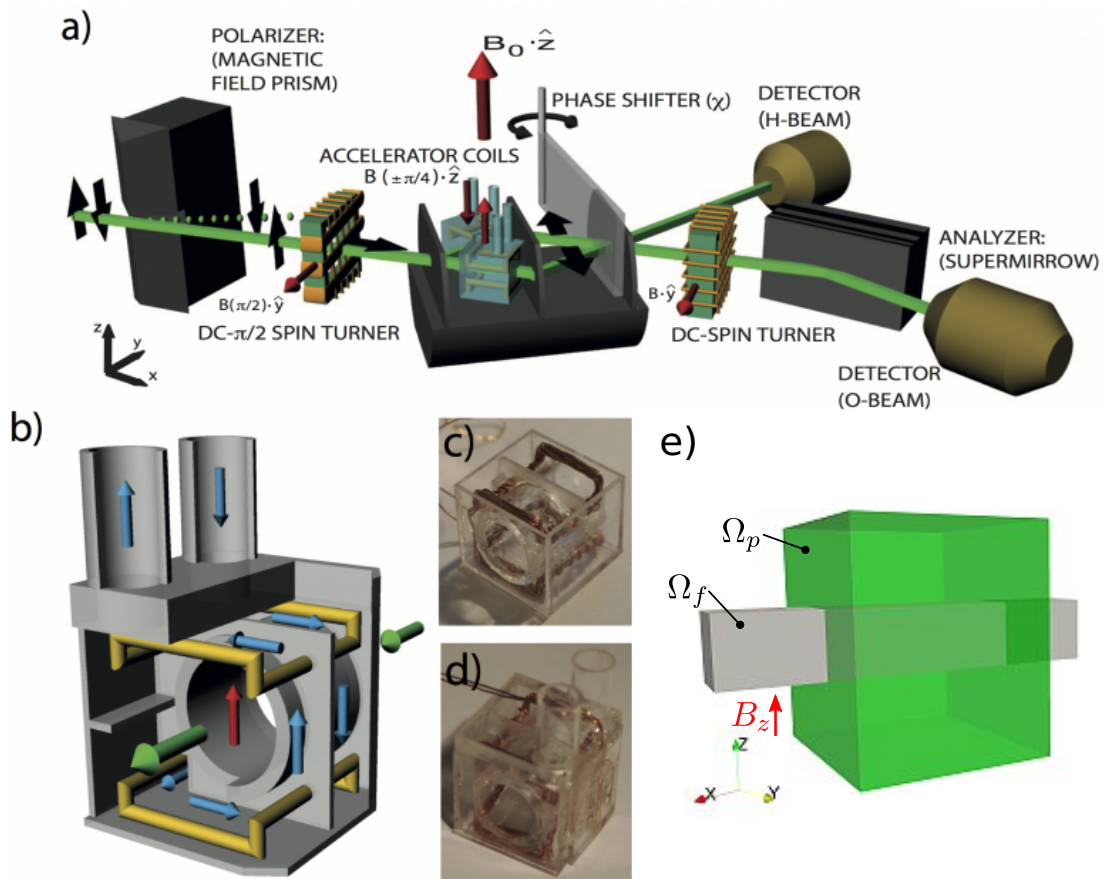


Figure 6.12: Current neutron interferometric setup. (a) Schematic view of the entire triple Laue interferometric setup. (b) Larmor spin-rotator boxes with coils in Helmholtz geometry (yellow), magnetic field (red), neutron beam (green) and water flux (blue), (c) Larmor spin-rotator coil with Helmholtz geometry in box, (d) closed box with connectors for water cooling. (e) Design and field domain for an optimized 3D printed permanent magnetic system. (Adapted from [150])

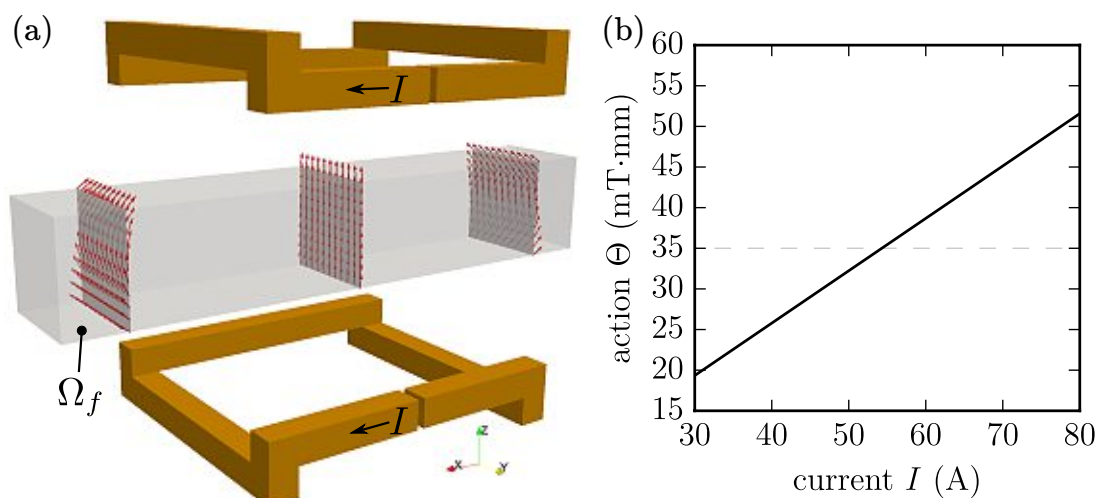


Figure 6.13: Current Larmor Spin-Rotator. (a) Modified Helmholtz coil geometry with the field box Ω_f (equal to neutron beam size). Normalized magnetic field vectors in red. (b) Action Θ as a function of the current I through the Helmholtz coil.

6.6.2 Optimized Designs

The idea is to find an optimized permanent magnetic Larmor spin-rotator by the usage of the inverse stray field and topology optimization framework. Following design parameters are given:

- Size of the field box Ω_f : $7 \times 7 \times 40 \text{ mm}^3$ ($a \times a \times L$).
- Maximum design volume Ω_p : $24 \times 24 \times 20 \text{ mm}^3$ ($a \times a \times L$).
- Action Θ of the external field: $\Theta = 35 \text{ mT}\cdot\text{mm}$.
- Θ is adjustable in the range of $\pm 5 \text{ mT}\cdot\text{mm}$.
- Homogeneous magnetic field density $\mathbf{B}(\mathbf{r})$ along z -axis: $\mathbf{B}(\mathbf{r}) = (0, 0, B_z)$.

A challenge for a permanent magnetic system is to make the action Θ adjustable. For the Helmholtz coil geometry, Θ is easily adjustable by the current through the coils. The easiest way to adjust Θ for a permanent magnetic setup is to change the distance between the neutron path (field box) and the magnets. To realize a homogeneous magnetic field density in the field box Ω_f , following functional for the minimization prob-

lem of equation 5.29 and 5.33 can given by

$$J = \int_{\Omega_f} \left(|\nabla B_x|^2 + |\nabla B_y|^2 + |(\nabla B_z)_y|^2 + |(\nabla B_z)_z|^2 \right) d\mathbf{r} \quad (6.5)$$

Two different initial designs are investigated to find a proper replacement of the Helmholtz coils. The first design is modified Halbach cylinder [151]. To archive a better field homogeneity outside the magnet, it is divided into two rows. To adjust Θ , it consist of thwo half halbach cylinders and the gap Δz between both halves is adjustable. In total 20 segments are used. Each permanent magnetic segment has a constant remanence $|B_r|$, but the direction of B_r is open and defines the optimization parameter for the inverse stray field optimization. Figure 6.15(a) shows the initial design of the modified Halbach cylinder. The fact that only the direction of the remanence is an optimization parameter, no regularization parameter is necessary. Figure 6.15(b) shows the result of the inverse stray field simulation for an action of $\Theta = 35 \text{ mT}\cdot\text{mm}$. In general, the magnetization (remanence) vectors have the same direction as a standard Halbach cylinder, only the segments on the top and bottom of the field box show a deviating direction.

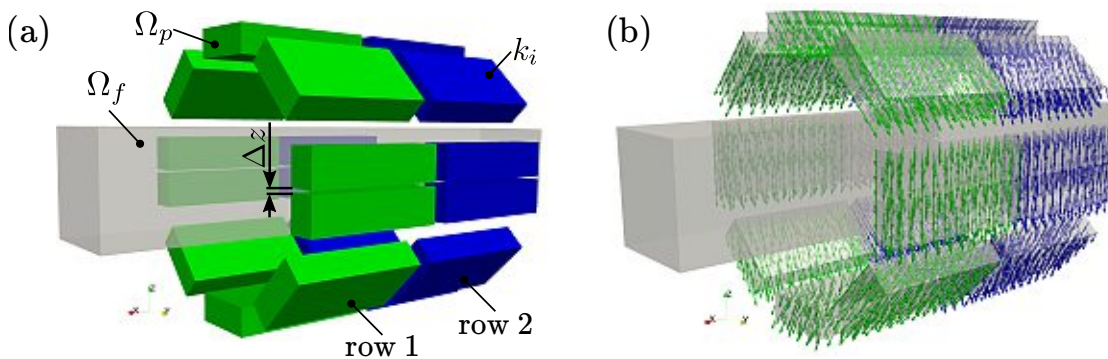


Figure 6.14: Modified and optimized Halbach cylinder. (a) Initial layout with 20 segments. Remanence $|B_r|$ is constant for each segment. Two rows should provide a homogeneous field outside of the magnets. (b) Result of the inverse stray field computation.

The second investigated design is a topology optimized one. Figure 6.15(a) shows the design domain Ω_p and the field box Ω_f where J of equation 6.5 should be minimized. To adjust Θ , the design consists of two halves, and the gap Δz is adjustable. The mesh of the design domain consist of 256,542 tetrahedral elements. No volume constraint is applied for the optimization. Figure 6.15(b) shows the topology optimized version of a permanent magnetic Larmor spin-rotator.

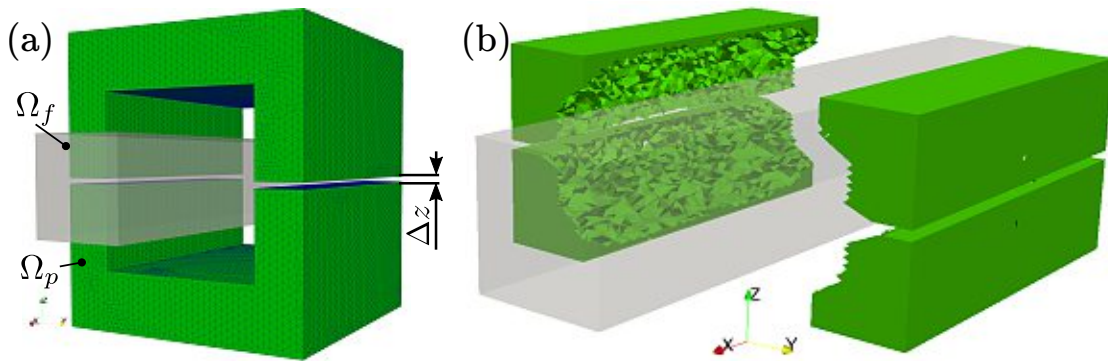


Figure 6.15: Initial designs for the optimized Larmor spin-rotator. (a) Modified Halbach cylinder for inverse stray field optimization. To generate a homogeneous field outside of the cylinder it is split into two rows. The action Θ is adjustable by the gap size Δz . Design space Ω_p for the topology optimization approach.

Several numerical experiments are performed to find the optimal parameters of both designs. To adjust Θ in both directions, a gap of $\Delta z = 2.25$ mm is chosen. To get an action of $\Theta = 35$ mT·mm, a remanence of the permanent magnet of $B_r = 61$ mT for the topology optimized version and $B_r = 68$ mT for the Halbach design is necessary. How Δz and B_r influences Θ , are plotted in figure 6.16. It exists a linear correlation between action and gap size. The topology optimized design is less sensitive for a changing Δz .

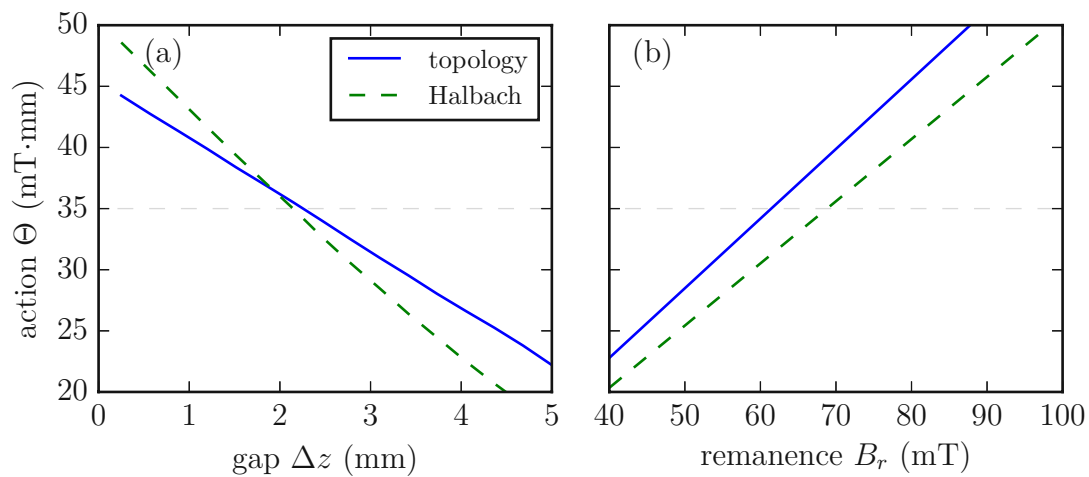


Figure 6.16: Simulation results for both optimized designs. (a) Action Θ as a function of the gap Δz ($B_r = 61$ mT for the topology optimized design and $B_r = 68$ mT for the Halbach cylinder), and (b) as a function of the remanence B_r of the magnet (gap $\Delta z = 2$ mm).

A crucial impact on the performance has the homogeneity of $\mathbf{B}(\mathbf{r})$ in the field box Ω_f . The relative error is defined as

$$\delta e = \frac{J}{\int_{\Omega_f} |\mathbf{B}|^2 d\mathbf{r}} \quad (6.6)$$

with the functional of equation 6.5. Figure 6.17(a) shows the relative error δe as a function of the gap Δz . The topology optimized design has a much lower relative error compared to the Halbach cylinder design, as well as the dependency of the gap is much lower for the topology optimized design. However, the main question is, if the optimized permanent magnetic design has a lower relative error, or a better performance as the current Helmholtz coil geometry. Figure 6.17(b) shows a plot of the relative error as a function of the action for the current and the both optimized designs. For the current design, δe is independent of Θ . In the range of around of $\Theta = 30 - 40$ mT·mm the topology optimized version shows a better performance.

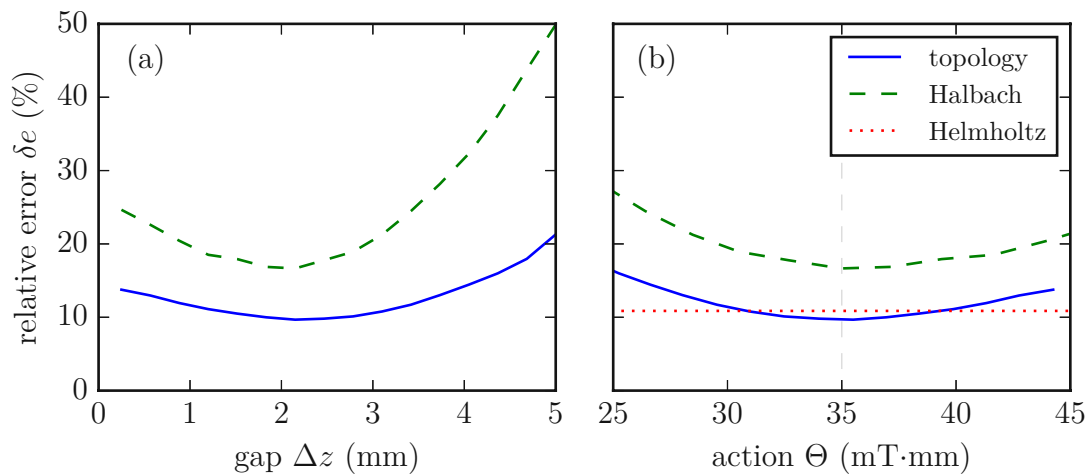


Figure 6.17: Relative error for both optimized designs. (a) Relative error δe as a function of the gap Δz . (b) Relative error as a function of the action Θ for the optimized designs and for the current Helmholtz coil geometry.

6.6.3 Validation

The topology optimized system is printed with Neofer[®] 25/60p. All four segments have the same shape. Figure 6.18(a) shows a picture of the printed segments. After the printing process, the magnets must be magnetized. Compared to all previous applications, only a weak magnetic field is necessary. The segments must have exactly

a remanence of $B_r = 61$ mT to generate an action of $\Theta = 35$ mT·mm for a gap of $\Delta z = 2.25$ mm. Magnetization of the segments are performed with an electromagnet as described in section 3.4. A jig with the exact positions of the segments is 3D printed. The jig is inserted into the electromagnet and the external field is increased in small steps. After each step, the magnetic field density of the segments is measured by the 3D Hall probe. FEM simulation of the arrangement yields a field of $B_z = 1.18$ mT in the center. With this approach a good adjustment of the remanence B_r is possible.

After the magnetization procedure, the magnetic field between the segments is measured and compared with simulation results. Figure 6.18(b) shows a volume scan between the segments and a line scan of B_z at $y = 0$ mm, $z = 0$ mm for the measured topology optimized version and the former Helmholtz coil geometry. Simulation results for $B_r = 61$ mT and measurements are in a good agreement. The vector field should illustrate the homogeneity of the measurement and simulations, respectively.

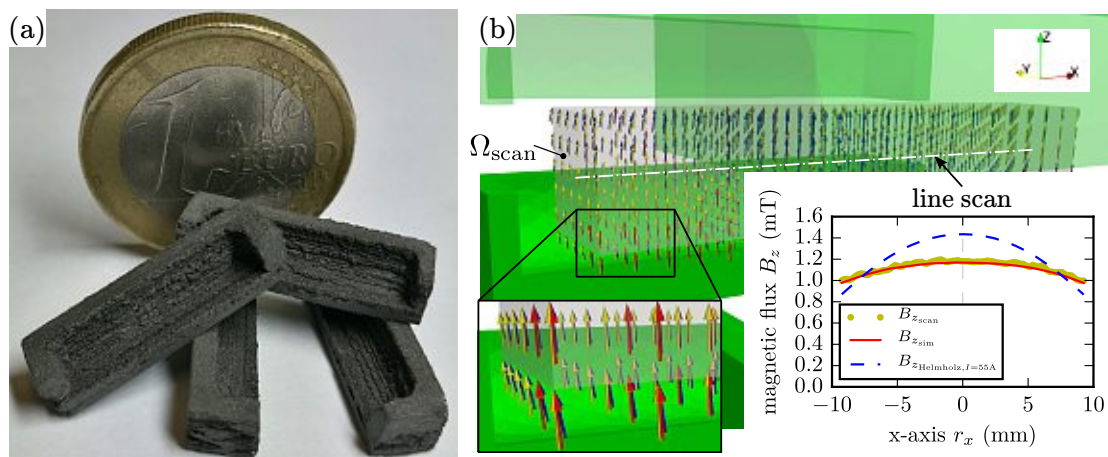


Figure 6.18: 3D printed Larmor spin-rotator and test of the magnetic performance. (a) Picture of the printed magnets with Neofer[®] 25/60p. (b) Volume scan between the magnets for a gap of $\Delta z = 2.25$ mm. Magnetic vectors (blue: Helmholtz coil simulation, red: topology optimization simulation, yellow: measurement) illustrates the homogeneity of the field. Line scan of B_z at $y = 0$ mm, $z = 0$ mm.

The real performance of the 3D printed Larmor spin-rotator can be only tested with a neutron experiment. For this reason, interference measurements with neutrons are performed at the Triga MARK-II reactor at the Atominstitut. Figure 6.19(a) shows a picture of the experimental setup. The gap Δz and therefore, the action Θ can be adjusted by a 3D printed mounting system with counter-rotating threads. A first coil after

the polarizer rotates the spin of the neutrons in flight direction then, a cadmium aperture with size of $5 \times 5 \text{ mm}^2$ ($a \times a$) reduces the beam. After the aperture, the beam enters the Larmor spin-rotator. The intensity modulation is created by varying the position of another coil (not visible on the picture) before the neutrons reach the detector and the spin is analyzed.

Interference patterns for different Δz are plotted in figure 6.19(b). The first measurements (black curve) shows a measurement without the Larmor spin-rotator. For a gap of $\Delta z = 2.25 \text{ mm}$ a phase shift of $\chi = \pi$ can be detected. This fits really well to the simulation for this action Θ . Another crucial parameter is the contrast of the setup. Here, a contrast of more than 95 % can be archived for a gap of $\Delta z = 2.25 \text{ mm}$. The old setup reach a contrast of maximum 91 %, and it depends on the temperature of the coils, as mentioned before.

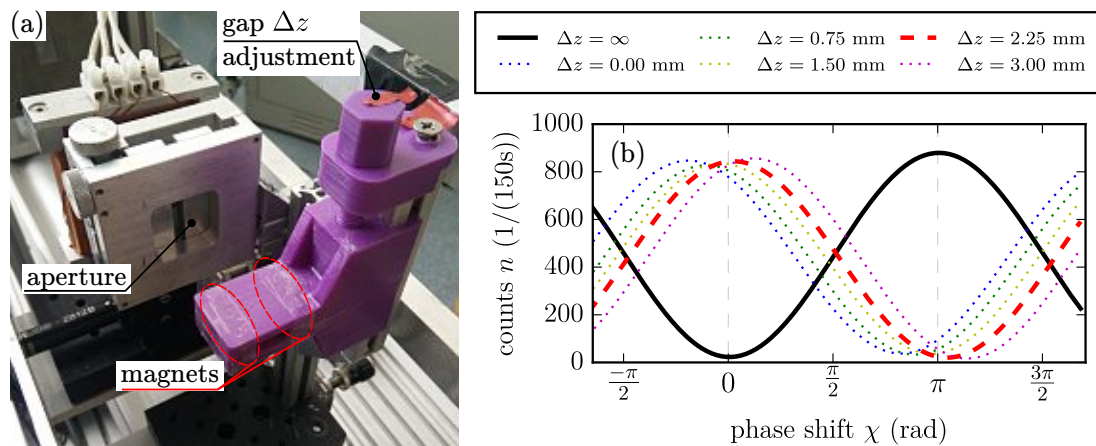


Figure 6.19: 3D printed Larmor spin-rotator neutron interference experiment. (a) Picture of the experimental setup. The gap Δz between the magnets can be adjusted by a self-printed adjustment mechanism. (b) Interference pattern for different gaps Δz .

This last sophisticated example shows the effectiveness of all introduced simulation methods, as well as the 3D printing process of polymer-bonded magnets in general. At time of writing this thesis, a more complex experiment at the Institut Laue-Langevin in Grenoble, France is ongoing.

7 Conclusion & Outlook

7.1 Conclusion

This thesis deals with additive manufacturing of polymer-bonded NdFeB magnets with a commercial available fused deposition modeling 3D printer. AM offers many advantages and additional benefits compared to conventional manufacturing processes. At the time of writing this thesis, a lot of inventions and innovations are going on that improves the techniques and processes of AM. Additionally, many technical developments and evolutions would not be possible without permanent magnets. Here, the first successful approach is described that combines these two technologies.

At the beginning of the thesis, a brief but wide overview about state of the art AM techniques is given. Several challenges for all AM process are discussed, as well as for FDM printer in detail. The challenges to produce objects with a high quality are the optimal printer parameters and adjustments. A detailed overview about all important printing parameters is described. To characterize the quality of the magnetic field of the printed magnets, the 3D printer is upgraded to a full 3D magnetic field mapping system. To avoid an exact positioning of the sensor, a calibration method relying on detailed stray field simulations is proposed. Our system has a good performance compared to high-price systems. To magnetize printed material during the printing process, our setup is upgraded to magnetic pixel (“maxel”) printer. The resolution of the “maxels” is restricted to 0.5 mm.

An crucial impact on the processability and for the further application is the used permanent magnetic material, as well as the matrix material for polymer-bonded magnets. A disadvantage of polymer-bonded magnets is their lower maximum energy product compared to conventional sintered magnets. However, many applications ex-

ists which need a tailored magnetic field and not a high field strength. Another important feature of polymer-bonded magnet is their procedural advantages of plastic technologies. In our case, the magnetic isotropic powder MQP-S-11-9 from Magnequench Corporation is used as magnetic filler material. As matrix materials, PA11 and PA12 are investigated. The filament manufacturing process was a sensitive process. Due to the high filling load of the powder, the produced filaments are extremely brittle. The production tolerances of the filaments are crucial, because finest calibration and most carefully printable designing leads to printing failures if the filament has a poor quality. The magnetic and mechanical properties of the manufactured filament materials are characterized by several methods. A big influence of the magnetic properties has the volumetric mass density of the prints. Some optimization are performed to increase the density of the prints, but with our setup and materials, the volumetric mass density and therefore, the remanence of the prints is reduced of about 25 %.

To get the most out of the 3D printed methodology, simulation tools are required to calculate the magnetic field distribution of a given printed structure. A simulation framework based on a pure FEM implementation is introduced, as well as a implementation of an inverse stray field code. By the aim of the open-source softwares FEniCS and Dolfin-adjoint, the Maxwell's equations for electrostatic are easily to implement. Several validation examples and numerical experiments show the effectiveness of the methods. Especially of interest for AM methods is the topology optimization approach. It allows the designer of magnetic systems to find a suitable topology of the magnets from scratch. Our implementation points out a good agreement between optimized designs and well known geometries.

Several examples demonstrates the effectiveness of the combination of the 3D printing method for polymer-bonded magnets and the introduced design tools. Examples ranges from magnetic speed wheel sensing systems to topology optimized linear positioning measurement systems. By the aim of the mixing extruder of our printer, magnets with a variable magnetic compound fraction can be realized. By the inverse stray field simulation framework, tailored magnetic field distribution are realized for sensing applications. A magnetic scale for positioning sensing is printed with the "maxel" printer. The minimum pitch size of such a system is with 2 mm much higher as for commercial scales, but our system enables to print "maxels" on any 3D printable magnetic design. The last application deals with neutron interferometric experiments. A new

design for a Larmour spin-rotator to manipulate the angle of the neutron spin is presented. The topology optimized design outperform the current design of a Helmholtz coil geometry.

7.2 Outlook

In this thesis, several new methods of AM and combinations of AM and design tools are presented. Nevertheless, there exists some possibilities to improve the performance, as well to extend possible printing materials and applications. The deviation of the ideal volumetric mass density and the printed one of around 25 % is a result of the flowability of the material and the FDM technique itself. Here is a potential for improvement of the printing results, and to reduce the error between simulations and measurements. At the moment, only prints with a variable magnetic compound fraction along the z -axis are possible. An improved slicing program should rescind this restriction. An influence on the quality of the printed structures is the filament diameter, because with a constant feeding rate, the volume flow through the nozzle varies, which leads to a patchy printing result.

A future challenge is the processing of anisotropic polymer-bonded magnet material. A possible composition of anisotropic ferrite is $\text{SrO} \times 6\text{Fe}_2\text{O}_3 + \text{PA12}$. Such a material is commercial available as Sprox[®] 11/22p from Magnetfabrik Bonn GmbH. The idea is to orientate the magnetic easy axis during the printing process by the aim of an electromagnet and a soft magnet flux concentrator. First tests with Sprox[®] 11/22p are full of expectations. An external field of about 100 mT is necessary to orientate the particles easy axis. With a 3D printer that can orientate anisotropic magnetic materials, completely new applications are possible.

Appendix

Rotation matrix with the Euler angles (γ, β, α)

$$\mathbf{R}_{ZYX} = \begin{pmatrix} \cos \gamma & \sin \gamma & 0 \\ -\sin \gamma & \cos \gamma & 0 \\ 0 & 0 & 1 \end{pmatrix} \begin{pmatrix} 1 & 0 & 0 \\ 0 & \cos \beta & \sin \beta \\ 0 & -\sin \beta & \cos \beta \end{pmatrix} \begin{pmatrix} \cos \alpha & \sin \alpha & 0 \\ -\sin \alpha & \cos \alpha & 0 \\ 0 & 0 & 1 \end{pmatrix}. \quad (\text{A.1})$$

**Demagnetizing factor of an uniformly magnetized ferromagnetic prism
(figure A.1(a)) [152]**

$$\begin{aligned} \pi D_z = & \frac{b^2 - c^2}{2bc} \ln \left(\frac{\sqrt{a^2 + b^2 + c^2} - a}{\sqrt{a^2 + b^2 + c^2} + a} \right) + \frac{a^2 - c^2}{2ac} \ln \left(\frac{\sqrt{a^2 + b^2 + c^2} - b}{\sqrt{a^2 + b^2 + c^2} + b} \right) \\ & + \frac{b}{2c} \ln \left(\frac{\sqrt{a^2 + b^2} + a}{\sqrt{a^2 + b^2} - a} \right) + \frac{a}{2c} \ln \left(\frac{\sqrt{a^2 + b^2} + b}{\sqrt{a^2 + b^2} - b} \right) \\ & + \frac{c}{2a} \ln \left(\frac{\sqrt{b^2 + c^2} - b}{\sqrt{b^2 + c^2} + b} \right) + \frac{c}{2b} \ln \left(\frac{\sqrt{a^2 + c^2} - a}{\sqrt{a^2 + c^2} + a} \right) \\ & + 2 \arctan \left(\frac{ab}{c\sqrt{a^2 + b^2 + c^2}} \right) + \frac{a^3 + b^3 - 2c^3}{3abc} \\ & + \frac{a^2 + b^2 - 2c^2}{3abc} \sqrt{a^2 + b^2 + c^2} + \frac{c}{ab} \left(\sqrt{a^2 + c^2} + \sqrt{b^2 + c^2} \right) \\ & - \frac{(a^2 + b^2)^{3/2} + (b^2 + c^2)^{3/2} + (c^2 + a^2)^{3/2}}{3abc}. \end{aligned} \quad (\text{A.2})$$

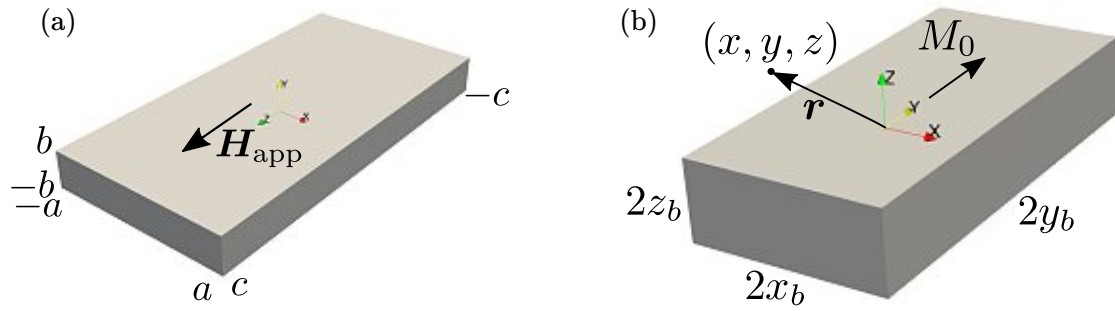


Figure A.1: (a) Calculation of the demagnetizing factor of a rectangular prism. The field \mathbf{H}_{app} is applied along the z -axis. (b) Calculation of the magnetic stray field of an uniaxial magnetic domain. The magnetization M_0 is along the y -axis, the dimensions of the magnet are $2x_b$, $2y_b$, and $2z_b$.

Calculation of the magnetic stray field of an uniaxial magnetic domain

(figure A.1(b)) [153]

$$H_x(x, y, z) = \frac{M_0}{4\pi} \sum_{k,l,m=1}^2 (-1)^{k+l+m} \ln \left[z + (-1)^m z_b + \sqrt{(x + (-1)^k x_b)^2 + (y + (-1)^l y_b)^2 + (z + (-1)^m z_b)^2} \right], \quad (\text{A.3})$$

$$H_y(x, y, z) = \frac{M_0}{4\pi} \sum_{k,l,m=1}^2 (-1)^{k+l+m} \frac{(y + (-1)^l y_b) (x + (-1)^k x_b)}{|y + (-1)^l y_b| |x + (-1)^k x_b|} \times \arctan \left(\frac{|x + (-1)^k x_b| (z + (-1)^m z_b)}{|y + (-1)^l y_b| \sqrt{(x + (-1)^k x_b)^2 + (y + (-1)^l y_b)^2 + (z + (-1)^m z_b)^2}} \right), \quad (\text{A.4})$$

$$H_z(x, y, z) = \frac{M_0}{4\pi} \sum_{k,l,m=1}^2 (-1)^{k+l+m} \ln \left[x + (-1)^k x_b + \sqrt{(x + (-1)^k x_b)^2 + (y + (-1)^l y_b)^2 + (z + (-1)^m z_b)^2} \right]. \quad (\text{A.5})$$

Bibliography

- [1] B. Kianian, "Wohlers report 2017: 3d printing and additive manufacturing state of the industry, annual worldwide progress report: Chapters titles: The middle east, and other countries," 2017.
- [2] B. L. Gupta and T. Abraham, "Permanent magnets - types, applications, new developments, industry structure and global markets," tech. rep., Innovative Research and Products (iRAP), Inc., 2014.
- [3] N. Guo and M. C. Leu, "Additive manufacturing: technology, applications and research needs," *Frontiers of Mechanical Engineering*, vol. 8, no. 3, pp. 215–243, 2013.
- [4] A. ASTM, "F2792-10 e1: Standard terminology for additive manufacturing technologies," *Annual Book of ASTM Standard, ASTM International, Pennsylvania*, pp. 671–673, 2012.
- [5] A. C. Brown and D. de Beer, "Development of a stereolithography (stl) slicing and g-code generation algorithm for an entry level 3-d printer," in *AFRICON, 2013*, pp. 1–5, 2013.
- [6] J. C. Steuben, A. P. Iliopoulos, and J. G. Michopoulos, "Implicit slicing for functionally tailored additive manufacturing," *Computer-Aided Design*, vol. 77, pp. 107 – 119, 2016.
- [7] I. Gibson, D. Rosen, and B. Stucker, *Additive Manufacturing Technologies: 3D Printing, Rapid Prototyping, and Direct Digital Manufacturing*. Springer, 2014.
- [8] P. F. Jacobs, "Fundamentals of stereolithography," in *Proceedings of the solid freeform fabrication symposium*, pp. 196–211, 1992.

- [9] A. KEŚY and J. KOTLIŃSKI, "Mechanical properties of parts produced by using polymer jetting technology," *Archives of Civil and Mechanical Engineering*, vol. 10, no. 3, pp. 37 – 50, 2010.
- [10] E. Sachs, M. Cima, and J. Cornie, "Three-dimensional printing: Rapid tooling and prototypes directly from a cad model," *CIRP Annals - Manufacturing Technology*, vol. 39, no. 1, pp. 201 – 204, 1990.
- [11] J. W. Comb, W. R. Priedeman, and P. W. Turley, "Fdm technology process improvements," in *Proceedings of Solid Freeform Fabrication Symposium*, pp. 42–49, 1994.
- [12] J. J. Beaman, J. W. Barlow, D. L. Bourell, R. H. Crawford, H. L. Marcus, and K. P. McAlea, "Solid freeform fabrication: a new direction in manufacturing," *Kluwer Academic Publishers, Norwell, MA*, vol. 2061, pp. 25–49, 1997.
- [13] J. Kruth, L. Froyen, J. V. Vaerenbergh, P. Mercelis, M. Rombouts, and B. Lauwers, "Selective laser melting of iron-based powder," *Journal of Materials Processing Technology*, vol. 149, no. 1, pp. 616 – 622, 2004. 14th International Symposium on Electromachining (ISEM XIV).
- [14] S. R. Seagle, R. L. Martin, and O. Berteau, "Electron-beam melting," *JOM*, vol. 14, pp. 812–820, Nov 1962.
- [15] Y. He, R. D. Wildman, C. J. Tuck, S. D. Christie, and S. Edmondson, "An investigation of the behavior of solvent based polycaprolactone ink for material jetting," *Scientific reports*, vol. 6, p. 20852, 2016.
- [16] B. Mueller and D. Kochan, "Laminated object manufacturing for rapid tooling and patternmaking in foundry industry," *Computers in Industry*, vol. 39, no. 1, pp. 47 – 53, 1999.
- [17] Y. Song, Y. Yan, R. Zhang, D. Xu, and F. Wang, "Manufacture of the die of an automobile deck part based on rapid prototyping and rapid tooling technology," *Journal of Materials Processing Technology*, vol. 120, no. 1, pp. 237 – 242, 2002.
- [18] C. L. Thomas, T. M. Gaffney, S. Kaza, and C. H. Lee, "Rapid prototyping of large scale aerospace structures," in *1996 IEEE Aerospace Applications Conference. Proceedings*, vol. 4, pp. 219–230 vol.4, Feb 1996.

- [19] J. Giannatsis and V. Dedoussis, "Additive fabrication technologies applied to medicine and health care: a review," *The International Journal of Advanced Manufacturing Technology*, vol. 40, pp. 116–127, Jan 2009.
- [20] M. O. Wang, C. E. Vorwald, M. L. Dreher, E. J. Mott, M.-H. Cheng, A. Cinar, H. Mehdizadeh, S. Somo, D. Dean, E. M. Brey, *et al.*, "Evaluating 3d-printed biomaterials as scaffolds for vascularized bone tissue engineering," *Advanced Materials*, vol. 27, no. 1, pp. 138–144, 2015.
- [21] M. Bonnet, "Kunststoffe in der ingenieuranwendung," *Vieweg+ Teubner, Wiesbaden*, 2009.
- [22] D. Bak, "Rapid prototyping or rapid production? 3d printing processes move industry towards the latter," *Assembly Automation*, vol. 23, no. 4, pp. 340–345, 2003.
- [23] R. Jones, P. Haufe, E. Sells, P. Iravani, V. Olliver, C. Palmer, and A. Bowyer, "Reprap—the replicating rapid prototyper," *Robotica*, vol. 29, no. 1, pp. 177–191, 2011.
- [24] A. Bellini, L. Shor, and S. I. Guceri, "New developments in fused deposition modeling of ceramics," *Rapid Prototyping Journal*, vol. 11, no. 4, pp. 214–220, 2005.
- [25] P. Dudek, "Fdm 3d printing technology in manufacturing composite elements," *Archives of Metallurgy and Materials*, vol. 58, no. 4, pp. 1415–1418, 2013.
- [26] L. E. Murr, S. M. Gaytan, D. A. Ramirez, E. Martinez, J. Hernandez, K. N. Amato, P. W. Shindo, F. R. Medina, and R. B. Wicker, "Metal fabrication by additive manufacturing using laser and electron beam melting technologies," *Journal of Materials Science & Technology*, vol. 28, no. 1, pp. 1 – 14, 2012.
- [27] T. R. Thomas, *Rough surfaces*. World Scientific, 1998.
- [28] P. M. Pandey, N. V. Reddy, and S. G. Dhande, "Slicing procedures in layered manufacturing: a review," *Rapid Prototyping Journal*, vol. 9, no. 5, pp. 274–288, 2003.
- [29] B. Berman, "3-d printing: The new industrial revolution," *Business Horizons*, vol. 55, no. 2, pp. 155 – 162, 2012.

- [30] P. Fastermann, *3D-Druck/Rapid Prototyping: Eine Zukunftstechnologie - kompakt erklärt*. Berlin Heidelberg: Springer, 2012.
- [31] T. T. Wohlers, T. Caffrey, and R. I. Campbell, *Wohlers Report 2016: 3D Printing and Additive Manufacturing State of the Industry Annual Worldwide Progress Report*. Wohlers Associates, 2016.
- [32] E. Brian, *Practical 3D Printers - The Science and Art of 3D Printing*. New York: Apress, 2012.
- [33] Sculpteo, "Comparison between 3d printing and traditional manufacturing processes for plastics," <https://www.sculpteo.com/en/>.
- [34] J. Jackson, *Classical electrodynamics*. New York: Wiley, 1999.
- [35] W. Demtröder, "Experimentalphysik 2," *Elektrizität und Optik, Kapitel*, vol. 10, 1995.
- [36] B. D. Cullity and C. D. Graham, *Introduction to magnetic materials*. John Wiley & Sons, 2011.
- [37] E. C. Stoner and E. Wohlfarth, "A mechanism of magnetic hysteresis in heterogeneous alloys," *Philosophical Transactions of the Royal Society of London. Series A. Mathematical and Physical Sciences*, pp. 599–642, 1948.
- [38] R. Boll and H. V. GmbH, *Weichmagnetische Werkstoffe: Einführung in den Magnetismus; VAC-Werkstoffe und ihre Anwendungen*. Siemens-Aktien-Ges., 1990.
- [39] J. Ormerod and S. Constantinides, "Bonded permanent magnets: Current status and future opportunities (invited)," *Journal of Applied Physics*, vol. 81, no. 8, pp. 4816–4820, 1997.
- [40] P. Campbell, *Permanent magnet materials and their application*. Cambridge University Press, 1996.
- [41] J. Coey, "Hard magnetic materials: A perspective," *IEEE Transactions on Magnetics*, vol. 47, no. 12, pp. 4671–4681, 2011.

- [42] O. Gutfleisch, M. A. Willard, E. Brück, C. H. Chen, S. Sankar, and J. P. Liu, "Magnetic materials and devices for the 21st century: stronger, lighter, and more energy efficient," *Advanced materials*, vol. 23, no. 7, pp. 821–842, 2011.
- [43] J. J. Croat, J. F. Herbst, R. W. Lee, and F. E. Pinkerton, "High-energy product nd-fe-b permanent magnets," *Applied Physics Letters*, vol. 44, no. 1, pp. 148–149, 1984.
- [44] D. Brown, B. Ma, and Z. Chen, "Developments in the processing and properties of ndfeb-type permanent magnets," *Journal of Magnetism and Magnetic Materials*, vol. 248, no. 3, pp. 432 – 440, 2002.
- [45] D. Li, S. Gaiffi, D. Kirk, K. Young, J. Herchenroeder, and T. Berwald, "Liquid coated melt-spun nd-fe-b powders for bonded magnets," *Journal of Applied Physics*, vol. 85, no. 8, pp. 4871–4873, 1999.
- [46] B. Ma, J. Herchenroeder, B. Smith, M. Suda, D. Brown, and Z. Chen, "Recent development in bonded ndfeb magnets," *Journal of Magnetism and Magnetic Materials*, vol. 239, no. 1–3, pp. 418 – 423, 2002.
- [47] R. Lee, "Hot-pressed neodymium-iron-boron magnets," *Applied Physics Letters*, vol. 46, no. 8, pp. 790–791, 1985.
- [48] J. Coey, "Permanent magnet applications," *Journal of Magnetism and Magnetic Materials*, vol. 248, no. 3, pp. 441 – 456, 2002.
- [49] S. Eimeke and G. Ehrenstein, "Processing strategies for the production of polymer-bonded micro magnets," *Annual Technical Conference - ANTEC*, vol. 1, pp. 461–465, 05 2006.
- [50] K. Elian and H. Theuss, "Integration of polymer bonded magnets into magnetic sensors," in *Electronics System-Integration Technology Conference (ESTC), 2014*, pp. 1–5, Sept 2014.
- [51] S. V. Joshi, L. Drzal, A. Mohanty, and S. Arora, "Are natural fiber composites environmentally superior to glass fiber reinforced composites?," *Composites Part A: Applied science and manufacturing*, vol. 35, no. 3, pp. 371–376, 2004.
- [52] J.-B. Donnet, *Carbon black: science and technology*. CRC Press, 1993.

- [53] M. Anhalt and B. Weidenfeller, "Magnetic properties of polymer bonded soft magnetic particles for various filler fractions," *Journal of applied physics*, vol. 101, no. 2, p. 023907, 2007.
- [54] S. Egelkraut, M. Maerz, and H. Ryssel, "Polymer bonded soft magnetic particles for planar inductive devices," in *Integrated Power Systems (CIPS), 2008 5th International Conference on*, pp. 1–8, VDE, 2008.
- [55] S. Eimeke, A. Gardocki, G. Ehrenstein, and D. Drummer, "Effects during injection molding of polymer- bonded magnets with multipolar structure," *Journal of Plastics Technology*, vol. 5, 05 2008.
- [56] C. Ibeh, *Thermoplastic Materials - Properties, Manufacturing Methods, and Applications*. Justus-Liebig-Universität Gießen: Taylor & Francis, 2011.
- [57] H. Domininghaus, *Kunststoffe: Eigenschaften und Anwendungen*. Springer-Verlag, 2007.
- [58] M. R. Jolly, J. D. Carlson, and B. C. Munoz, "A model of the behaviour of magnetorheological materials," *Smart Materials and Structures*, vol. 5, no. 5, p. 607, 1996.
- [59] H.-x. Deng, X.-l. Gong, and L.-h. Wang, "Development of an adaptive tuned vibration absorber with magnetorheological elastomer," *Smart materials and structures*, vol. 15, no. 5, p. N111, 2006.
- [60] M. Sarasa, *Einsatz neuer weichmagnetischer Werkstoffe bei elektrischen Maschinen im Kraftfahrzeug*. PhD thesis, Universität der Bundeswehr München, Universitätsbibliothek, 2005.
- [61] A. D. McNaught and A. D. McNaught, *Compendium of chemical terminology*, vol. 1669. Blackwell Science Oxford, 1997.
- [62] A. Markov, "Rheologisches Verhalten hochgefüllter Kunststoffe. Einfluss der Füllstoffe," *Materialwissenschaft und Werkstofftechnik*, vol. 39, no. 3, pp. 227–233, 2008.
- [63] B. Hochstein, *Rheologie von Kugel- und Fasersuspensionen mit viskoelastischen Matrixflüssigkeiten*. PhD thesis, Karlsruhe, Univ., Diss., 1997, 1997.

- [64] M. G. Garrell, A. J. Shih, B.-M. Ma, E. Lara-Curzio, and R. O. Scattergood, "Mechanical properties of nylon bonded nd-fe-b permanent magnets," *Journal of Magnetism and Magnetic Materials*, vol. 257, no. 1, pp. 32–43, 2003.
- [65] *Werkstoffkunde Kunststoffe*. Hanser Fachbuchverlag.
- [66] S. Kirchberg, *Einfluss von Fullgrad und Geometrie weichmagnetischer Partikel auf die Verarbeitungs- und Materialeigenschaften ausgewählter Thermoplaste*. PhD thesis, Zugl.: Clausthal, Techn. Univ., Diss., 2009, 2011.
- [67] A. Morrish and S. Yu, "Dependence of the coercive force on the density of some iron oxide powders," *Journal of Applied Physics*, vol. 26, no. 8, pp. 1049–1055, 1955.
- [68] V. D. Bruggeman, "Berechnung verschiedener physikalischer konstanten von heterogenen substanzen. i. dielektrizitätskonstanten und leitfähigkeiten der mischkörper aus isotropen substanzen," *Annalen der physik*, vol. 416, no. 7, pp. 636–664, 1935.
- [69] E. A. Perigo, I. A. Cruz, B. Antunes, A. Braga, and F. J. G. Landgraf, "How extrinsic is the coercivity in ndfeb bonded magnets?," *IEEE Transactions on Magnetics*, vol. 49, no. 9, pp. 5043–5047, 2013.
- [70] C. Furnas, "Grading aggregates-i-mathematical relations for beds of broken solids of maximum density," *Industrial & Engineering Chemistry*, vol. 23, no. 9, pp. 1052–1058, 1931.
- [71] E. Abdullah and D. Geldart, "The use of bulk density measurements as flowability indicators," *Powder technology*, vol. 102, no. 2, pp. 151–165, 1999.
- [72] C. Rauwendaal, *Polymer extrusion*. Carl Hanser Verlag GmbH Co KG, 2014.
- [73] Y. Yan, K. D. Ngo, Y. Mei, and G.-Q. Lu, "Additive manufacturing of magnetic components for power electronics integration," in *Electronics Packaging (ICEP), 2016 International Conference on*, pp. 368–371, IEEE, 2016.
- [74] B. Zhang, N.-E. Fenineche, H. Liao, and C. Coddet, "Magnetic properties of in-situ synthesized fe-80% ni powders," *Journal of Magnetism and Magnetic Materials*, vol. 336, pp. 49–54, 2013.

- [75] C. Mikler, V. Chaudhary, T. Borkar, V. Soni, D. Jaeger, X. Chen, R. Contieri, R. Ramanujan, and R. Banerjee, "Laser additive manufacturing of magnetic materials," *JOM*, vol. 69, no. 3, pp. 532–543, 2017.
- [76] L. M. Bollig, M. V. Patton, G. S. Mowry, and B. B. Nelson-Cheeseman, "Effects of 3d printed structural characteristics on magnetic properties," *IEEE Transactions on Magnetics*, 2017.
- [77] J. Jaćimović, F. Binda, L. G. Herrmann, F. Greuter, J. Genta, M. Calvo, T. Tomše, and R. A. Simon, "Net shape 3d printed ndfeb permanent magnet," *Advanced Engineering Materials*, 2017.
- [78] R. Fischer, T. Schrefl, H. Kronmüller, and J. Fidler, "Grain-size dependence of remanence and coercive field of isotropic nanocrystalline composite permanent magnets," *Journal of magnetism and magnetic materials*, vol. 153, no. 1-2, pp. 35–49, 1996.
- [79] M. P. Paranthaman, C. S. Shafer, A. M. Elliott, D. H. Siddel, M. A. McGuire, R. M. Springfield, J. Martin, R. Fredette, and J. Ormerod, "Binder jetting: A novel ndfeb bonded magnet fabrication process," *JOM*, vol. 68, no. 7, pp. 1978–1982, 2016.
- [80] L. Li, A. Tirado, B. S. Conner, M. Chi, A. M. Elliott, O. Rios, H. Zhou, and M. P. Paranthaman, "A novel method combining additive manufacturing and alloy infiltration for ndfeb bonded magnet fabrication," *Journal of Magnetism and Magnetic Materials*, vol. 438, pp. 163–167, 2017.
- [81] L. Li, A. Tirado, I. C. Nlebedim, O. Rios, B. Post, V. Kunc, R. R. Lowden, E. Lara-Curzio, R. Fredette, J. Ormerod, T. A. Lograsso, and M. P. Paranthaman, "Big area additive manufacturing of high performance bonded ndfeb magnets," *Scientific Reports*, vol. 6, p. 36212, Oct 2016.
- [82] C. Huber, C. Abert, F. Bruckner, M. Groenefeld, O. Muthsam, S. Schuschnigg, K. Sirak, R. Thanhoffer, I. Teliban, C. Vogler, R. Windl, and D. Suess, "3d print of polymer bonded rare-earth magnets, and 3d magnetic field scanning with an end-user 3d printer," *Applied Physics Letters*, vol. 109, no. 16, p. 162401, 2016.
- [83] T. R. Kramer, F. M. Proctor, and E. Messina, *The nist rs274ngc interpreter-version 3*, vol. 5416. 2000.

- [84] T. Reiner, N. Carr, R. Měch, O. Št'ava, C. Dachsbacher, and G. Miller, "Dual-color mixing for fused deposition modeling printers," in *Computer Graphics Forum*, vol. 33, pp. 479–486, Wiley Online Library, 2014.
- [85] Z. Zhao and Z. Luc, "Adaptive direct slicing of the solid model for rapid prototyping," *International Journal of Production Research*, vol. 38, no. 1, pp. 69–83, 2000.
- [86] G. Jin, W. Li, C. Tsai, and L. Wang, "Adaptive tool-path generation of rapid prototyping for complex product models," *Journal of manufacturing systems*, vol. 30, no. 3, pp. 154–164, 2011.
- [87] J. Lenz and S. Edelstein, "Magnetic sensors and their applications," *IEEE Sensors journal*, vol. 6, no. 3, pp. 631–649, 2006.
- [88] W. Gopel, "Sensor a comprehensive survey volume 5 magnetic sensor," VCH, Weinheim, 1989.
- [89] D. R. Popovic, S. Dimitrijevic, M. Blagojevic, P. Kejik, E. Schurig, and R. S. Popovic, "Three-axis teslameter with integrated hall probe," *IEEE Transactions on instrumentation and measurement*, vol. 56, no. 4, pp. 1396–1402, 2007.
- [90] L. Breth, *Detection of weak magnetic fields: The TMR fluxgate sensing technology and its limits*. PhD thesis, TU-Wien, 2016.
- [91] H. Husstedt, *Messung von Magnetfeldern fur das Testen von Automobilsensoren*. PhD thesis, Johannes Kepler Universität Linz, 2012.
- [92] P. Yiu, "The uses of homogeneous barycentric coordinates in plane euclidean geometry," *International Journal of Mathematical Education in Science and Technology*, vol. 31, no. 4, pp. 569–578, 2000.
- [93] D.-T. Lee and B. J. Schachter, "Two algorithms for constructing a delaunay triangulation," *International Journal of Computer & Information Sciences*, vol. 9, no. 3, pp. 219–242, 1980.
- [94] M. J. D. Powell, "An efficient method for finding the minimum of a function of several variables without calculating derivatives," *The Computer Journal*, vol. 7, no. 2, pp. 155–162, 1964.

- [95] L. W. Fullerton and M. D. Roberts, "Apparatus and method for printing maxels," Aug. 11 2015. US Patent 9,105,384.
- [96] J. Camacho and V. Sosa, "Alternative method to calculate the magnetic field of permanent magnets with azimuthal symmetry," *Revista mexicana de fisica E*, vol. 59, no. 1, pp. 8–17, 2013.
- [97] C. Huber, C. Abert, F. Bruckner, M. Groenefeld, S. Schuschnigg, I. Teliban, C. Vogler, G. Wautischer, R. Windl, and D. Suess, "3d printing of polymer-bonded rare-earth magnets with a variable magnetic compound fraction for a predefined stray field," *Scientific Reports*, vol. 7, p. 9419, Aug 2017.
- [98] C. Huber, C. Abert, F. Bruckner, C. Pfaff, J. Kriwet, M. Groenefeld, I. Teliban, C. Vogler, and D. Suess, "Topology optimized and 3d printed polymer-bonded permanent magnets for a predefined external field," *Journal of Applied Physics*, vol. 122, no. 5, p. 053904, 2017.
- [99] J. J. Croat, "High energy product rare earth-iron magnet alloys," Feb. 7 1989. US Patent 4,802,931.
- [100] R. Groesinger, "Characterisation of hard magnetic materials," *Journal of Electrical Engineering*, vol. 59, no. 7, pp. 15–20, 2008.
- [101] G. Jewell, D. Howe, C. Schotzko, and R. Grossinger, "A method for assessing eddy current effects in pulsed magnetometry," *IEEE transactions on magnetics*, vol. 28, no. 5, pp. 3114–3116, 1992.
- [102] D. Givord, P. Tenaud, and T. Viadieu, "Coercivity mechanisms in ferrites and rare earth transition metal sintered magnets (smco/sub 5/, nd-fe-b)," *IEEE Transactions on Magnetism*, vol. 24, no. 2, pp. 1921–1923, 1988.
- [103] N. Mehboob, *Hysteresis Properties of Soft Magnetic Materials*. PhD thesis, Universität Wien, 2012.
- [104] S. Astm, "Standard test method for dynamic young's modulus," *Shear Modulus, and Poisson's Ratio by Impluse Excitation of Vibration*, West Conshohocken: ASTM International, vol. 1878, 1876.

- [105] S.-H. Ahn, M. Montero, D. Odell, S. Roundy, and P. K. Wright, "Anisotropic material properties of fused deposition modeling abs," *Rapid prototyping journal*, vol. 8, no. 4, pp. 248–257, 2002.
- [106] M. I. Qadeer, S. J. Savage, U. W. Gedde, and M. S. Hedenqvist, "Rheological and dynamic mechanical properties of polymer-bonded magnets based on sm2co17 and polyamide-12," *Journal of materials science*, vol. 49, no. 21, pp. 7529–7538, 2014.
- [107] K. Ziegel and A. Romanov, "Modulus reinforcement in elastomer composites. i. inorganic fillers," *Journal of Applied Polymer Science*, vol. 17, no. 4, pp. 1119–1131, 1973.
- [108] A. Tikhonov, A. Goncharsky, V. Stepanov, and A. G. Yagola, *Numerical Methods for the Solution of Ill-Posed Problems (Mathematics and Its Applications)*. Springer, 1995.
- [109] X. Brunotte, G. Meunier, and J.-F. Imhoff, "Finite element modeling of unbounded problems using transformations: a rigorous, powerful and easy solution," *IEEE Transactions on Magnetics*, vol. 28, no. 2, pp. 1663–1666, 1992.
- [110] C. Abert, G. Selke, B. Kruger, and A. Drews, "A fast finite-difference method for micromagnetics using the magnetic scalar potential," *IEEE Transactions on Magnetics*, vol. 48, no. 3, pp. 1105–1109, 2012.
- [111] D. R. Fredkin and T. R. Koehler, "Hybrid method for computing demagnetizing fields," *IEEE Transactions on Magnetics*, vol. 26, pp. 415–417, Mar 1990.
- [112] C. Abert, L. Exl, G. Selke, A. Drews, and T. Schrefl, "Numerical methods for the stray-field calculation: A comparison of recently developed algorithms," *Journal of Magnetism and Magnetic Materials*, vol. 326, pp. 176 – 185, 2013.
- [113] V. Panchanathan, "Studies on low rare earth nd-fe-b compositions," *IEEE Transactions on Magnetics*, vol. 31, no. 6, pp. 3605–3607, 1995.
- [114] D. Braess, *Finite elements: Theory, fast solvers, and applications in solid mechanics*. Cambridge University Press, 2007.
- [115] P. G. Ciarlet, *The finite element method for elliptic problems*. SIAM, 2002.

- [116] Y. Saad and M. H. Schultz, "Gmres: A generalized minimal residual algorithm for solving nonsymmetric linear systems," *SIAM Journal on scientific and statistical computing*, vol. 7, no. 3, pp. 856–869, 1986.
- [117] M. S. Alnæs, J. Blechta, J. Hake, A. Johansson, B. Kehlet, A. Logg, C. Richardson, J. Ring, M. E. Rognes, and G. N. Wells, "The fenics project version 1.5," *Archive of Numerical Software*, vol. 3, no. 100, 2015.
- [118] A. Logg, *Automated Solution of Differential Equations by the Finite Element Method (Lecture Notes in Computational Science and Engineering)*. Springer, 2013.
- [119] M. S. Alnæs, A. Logg, K. B. Ølgaard, M. E. Rognes, and G. N. Wells, "Unified form language: A domain-specific language for weak formulations of partial differential equations," *ACM Transactions on Mathematical Software*, vol. 40, no. 2, 2014.
- [120] A. Logg and G. N. Wells, "Dolfin: Automated finite element computing," *ACM Transactions on Mathematical Software*, vol. 37, no. 2, 2010.
- [121] A. Logg, K. B. Ølgaard, M. E. Rognes, and G. N. Wells, *FFC: the FEniCS Form Compiler*, ch. 11. Springer, 2012.
- [122] J. Schöberl, "Netgen an advancing front 2d/3d-mesh generator based on abstract rules," *Computing and Visualization in Science*, vol. 1, no. 1, pp. 41–52, 1997.
- [123] C. Abert, L. Exl, F. Bruckner, A. Drews, and D. Suess, "magnum. fe: A micromagnetic finite-element simulation code based on fenics," *Journal of Magnetism and Magnetic Materials*, vol. 345, pp. 29–35, 2013.
- [124] Q. Chen and A. Konrad, "A review of finite element open boundary techniques for static and quasi-static electromagnetic field problems," *IEEE Transactions on Magnetics*, vol. 33, pp. 663–676, Jan 1997.
- [125] F. Bruckner, C. Abert, C. Vogler, F. Heinrichs, A. Satz, U. Ausserlechner, G. Binder, H. Koeck, and D. Suess, "Macroscopic simulation of isotropic permanent magnets," *Journal of Magnetism and Magnetic Materials*, vol. 401, pp. 875 – 879, 2016.

- [126] F. Bruckner, C. Abert, G. Wautischer, C. Huber, C. Vogler, M. Hinze, and D. Suess, "Solving large-scale inverse magnetostatic problems using the adjoint method," *Scientific Reports*, vol. 7, p. 40816, Jan 2017.
- [127] S. Wang and J. Kang, "Shape optimization of bldc motor using 3-d finite element method," *IEEE Transactions on Magnetics*, vol. 36, pp. 1119–1123, Jul 2000.
- [128] A. R. Insinga, R. Bjørk, A. Smith, and C. R. H. Bahl, "Globally optimal segmentation of permanent-magnet systems," *Phys. Rev. Applied*, vol. 5, p. 064014, Jun 2016.
- [129] M. Ortner, "Improving magnetic linear position measurement by field shaping," in *2015 9th International Conference on Sensing Technology (ICST)*, pp. 359–364, Dec 2015.
- [130] N. I. Klevets, "Optimal design of magnetic systems," *Journal of Magnetism and Magnetic Materials*, vol. 306, no. 2, pp. 281 – 291, 2006.
- [131] S. W. Funke and P. E. Farrell, "A framework for automated PDE-constrained optimisation," *ArXiv e-prints*, Feb. 2013.
- [132] F. Campelo, J. Ramirez, and H. Igarashi, "A survey of topology optimization in electromagnetics: considerations and current trends," *Academia*, 2010.
- [133] V. Komkov, K. K. Choi, and E. J. Haug, *Design sensitivity analysis of structural systems*, vol. 177. Academic press, 1986.
- [134] H. Akel and J. Webb, "Design sensitivities for scattering-matrix calculation with tetrahedral edge elements," *IEEE Transactions on Magnetics*, vol. 36, no. 4, pp. 1043–1046, 2000.
- [135] I.-h. Park, B.-t. Lee, and S.-y. Hahn, "Design sensitivity analysis for nonlinear magnetostatic problems using finite element method," *IEEE transactions on magnetics*, vol. 28, no. 2, pp. 1533–1536, 1992.
- [136] O'Leary and D. Prost, "The use of the l-curve in the regularization of discrete ill-posed problems," *Society for Industrial and Applied Mathematics*, vol. 14, no. 5, pp. 1287–1503, 1993.

- [137] P. E. Farrell, D. A. Ham, S. W. Funke, and M. E. Rognes, "Automated derivation of the adjoint of high-level transient finite element programs," *SIAM Journal on Scientific Computing*, vol. 35, no. 4, pp. C369–C393, 2013.
- [138] C. Zhu, R. H. Byrd, P. Lu, and J. Nocedal, "Algorithm 778: L-bfgs-b: Fortran subroutines for large-scale bound-constrained optimization," *ACM Transactions on Mathematical Software (TOMS)*, vol. 23, no. 4, pp. 550–560, 1997.
- [139] A. Wächter and L. T. Biegler, "On the implementation of an interior-point filter line-search algorithm for large-scale nonlinear programming," *Mathematical Programming*, vol. 106, no. 1, pp. 25–57, 2006.
- [140] M. P. Bendsoe and O. Sigmund, *Topology Optimization*. Springer, 2004.
- [141] Y. Okamoto, K. Akiyama, and N. Takahashi, "3-d topology optimization of single-pole-type head by using design sensitivity analysis," *IEEE Transactions on Magnetics*, vol. 42, pp. 1087–1090, April 2006.
- [142] J. S. Choi and J. Yoo, "Simultaneous structural topology optimization of electromagnetic sources and ferromagnetic materials," *Computer Methods in Applied Mechanics and Engineering*, vol. 198, no. 27–29, pp. 2111 – 2121, 2009.
- [143] S. Wang and J. Kang, "Topology optimization of nonlinear magnetostatics," *IEEE Transactions on Magnetics*, vol. 38, pp. 1029–1032, Mar 2002.
- [144] S. Wang, D. Youn, H. Moon, and J. Kang, "Topology optimization of electromagnetic systems considering magnetization direction," *IEEE Transactions on Magnetics*, vol. 41, pp. 1808–1811, May 2005.
- [145] C. Treutler, "Magnetic sensors for automotive applications," *Sensors and Actuators A: Physical*, vol. 91, no. 1–2, pp. 2 – 6, 2001. Third European Conference on Magnetic Sensors & Actuators.
- [146] J. Novak and B. Cvetkovic, "Magnetic encoder scale and reference mark applicator and template," Mar. 26 2013. US Patent 8,405,387.
- [147] H. Inaba, M. Shigeta, T. Ando, A. Nokita, and M. Konya, "Attitude control system of a super-high speed elevator car based on magnetic guides," in *Industrial Elec-*

- tronics, Control and Instrumentation, 1994. IECON'94., 20th International Conference on*, vol. 2, pp. 1028–1033, IEEE, 1994.
- [148] H. Rauch, W. Treimer, and U. Bonse, “Test of a single crystal neutron interferometer,” *Physics Letters A*, vol. 47, no. 5, pp. 369–371, 1974.
- [149] Y. Hasegawa, R. Loidl, G. Badurek, M. Baron, and H. Rauch, “Violation of a bell-like inequality in single-neutron interferometry,” *Nature*, vol. 425, no. 6953, pp. 45–48, 2003.
- [150] H. Geppert, T. Denkmayr, S. Sponar, H. Lemmel, and Y. Hasegawa, “Improvement of the polarized neutron interferometer setup demonstrating violation of a bell-like inequality,” *Nuclear Instruments and Methods in Physics Research Section A: Accelerators, Spectrometers, Detectors and Associated Equipment*, vol. 763, pp. 417–423, 2014.
- [151] R. Bjørk, C. R. H. Bahl, A. Smith, and N. Pryds, “Comparison of adjustable permanent magnetic field sources,” *Journal of Magnetism and Magnetic Materials*, vol. 322, no. 22, pp. 3664–3671, 2010.
- [152] A. Aharoni, “Demagnetizing factors for rectangular ferromagnetic prisms,” *Journal of Applied Physics*, vol. 83, no. 6, pp. 3432–3434, 1998.
- [153] R. Engel-Herbert and T. Hesjedal, “Calculation of the magnetic stray field of a uniaxial magnetic domain,” *Journal of Applied Physics*, vol. 97, no. 7, p. 074504, 2005.

List of Figures

1.1	3D printed magnets on a whiteboard.	3
2.1	Tool-chain of the additive manufacturing process.	6
2.2	AM technologies classified on their basic principle.	6
2.3	AM processes that use polymerization to form the object.	8
2.4	Binder Jetting (BJ)	8
2.5	AM processes by melting the construction material together.	10
2.6	Laminated object manufacturing (LOM)	11
2.7	Break-even analysis comparing conventional and AM processes.	11
2.8	Errors due to tessellation and slicing.	12
2.9	Hysteresis curve for a typical hard magnetic material.	15
2.10	Magnetic properties of common permanent magnetic materials.	18
2.11	Qualitative influence of the filling fraction on the characteristic properties of filled thermoplastics.	22
2.12	Comparison between the filling volume and mass fraction of PA12+Sr-Ferrite and PA12+NdFeB compounds, respectively.	23
2.13	Influence of the size distribution and filler morphology on the maximum packing density	26
2.14	Schematic sketch of a twin-screw extruder for compound manufacturing.	27
2.15	Conventional manufacturing methods and their used magnetic and matrix materials.	28
3.1	3D printer Builder from Code P with its mixing extruder.	32
3.2	Tool-chain for slicing of a STL file.	34
3.3	Noise signal and the detectivity measurement.	39
3.4	Different sensor mounting capabilities.	40

3.5	Principle of the software to define the measuring grid.	41
3.6	Height profile of a complex structure.	42
3.7	Sketch and picture of the calibration procedure.	44
3.8	Magnetic flux measurement before and after calibration.	45
3.9	Area scan of the magnetic flux density B , 1 mm above the cylinder magnet.	46
3.10	Comparison between the Infineon and the 3D printer field mapping system.	46
3.11	Area scan of the absolute error between the Infineon and the 3D printer field mapping system.	47
3.12	Concepts to realize a “maxel” printer.	48
3.13	Simulations results for the “maxel” printer.	49
3.14	Upgrade of the 3D printer to a “maxel” printer.	50
4.1	Scanning electron microscopic (SEM) image of Neofer [®] 25/60p.	53
4.2	Sketch of the filament extrusion line.	55
4.3	Picture of the extruded and spooled filaments.	56
4.4	Printing errors caused of the filament quality.	57
4.5	Thermogravimetric analysis.	58
4.6	3D μ -CT scan of a 3D printed cube made of Neofer [®] 25/60p.	60
4.7	Measurement of the magnetic properties.	62
4.8	Hysteresis measurement with different characterization methods.	63
4.9	Magnetic properties of 3D printed Neofer [®] 25/60p.	65
4.10	VSM measurements at different temperatures.	65
4.11	PFM measurements of PA12+MQP-S-11-9 with different filler fractions.	66
4.12	ASTM D638-10 Type IV specimens for tensile tests.	67
4.13	Tensile stress-strain test results of Neofer [®] 25/60p and pure PA12.	68
4.14	DMA measurements of pure PA12, PA12+MQP-S, and Neofer [®] 25/60p.	70
5.1	Difference between Maxwell’s magnetostatic forward and inverse problem.	72
5.2	Principle of discretization.	77
5.3	Workflow of FEniCS and their components and interplay.	78
5.4	Validation of the demagnetization field calculation.	80
5.5	Validation of the FEM method for the demagnetization field calculation.	81
5.6	Discretization error as a function of the variable air box size factor for different maximum sizes of the tetrahedral elements.	82

5.7	Simulated stray field with the implemented FEM method and Comsol. . . .	83
5.8	Optimization procedure by the adjoint variable method (AVM).	86
5.9	Theoretical L-curve to determine the best choice for the regularization parameter α	87
5.10	Geometric definitions of the problem, and the reconstructed magnetization.	89
5.11	L-curves for the reconstruction of the flower state magnetization.	91
5.12	Validation of the topology optimization framework.	93
5.13	Maximization of B_z with different volume constraints of the design volume.	94
5.14	Topology optimization of a permanent and soft magnetic combined yoke. .	95
6.1	Magnetic wheel speed sensing.	97
6.2	3D printed back bias magnet for magnetic speed sensing applications. . . .	98
6.3	Reconstructed topology of the scanned back-bias magnet.	100
6.4	3D print of a polymer-bonded magnet with a variable magnetic compound fraction.	101
6.5	Reconstructed magnetization of a cuboid printed structure.	102
6.6	3D prints of magnetic hollow cylinder with a variable magnetic compound fraction distribution to generate a predefined stray field inside the cylinder.	103
6.7	Errors of the printed magnets for a predefined stray field.	104
6.8	Setup of a magnetic configuration to linearize B_z in the region Ω_f	105
6.9	Topology optimized magnetic configuration with different volume constraints.	106
6.10	Comparison between simulations and measurements.	107
6.11	Magnetic linear incremental scales.	109
6.12	Current neutron interferometric setup.	111
6.13	Current Larmor Spin-Rotator.	112
6.14	Modified and optimized Halbach cylinder.	113
6.15	Initial designs for the optimized Larmor spin-rotator.	114
6.16	Action as a function of the gap and the remanence.	114
6.17	Relative error for both optimized designs.	115
6.18	3D printed Larmor spin-rotator and test of the magnetic performance. . . .	116
6.19	3D printed Larmor spin-rotator neutron interference experiment.	117
A.1	Calculation of the demagnetization factor and the magnetic stray field of an uniaxial magnetic domain.	122

List of Tables

2.1	Comparison chart of different additive and conventional manufacturing technologies.	13
3.1	Best empirically found printer parameters for the different used materials. .	36
3.2	Detectivity measurement for the 3D Hall transducer scanner for static magnetic fields for all three direction in space.	39
3.3	Typical calibration parameters for the 3D field mapping setup.	44
4.1	Characteristic properties of the used isotropic compounds from the Magnetfabrik Bonn GmbH.	52
4.2	Properties of the used isotropic powder from Magnequench Corporation. .	52
4.3	TGA results for different compound materials.	58
4.4	Calculation of the volumetric mass density ρ for 3D printed and IM Neofer [®] 25/60p, and PA12+MQP-S (85 wt.%) compound.	59
4.5	Summary of the magnetic properties of the 3D printed samples.	66
4.6	Tensile test results of Neofer [®] 25/60p and pure PA12.	68

Curriculum Vitæ

CHRISTIAN HUBER

Maria-Trapp-Platz 2/2/216

1220 Wien

Born on 13 August 1986, Schärding, Austria.

Professional Experience

- since 05/17 University of Vienna, Christian Doppler Laboratory for Advanced Magnetic Sensing and Materials/ Institute of Physics, project assistant
- 11/2015–05/2017 Vienna University of Technology, Christian Doppler Laboratory for Advanced Magnetic Sensing and Materials/ Institute of Solid State Physics, project assistant
- 02/2015–11/2015 Piezocryst Advanced Sensorics GmbH, product development, project manager
- 03/2014–11/2014 Vienna University of Technology, Institute of Electrodynamics, Microwave, and Circuit Engineering, research associate
- 03/2012–07/2013 CME-Engineering GmbH, student employee
- 08/2011–09/2011 Knowles Electronics AG, R&D department, internship
- 08/2010–10/2011 NXP Semiconductors AG, R&D department, internship
- 08/2009–10/2009 Sagem Communications Austria GmbH, R&D department, internship
- 09/2006–04/2009 BPS Engineering GmbH, technical drawer
- 07/2006–09/2006 Ferro Montagetechnik GmbH, metal technician
- 01/2005–07/2005 SGS Personalservice GmbH, metal technician
- 09/2001–12/2004 Schwarzmüller Karosseriefabrik GmbH, apprenticeship as metal worker

Education

- 11/2015–01/2018 Ph.D., Technical Physics, Vienna University of Technology
11/2012–11/2014 M.Sc., Technical Physics, Vienna University of Technology
08/2013–12/2013 Joint study programme, University of Illinois at Urbana-Champaign, USA
11/2011 ATHENS programme, Istanbul Technical University, Turkey
10/2009–11/2012 B.Sc., Technical Physics, Vienna University of Technology

09/2005–06/2009 Evening school in mechanical engineering, Higher technical school (HTL), Ottakring/Vienna

Awards

- 06/2017 Best student-led project at IEEE Magnetic Society Summer School in Santander, Spain
12/2013 Performance scholarship from Vienna University of Technology

List of Publications

Peer-Reviewed Articles

- [10] R. Windl, C. Abert, F. Bruckner, C. Huber, C. Vogler, H. Weitensfelder, and D. Suess, "Contactless and absolute linear displacement detection based upon 3d printed magnets combined with passive radio-frequency identification," *AIP Advances*, vol. 7, no. 11, p. 115121, 2017.
- [9] M. Ortner, C. Huber, N. Vollert, J. Pilz, and D. Suess, "Application of 3d-printed magnets in magnetic position detection systems," *IEEE Sensors Journal*, accepted for publication, 2017.
- [8] C. Abert, C. Huber, F. Bruckner, C. Vogler, G. Wautischer, and D. Suess, "A fast finite-difference algorithm for topology optimization of permanent magnets," *Journal of Applied Physics*, vol. 122, no. 11, p. 113904, 2017.

- [7] C. Huber, C. Abert, F. Bruckner, M. Groenefeld, S. Schuschnigg, I. Teliban, C. Vogler, G. Wautischer, R. Windl, and D. Suess, "3d printing of polymer-bonded rare-earth magnets with a variable magnetic compound fraction for a predefined stray field," *Scientific Reports*, vol. 7, p. 9419, Aug 2017.
- [6] C. Huber, C. Abert, F. Bruckner, C. Pfaff, J. Kriwet, M. Groenefeld, I. Teliban, C. Vogler, and D. Suess, "Topology optimized and 3d printed polymer-bonded permanent magnets for a predefined external field," *Journal of Applied Physics*, vol. 122, no. 5, p. 053904, 2017.
- [5] G. Shilyashki, H. Pfutzner, and C. Huber, "Interlaminar magnetic flux assessment of a transformer core measured by an extra-thin printed foil detector," *IEEE Transactions on Magnetics*, 2017.
- [4] F. Bruckner, C. Abert, G. Wautischer, C. Huber, C. Vogler, M. Hinze, and D. Suess, "Solving large-scale inverse magnetostatic problems using the adjoint method," *Scientific Reports*, vol. 7, p. 40816, Jan 2017.
- [3] R. Windl, F. Bruckner, C. Abert, C. Huber, C. Vogler, T. Huber, H. Oezelt, and D. Suess, "Passive wireless strain measurement based upon the villari effect and giant magnetoresistance," *Applied Physics Letters*, vol. 109, no. 25, p. 253502, 2016.
- [2] C. Huber, C. Abert, F. Bruckner, M. Groenefeld, O. Muthsam, S. Schuschnigg, K. Sirak, R. Thanhoffer, I. Teliban, C. Vogler, R. Windl, and D. Suess, "3d print of polymer bonded rare-earth magnets, and 3d magnetic field scanning with an end-user 3d printer," *Applied Physics Letters*, vol. 109, no. 16, p. 162401, 2016.
- [1] C. Huber, S. Smolek, and C. Strelj, "Simulation of layer measurement with confocal micro-xrf," *X-Ray Spectrometry*, vol. 43, no. 3, pp. 175–179, 2014.

Technical Papers

- [2] C. Huber, M. Groenefeld, and D. Suess, "Dauermagnete aus dem 3d-drucker," GIT Labor-Fachzeitschrift 5, Wiley Verlag, 2017.
- [1] C. Huber, C. Abert, F. Bruckner, M. Groenefeld, O. Muthsam, S. Schuschnigg, K. Sirak, R. Thanhoffer, I. Teliban, C. Vogler, R. Windl, and D. Suess, "3d print

of polymer bonded rare-earth magnets, and 3d magnetic field scanning with an end-user 3d printer,” *MagNews 1*, UK Magnetic Society, 2017.

Poster Presentations

- [2] C. Huber, F. Bruckner, S. Sponar, C. Abert, M. Groenefeld, and D. Suess, “Additive Manufacturing of Polymer Bonded Rare-Earth Magnets for a Predefined External Field”, *Joined SPG – OEPG Meeting*, Genf, Switzerland, August 2017
- [1] C. Huber, C. Abert, F. Bruckner, M. Groenefeld, and D. Suess, “Additive Manufacturing of Polymer-Bonded Rare-Earth Magnets for Stray Field Shaping”, *IEEE Magnetic Society Summer School*, Santander, Spain, June 2017

Talks at Scientific Conferences

Invited Talks

- [1] C. Huber, M. Groenefeld, and D. Suess, “3D Printed Magnets for a Predefined External Field”, *MagMatApp’17: Magnetic Materials for the Optimization of Motors, Generators and other Advanced Applications*, UK Magnetic Society Seminar, Hannau, Germany, October 2017

Contributed Talks

- [2] C. Huber, F. Bruckner, C. Abert, C. Vogler, M. Groenefeld, S. Schuschnigg, I. Teliban, and D. Suess, “3D Printing of Polymer Bonded Rare-Earth Magnets With a Variable Magnetic Compound Density for a Predefined Stray Field”, *MMM 2016*, New Orleans, USA, November 2016
- [1] C. Huber, C. Abert, F. Bruckner, M. Groenefeld, O. Muthsam, S. Schuschnigg, K. Sirak, R. Thanhoffer, I. Teliban, C. Vogler, R. Windl, and D. Suess, “3D Print of Polymer Bonded Rare-Earth Magnets, and 3D Magnetic Field Scanning With an End-User 3D Printer”, *JEMS 2016*, Glasgow, UK, August 2016